

Technische Universität München
Lehrstuhl für Technische Chemie II

Understanding hydrodenitrogenation on unsupported and supported sulfide based catalysts

Ana Hrabar

Vollständiger Abdruck der von der Fakultät für Chemie der Technischen Universität
München zur Erlangung des akademischen Grades eines

Doktors der Naturwissenschaften (Dr. rer. nat.)

genehmigten Dissertation.

Vorsitzender:

Univ.-Prof. Dr. K.-O. Hinrichsen

Prüfer der Dissertation:

1. Univ.-Prof. Dr. J.A. Lercher
2. Univ.-Prof. M. Tromp, Ph.D.

Die Dissertation wurde am 05.07.2011. bei der Technischen Universität München
eingereicht und durch die Fakultät für Chemie am 15.09.2011. angenommen.

“I have no special talents. I am only passionately curious.”

Albert Einstein

To my family

Acknowledgements

Now when my time as a PhD student at the TU München is coming to an end I would like to thank all people who have contributed my work during the last four years and have made this thesis possible.

At first I would like to thank Johannes (Prof. J.A. Lercher) for giving me the opportunity to work in his group on a very interesting project. Thank you for your trust, patience, guidance and helpful discussions. I enjoyed all the scientific freedom you gave me regarding my work. During this time I learnt a lot and gained great experience in how to manage frequent meetings, and to confidently present and discuss my results with scientific experts. Certainly this period developed me faster than I could ever imagine.

Further I would like to thank my project partners at Chevron Energy Technology Company, in particular Alex (Dr. A. Kuperman) and Axel (Dr. A. Brait) for fruitful telephone discussions on the topic of hydrodenitrogenation. Thank you for carefully following all the steps of my work and for giving me useful advices and suggestions. I was always happy to hear your point of view on the insights of chemistry and on other matters. Thanks for inviting me to visit you in California. I really enjoyed that experience.

Thank you Oliver (Dr. O.Y. Gutiérrez) for extensive discussions that helped me to bring my work to an end. Your broad experience in the field of hydrotreating brought more insights to my work. Thank you for your patience over last months and very useful comments and suggestions.

Thank you Andy (Dr. A. Jentys), for helping me with the XAFS data analysis and for your support during the time I spent at DESY in Hamburg. Xaver (Dipl.-Ing. X. Hecht), without you it would have been impossible to get the work done. Thank you for teaching me how to manage my setup, to fix numerous problems with the vacuum systems, GC, gas leaks... Thank you Marianne (Dr. M. Hanzlik), for performing the TEM measurements. Special thanks to Helen, Steffi and Katharina for being there always when I needed it. Thanks Martin and Andreas for your help with measurements and troubleshooting.

I would like to express my gratitude to Jennifer. You have been of great help with your hard working schedule and new ideas during the work on your Diploma thesis. Also, life wouldn't have been easy without you Yanzhe. Thank you for your great help when I was starting to work on my setup, and for often discussions on the hydrogenation part. Thank you both for being great friends.

Thanks to all TCII people. It was really great to be part of such a big international group. Working and hanging out with you was a wonderful experience and I will never forget you. Thanks for being so friendly and open minded. Thanks to my first officemates Wolfgang, Aonsurang, Andreas, Christoph and Prado for welcoming me and helping me a lot with getting into the group. Thanks Virginia, Elvira and Benjamin for generous help in the lab and great time we spent partying. Thanks to my “second generation” of officemates Marta, Chen, Manuela and Elisabeth for great time and relaxing coffee breaks. Thanks to Cornelia, Roberta, Yongzhong, Xuebing, Andre, Erika, Rino, Peter, Olga, Jürgen, Matteo, Frederik, Praveen, Lay-Hwa, Dechao, Manuel, Richard, Tobias, Sabine, Florian, Anna, Sonja, Daniela, Claudia, Sarah, Despina, Stephan, Oliver, Christian, Nianhua, Baoxiang, Herui, Lin Lin, Michael, Linus, Shi Hui, Xianyong, Ren, Robin, John, Stefanie, Jiayue, Stefan, Bo, Monica, Eva and Yuchun. It was great working with all of you.

Last but not the least I would like to thank my husband Pierluigi, my parents and my sister Sanja for giving me great strength, for being patient and supportive in the last years. Without you it wouldn't be possible to cope with all the stress and tension. Thanks to my friends outside TCII. Thanks Pamela, Philippe, Marina, Zarko and Sonja for spending great free time together and for cheering me out when my moods were down.

Ana

July 2011

Table of Contents

Chapter 1.....	1
General Introduction.....	1
1. Crude oil as the source of energy.....	2
2. Industrial hydrotreating.....	4
3. Hydrodesulfurization (HDS).....	7
3.1. Sulfur containing compounds.....	7
3.2. Thermodynamics.....	8
3.3. Reaction mechanism.....	8
4. Hydrodenitrogenation (HDN).....	9
4.1. Nitrogen containing compounds.....	10
4.2. Thermodynamics.....	11
4.3. Reaction mechanism.....	12
5. Hydrotreating catalysts.....	13
5.1. Structure of the oxidic catalyst precursor.....	14
5.2. Structure of sulfide catalyst.....	15
5.3. Catalytic active sites.....	16
5.4. Further development of hydrotreating catalysts.....	18
6. Scope of the thesis.....	19
7. References.....	20
Chapter 2.....	23
<i>Selective poisoning of the direct denitrogenation route in the o-propylaniline HDN by DBT on Mo and NiMo/γ-Al₂O₃ sulfide catalysts</i>	23
1. Graphical abstract.....	24
2. Introduction.....	24
3. Experimental.....	26
3.1. Catalyst preparation.....	26
3.2. Catalyst characterization.....	26
3.3. Kinetic test.....	27
4. Results.....	30
4.1. Catalyst characterization.....	30
4.1.1. Physicochemical properties.....	30
4.1.2. X-ray diffraction (XRD).....	30
4.1.3. Transmission electron microscopy (TEM).....	31
4.1.4. Raman spectroscopy.....	31

4.1.5. Temperature-programmed sulfidation (TPS).....	32
4.1.6. NO adsorption	33
4.2. Hydrodenitrogenation of o-propylaniline (OPA).....	35
4.2.1. Kinetic modeling of the HDN OPA network	36
4.2.2. Influence of Ni substitutions on the OPA HDN	38
4.2.3. Effect of dibenzothiophene (DBT) on the OPA HDN	39
4.2.4. Stability of the NiMoS/ γ -Al ₂ O ₃ catalyst in the OPA HDN.....	43
4.2.5. Temperature dependence of the catalytic reaction	44
5. Discussion	47
6. Conclusion.....	54
7. Acknowledgements.....	55
8. References	56
Chapter 3.....	59
<i>C(sp³)-N bond cleavage in the ring opening of 1,2,3,4-tetrahydroquinoline and decahydroquinoline on Mo and NiMo/γ-Al₂O₃ sulfide catalysts</i>	<i>59</i>
1. Introduction.....	60
2. Experimental.....	61
2.1. Catalyst synthesis and characterization	61
2.2. Kinetic test	62
3. Results	63
3.1. Catalyst characterization	63
3.1.1. Physicochemical properties	63
3.1.2. Temperature-programmed desorption (TPD) and reduction (TPR)	63
3.2. Hydrodenitrogenation of decahydroquinoline (DHQ).....	65
3.2.1. HDN reaction network.....	65
3.2.2. Effect of Ni promoter and dibenzothiophene (DBT).....	68
3.3. Hydrodenitrogenation of quinoline	70
3.3.1. HDN reaction network.....	70
3.3.2. Effect of Ni promoter and DBT	72
4. Discussion	74
4.1. Reaction pathway of quinoline and DHQ HDN.....	74
4.2. The active sites and mechanism for the ring opening via C(sp ³)-N bond cleavage ...	76
5. Conclusion.....	80
6. Acknowledgements.....	81
7. Supplementary material	82
7.1. Calculation of equilibrium constants at T= 370 °C and p= 5 MPa.....	82

7.1.1. Quinoline and 1,2,3,4-Tetrahydroquinoline (14THQ).....	82
7.1.2. Quinoline and 5,6,7,8-Tetrahydroquinoline (58THQ).....	82
7.1.3. 1,2,3,4-Tetrahydroquinoline (14THQ) and Decahydroquinoline (DHQ)	83
7.1.4. 5,6,7,8-Tetrahydroquinoline (58THQ) and Decahydroquinoline (DHQ)	83
8. References	84
<i>Chapter 4.....</i>	<i>86</i>
<i>Characterization and performance of γ-Al₂O₃ supported Mo and NiMo and novel unsupported NiMo catalysts in the HDN of quinoline</i>	<i>86</i>
1. Introduction.....	87
2. Experimental.....	88
2.1. Catalyst preparation.....	88
2.2. Catalyst characterization	89
2.3. Catalyst performance.....	91
3. Results	92
3.1. Physicochemical properties	92
3.2. X-ray diffraction (XRD).....	92
3.2.1. Oxide catalyst precursors	92
3.2.2. Sulfide catalysts.....	93
3.3. Transmission electron microscopy – selective area diffraction (TEM-SAD).....	94
3.3.1. Supported sulfide catalysts	94
3.3.2. NiMo unsupported oxide catalyst precursor	94
3.3.3. NiMo unsupported sulfide catalysts	95
3.4. Raman spectroscopy	95
3.4.1. Oxide catalyst precursors	95
3.4.2. Sulfide catalysts.....	97
3.5. Diffuse reflectance UV-vis spectroscopy.....	98
3.6. X-ray absorption spectroscopy (XAS)	99
3.6.1. Oxide catalyst precursors	99
3.6.2. Transition from oxide precursors to sulfide catalysts.....	102
3.6.3. Sulfide catalysts.....	103
3.7. Temperature-programmed sulfidation (TPS).....	105
3.8. The HDN of quinoline	106
3.8.1. The HDN of quinoline as a space time dependent experiment.....	106
3.8.2. The HDN of quinoline as a temperature dependent experiment.....	110
4. Discussion	113
4.1. Catalyst characterization	113

4.2. The HDN of quinoline	116
5. Conclusion.....	119
6. Acknowledgements.....	120
7. References	121
<i>Chapter 5</i>	124
<i>Summary</i>	124
1. Summary	125
<i>Curriculum Vitae</i>	128
<i>List of publications</i>	129

List of Abbreviations

BTU	British thermal unit
HYD	Hydrogenation
HDS	Hydrodesulfurization
HDN	Hydrodenitrogenation
HDO	Hydrodeoxygenation
HDM	Hydrodemetallization
FCC	Fluid catalytic cracking
ppm	Parts per million
DBT	Dibenzothiophene
46-DM-DBT	4,6-Dimethyldibenzothiophene
DDS	Direct desulfurization
Q	Quinoline
14THQ	1,2,3,4-Tetrahydroquinoline
58THQ	5,6,7,8-Tetrahydroquinoline
DHQ	Decahydroquinoline
OPA	O-propylaniline
PCHA	Propylcyclohexylamine
PB	Propylbenzene
PCH	Propylcyclohexane
PCHE	Propylcyclohexene
DDN	Direct denitrogenation
HYD	Hydrogenation
TMS	Transition metal sulfides
BET	Brunauer-Emmet-Teller
XRD	X-ray diffraction
TEM-SAD	Transmission electron microscopy – selective area diffraction
XAS	X-ray absorption spectroscopy
EXAFS	Extended X-ray absorption fine structure
XANES	X-ray absorption near edge structure
°C	Celsius
MPa	Mega Pascal
RT	Room temperature

Chapter 1

General Introduction

This chapter introduces the importance of industrial hydrotreating processes because of the growing petroleum demand and stricter environmental legislations. Concepts for hydrodesulfurization (HDS) and hydrodenitrogenation (HDN) are given and reaction networks of model compounds are described. Effects of hydrogen disulfide and hydrogen donating molecules are discussed. The overview of a catalyst precursor structure as well as of a conventional promoted MoS₂ catalyst is given with a special emphasis on the active sites. Further development of catalytic systems is proposed.

1. Crude oil as the source of energy

Crude oil (petroleum) consists of complex gaseous, liquid, and solid hydrocarbons, and other organic hetero compounds containing sulfur, nitrogen, oxygen and trace amounts of metals. The relative concentration of hydrocarbons, i.e., paraffins, naphthenes, aromatics, and asphaltenes depends on the oil type. Therefore crude oil exists with a wide range of specific gravity and viscosity. Even though its physical properties may vary depending on the consisting compounds, the proportion of chemical elements is found to be in a very narrow range, Table 1 [1].

Chemical element	wt. %
Carbon	83 – 87
Hydrogen	10 – 14
Sulfur	0.5 – 6
Nitrogen	0.1 – 2
Oxygen	0.1 – 1.5
Metals	< 0.1

Table 1. Elementary composition of petroleum [1].

Consumption of different types of energy over past years and the prediction for the future is shown in Table 2. Crude oil presents the most frequently used resource of energy and is mostly used for the liquid fuel production. Therefore, higher liquid fuel consumption leads to a growing crude oil demand.

	Energy consumption, quads (1 quad ~ 10 ¹⁵ BTU or 1.055 kJ)			
	1995	1996	2010	2015
Crude oil (petroleum)	34.7	36.0	40.4	44.1
Gas	22.3	22.6	26.3	31.9
Coal	19.7	20.8	24.1	29.0
Nuclear	7.2	7.2	7.4	4.7
Hydro	3.4	4.0	3.2	3.2
Other	3.2	3.3	4.0	5.2

Table 2. Past and projected energy consumption [1].

One of the world's greatest progresses in the 20th century was the transportation revolution. In nowadays, the consumption of diesel fuels is the highest among the three dominant types of fuels, i.e., gasoline (cars with spark ignition engines), diesel fuel (track or trains with compression ignition engines) and jet fuel (sailing ships and aircrafts with gas turbine engines) [2]. Continuously growing demand made the specifications standards and environmental legislations on diesel fuel composition and properties more severe. The most important steps in the development of diesel fuel in EU are shown in Table 3 [3]. These quality standards for the EU automotive fuels have been developed from European Standard

Organization (CEN) with the aim to reduce the pollutant emissions since the transportation present the major source of air pollution in urban environments.

Year	Max. sulfur limit, ppm	Min. cetane number
October 1994	1000	49
October 1996	500	
January 2000	350	51
January 2005	50 (for highway vehicles)	
January 2009	10 (for highway vehicles)	

Table 3. CEN quality standards for diesel fuel [3].

Numerous countries have great oil reserves, Fig. 1. [4]. Nevertheless, diminishing of lighter crude oil reserves has led to a shift towards heavy oil use, since the most of world's oil resources are heavy hydrocarbons, Fig. 2 [5]. Even though, heavy crude oils contain higher concentration of impurities, i.e., sulfur- and nitrogen-containing compounds, and metals that make them difficult and more expensive to refine, they present the future of the oil industry because of great availability.

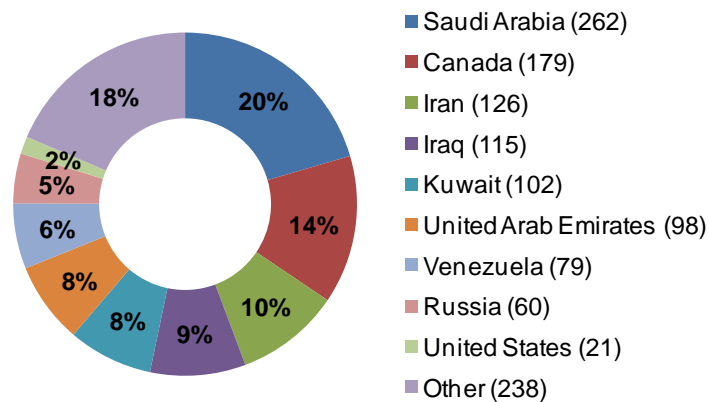


Figure 1. Oil reserves by country from U.S. Energy Information Administration, 2006.

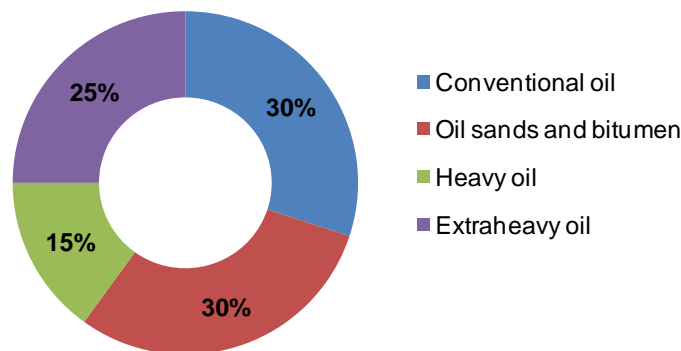


Figure 2. Total oil resources of 9 to 13 trillion bbl [5].

2. Industrial hydrotreating

One of the most performed refinery processes is hydrotreating [6]. It is used for hydrogenation of double bonds and aromatic rings, hydrogenolysis reaction where C-X bond is cleaved for the heteroatom removal (X= S, N, O), and removal of metals, for improving the product quality and for obtaining the environmentally acceptable products. At the mild conditions of hydrotreating reactions, the molecular size doesn't change significantly in contrast to hydrocracking reactions where C-C bond cleavage occurs [7]. Therefore hydrotreating is reductive treatment of organic molecules consisting of following reactions: hydrogenation (HYD), hydrodesulfurization (HDS), hydrodenitrogenation (HDN), hydrodeoxygenation (HDO) and hydrodemetallization (HDM) that are carried out simultaneously in industry [8]. Sulfur removal is carried out via formation of H₂S, nitrogen via NH₃ and oxygen via formation of H₂O. Metals are often removed in form of metal sulfides.

Besides improving the fuel quality (odor, color, stability, corrosion), the main purpose of hydrotreating reactions is to reduce the air pollution emissions and to avoid poisoning of noble metals and acid catalysts used in catalytic reforming and cracking. Primary objective in naphtha hydrotreating is to remove sulfur-containing compounds for downstream processes because hetero-compounds often act as poisons. Sulfur is also removed from gasoline and mid-distillate (kerosene, diesel, jet fuel) to meet the clean fuel specifications. Hydrotreating of FCC feed is done for removal of nitrogen containing compounds, for better cracking catalyst activity. Metals induce many problems. When burned in oils they produce ash which deposits in engines causing the damage [9]. The overview of different starting feedstocks and the purpose of hydrotreating reactions is given in Table 4 [2].

Reaction	Feedstock	Purpose
HDS	Catalytic reformer feedstocks	Reduce catalyst poisoning
	Diesel fuel	Environmental specifications
	Distillate fuel oil	Environmental specifications
	Hydrocracker feedstocks	Reduce catalyst poisoning
	Coker feedstocks	Reduce sulfur content of coke
HDN	Lubricating oil	Improve stability
	Catalytic cracking feedstocks	Reduce catalyst poisoning
	Hydrocracker feedstocks	Reduce catalyst poisoning
HDM	Catalytic cracking feedstocks	Avoid metals deposition
		Avoid coke buildup
		Avoid catalyst destruction
	Hydrocracker feedstocks	Avoid metals deposition
		Avoid catalyst destruction

Table 4. Outcome of Hydroprocesses in Refining [2].

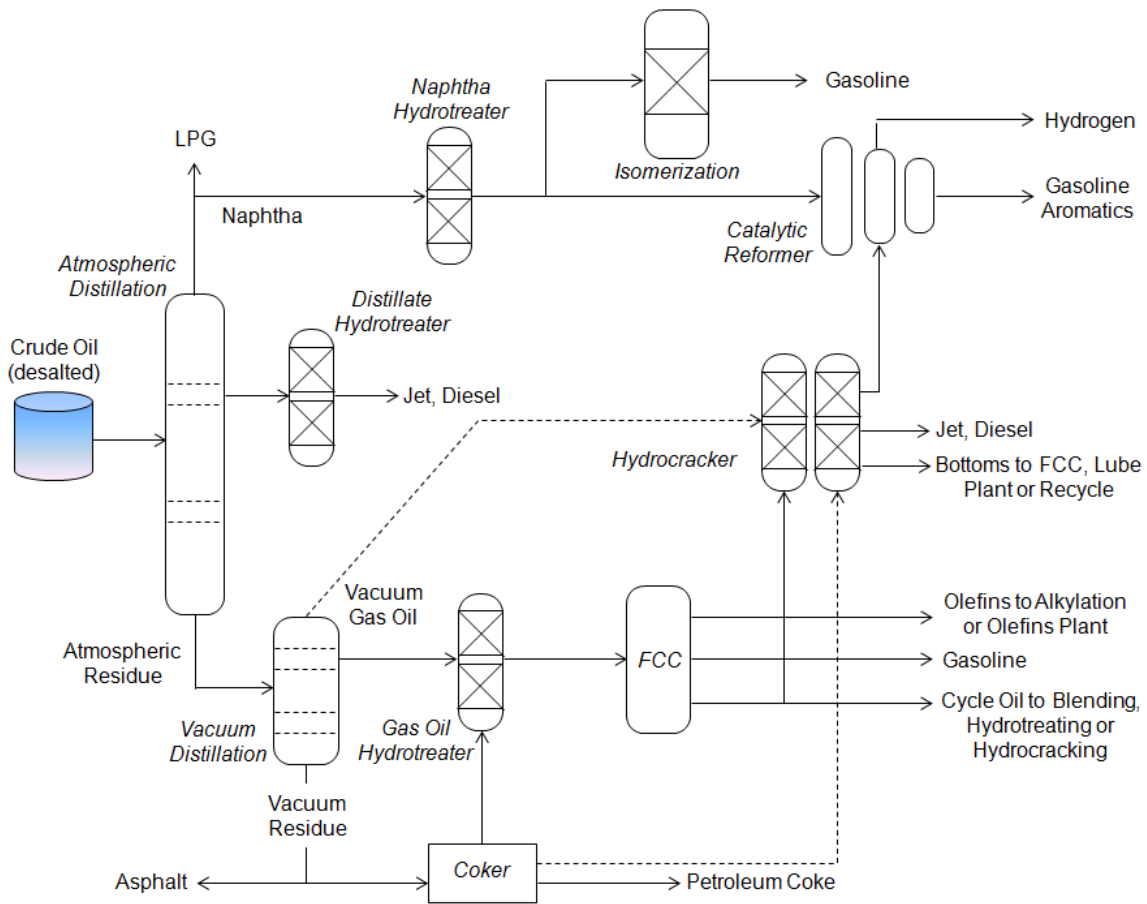


Figure 3. Scheme of typical Oil Refinery [9].

The world's hydrotreating capacity is half of the crude distillation capacity [9]. Refineries typically use at least three hydrotreating units, i.e., one or two for vacuum or heavy gas oil, one or two for light gas oil, and one for naphtha, as shown in Fig. 3. Hydrotreating reactions take place in a fixed catalyst bed reactor, Fig. 4. At first, hydrogen is mixed with a preheated feed and the flow is further directed downward through the reactor, packed with various catalysts depending on the process. The reaction effluent is then cooled and passed through the high pressure separator that separates the liquid hydrocarbon from gaseous H_2 , H_2S , and NH_3 . Acid gases are further absorbed from hydrogen that is then recycled.

Hydrotreating reactions are carried out simultaneously in industry and the effect of individual processes on each other is complex. HDN is considered to be more difficult and demanding than HDS, Table 5 [10]. Besides the fact that HDN is requiring more rigorous reaction conditions, the content of nitrogen-containing compounds in conventional crude oil is rather small. Thus, in the past, more attention was given to HDS. Generally with increasing the boiling point of the oil fraction the sulfur- and nitrogen-content is higher. The increase of sulfur-content is slower than that of nitrogen. From naphtha to gas oil, the nitrogen-content enhances by two or three orders of magnitude while the sulfur only one or two [11].

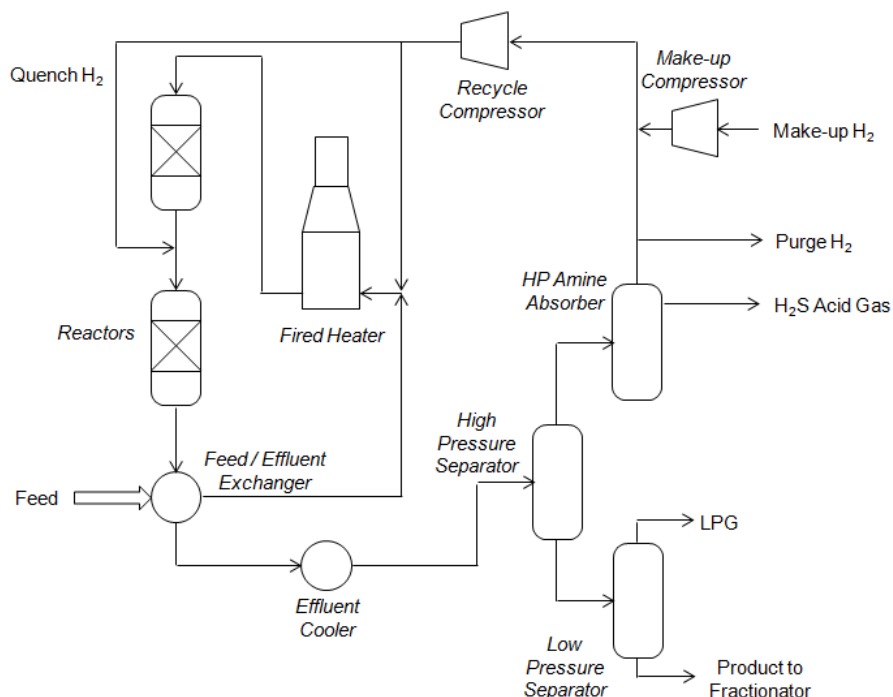


Figure 4. Scheme of Hydrotreating Process.

Recent need for processing the lower quality crude oil and more strict environmental requirements have put more interest in the HDN. For better understanding the complexity of oil refining, Table 6 shows broad range of contamination in different crude oil [12]. Evidently the amount of sulfur and nitrogen vary extensively, hence each crude oil requires different catalyst performance. Therefore it is necessary to focus on the catalyst development since the improvement of the process itself via changing the reactor configuration and reaction conditions is economically inconvenient.

	wt.% S			wt.% N		
	Original	Product	Removal, %	Original	Product	Removal, %
I	0.8	0.05	94	0.015	0.007	53
II	1.19	0.07	94	0.056	0.041	27
III	1.58	0.14	91	0.012	0.007	42

Table 5. Comparison of S and N removal from three different petroleum distillates [10].

	Arabian light	Arabian heavy	Attaka	Boscan
S, wt. %	1.8	2.9	0.07	5.2
N, wt. %	0.1	0.2	< 0.1	0.7
O, wt. %	< 0.1	< 0.1	< 0.1	< 0.1
V, ppm	18	50	< 1	1200
Ni, ppm	4	16	< 1	150

Table 6. Typical content of contaminants in various crude oil [12].

3. Hydrodesulfurization (HDS)

Hydrodesulfurization is accomplished by the catalytic reaction of hydrogen with organic sulfur-containing compounds from crude oil and its fractions to produce H_2S [13]. Sulfur-containing compounds cannot be tolerated in fuels, as upon combustion they produce sulphuric acid and also poison reforming catalyst. Sulfur content of the feed used for reforming should not exceed 1 ppm [7]. Furthermore sulfur-containing compounds cause corrosion and have unpleasant smell.

3.1. Sulfur containing compounds

In crude oil, there is a variety of sulfur-containing compounds that form different product as a result of desulfurization. Typical sulfur-containing compounds in crude oil are mercaptans, sulfides, disulfides (relatively easy to convert), and thiophene and its derivatives (high stability due to their aromatic character), as shown in Table 7. HDS process involves C-S bond cleavage and saturation of the reactive fragments. Saturation of aromatic rings occurs only when necessary, prior to the C-S bond cleavage, despite the fact that their hydrogenation may be thermodynamically favored [9].

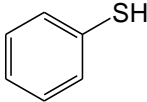
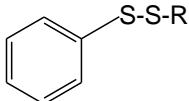
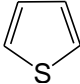
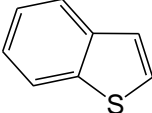
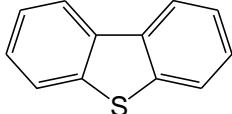
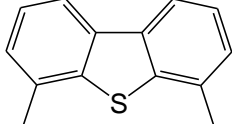
Sulfur containing hydrocarbons in crude oil		
Mercaptans	Aliphatic	R-SH
	Aromatic	
Sulfides	Hydrogen sulfide	H_2S
	Aliphatic	R-S-R
Disulfides	Aliphatic	R-S-S-R
	Aromatic	
Thiophenes	Thiophene	
	Benzothiophene	
	Dibenzothiophene	
	4,6-Dimethyldibenzothiophene	

Table 7. Typical sulfur containing molecules in crude oil [7].

3.2. Thermodynamics

The HDS is an exothermic reaction. Essentially it is irreversible because under industrial conditions (for example, 250 to 350 °C and 3 to 10 MPa) there are no thermodynamic limitations [7]. Difficulties arise from different kinetic rates, because each sulfur-containing compound has its own complex kinetics influenced by a number of consecutive equilibrium stages [9]. Table 8 contains the standard enthalpies and equilibrium constant values for different HDS reactions. The amount of heat released depends on the number of moles of hydrogen needed for desulfurization. Consequently the value of standard enthalpies increases with higher hydrogen consumption and in addition it changes depending on the type of sulfur-containing compound. There is a clear difference in the equilibrium constants from one class of sulfur containing compounds, e.g., mercaptans, to another, e.g., thiophenes. Nevertheless, within the same class, the gap is very small.

Reaction	$\log_{10} K_p$ at T [°C]					ΔH° , kJ/mol
	25	100	200	300	400	
<i>Mercaptans</i>						
$\text{CH}_3\text{SH} + \text{H}_2 \leftrightarrow \text{CH}_4 + \text{H}_2\text{S}$	12.97	10.45	8.38	7.06	6.15	-72
$\text{C}_2\text{H}_5\text{SH} + \text{H}_2 \leftrightarrow \text{C}_2\text{H}_6 + \text{H}_2\text{S}$	10.75	8.69	6.99	5.91	5.16	-59
$\text{C}_3\text{H}_7\text{SH} + \text{H}_2 \leftrightarrow \text{C}_3\text{H}_8 + \text{H}_2\text{S}$	10.57	8.57	6.92	5.87	5.15	-57
<i>Thiophenes</i>						
Thiophene + 4H ₂ ↔ n-C ₄ H ₁₀ + H ₂ S	30.84	21.68	14.13	9.33	6.04	-262
3-Methylthiophene + 4H ₂ ↔ 2-Methylbutane + H ₂ S	30.39	21.35	13.88	9.11	5.82	-258
2-Methylthiophene + 4H ₂ ↔ n-Pentane + H ₂ S	29.27	20.35	13.33	8.77	5.66	-250
<i>Benzothiophenes</i>						
Benzothiophene + 3H ₂ ↔ Ethylbenzene + H ₂ S	29.68	22.56	16.65	12.8	10.2	-203
Dibenzothiophene (DBT) + 2H ₂ ↔ Biphenyl + H ₂ S	24.70	19.52	15.23	12.5	10.6	-148
Benzothiophene + H ₂ ↔ Dihydrobenzothiophene	5.25	3.22	1.55	0.49	-0.23	-58
DBT + H ₂ ↔ Hexahydro-DBT	19.93	11.93	5.47	1.54	-0.98	-230

Table 8. Equilibrium constants and standard enthalpies of HDS reactions [9].

3.3. Reaction mechanism

Desulfurization generally occurs either with or without hydrogenation of the heterocyclic ring. Therefore there are two possible reaction pathways, i.e., the direct desulfurization (DDS) and the hydrogenation (HYD) pathway. Hydrogenation of the ring can be affected by thermodynamic conditions because it is equilibrium-limited at common temperatures. Thus, sulfur-removal via HYD pathway may be inhibited at low pressures and high temperatures.

Prins et al. proposed the complete HDS mechanism of 4,6-dimethyldibenzothiophene (46-DM-DBT) as shown in Fig. 5 [14]. Two methyl groups at positions 4 and 6 are sterically hindering the sulfur atom, therefore 46-DM-DBT is one of the molecules that are the most difficult to desulfurize and which cause problems in deep HDS.

It is important to note that several variables influence the HDS rates, i.e., concentration of organic reactants and products, hydrogen, and hydrogen disulfide. Hydrogen disulfide inhibits hydrodesulfurization of all sulfur containing compounds. Both DDS and HYD pathways are inhibited by H_2S , but inhibition of DDS pathway is more extensive [15]. Prins et al. proposed same catalytic sites for the C-S bond cleavage in both 46-DM-DBT and partially hydrogenated intermediates. The active sites are assumed to be sulfur vacancies on the catalyst surface. That would explain strong inhibition by H_2S . On the other hand hydrogenation reaction pathway is much less affected by H_2S which indicates that sulfur vacancies are not necessary for the hydrogenation.

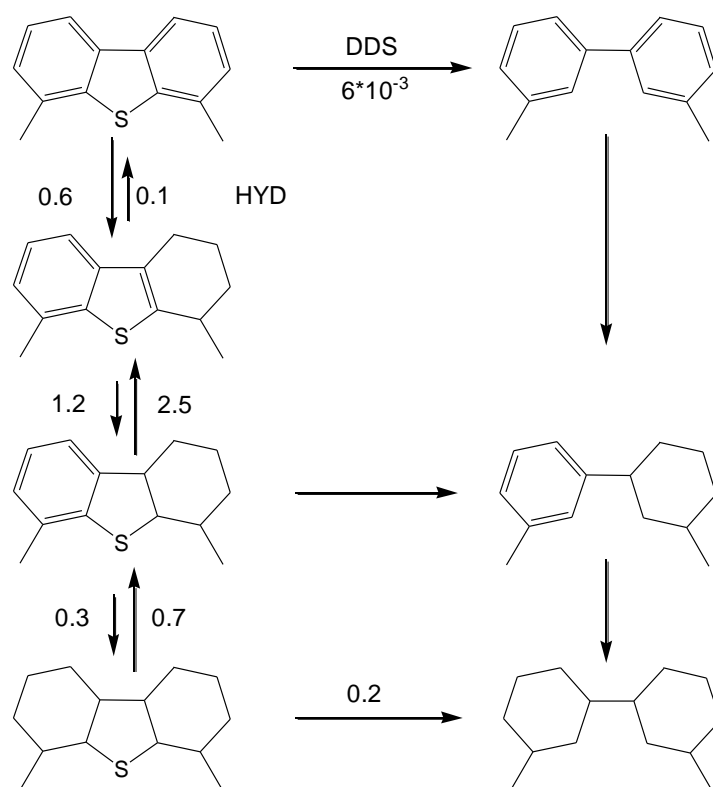


Figure 5. Reaction network of HDS of 46-dimethyldibenzothiophene [14].

4. Hydrodenitrogenation (HDN)

The concentration of nitrogen-containing compounds in crude oil is far lower than that of sulfur-containing compounds. However nitrogen-containing compounds cause significant problems in major catalytic processes because they strongly adsorb on acid catalytic sites needed for cracking and hydrocracking reactions [7]. Studies carried out on real feeds and model compounds indicate that catalytic sites can be poisoned even with less than 50 ppm of nitrogen in the feed [8]. Therefore the HDN is commonly used in conjunction with hydrocracking. Furthermore, the nitrogen-removal is needed to achieve low sulfur level in fuel, to obtain low NO_x emissions and to protect the catalyst.

4.1. Nitrogen containing compounds

Nitrogen-containing compounds consist of two types, i.e., heterocycles and nonheterocycles, Table 9. Nonheterocyclic anilines and aliphatic amines undergo HDN quickly compared to five-membered pyrrolic and six-membered pyridinic rings due to different electronic configuration. Five-membered nonbasic hetero-aromatics have a lone electron pair which is involved in the π -cloud of the ring and it is for that reason not available for the interaction with acids. On the contrary six-membered basic nitrogen aromatics have unshared electron pair, involved in the π -cloud of the ring, available for interaction with acids [16].

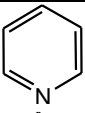
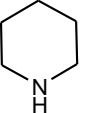
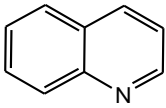
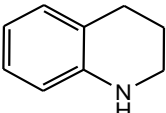
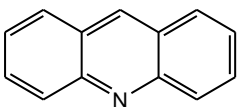
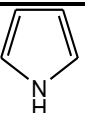
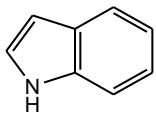
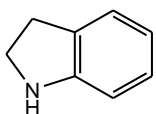
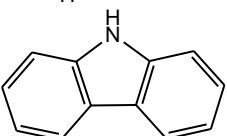
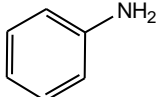
Nitrogen compound	Formula	pKa	Structure
Heterocyclic six-membered (pyridinic) rings			
Pyridine	C_5H_5N	5.2	
Piperidine	$C_5H_{11}N$	11.1	
Quinoline	C_9H_7N	4.9	
Tetrahydroquinoline	$C_9H_{11}N$	5.0	
Acridine	$C_{13}H_9N$	5.6	
Heterocyclic five-membered (pyrrolic) rings			
Pyrrole	C_4H_5N	0.4	
Indole	C_8H_7N	-3.6	
Indoline	C_8H_9N	5.0	
Carbazole	$C_{12}H_9N$	-6.0	
Nonheterocyclic rings			
Aniline	C_6H_7N	5.0	

Table 9. Representative cyclic nitrogen compounds [16].

The type of nitrogen-containing compounds and total amount of nitrogen vary depending on the type of feedstock. The diversity of the compound distribution in the middle distillates, i.e., crude oil, shale oil and tar-sands, is illustrated in Table 10 [17]. Even in the feedstocks with similar boiling range, large differences in the distribution of nitrogen-containing compounds were found.

	Petroleum	Shale-oil	Tar-sands
Total N, ppm	83	2290	3050
Boiling range, °C	220-384	150-390	190-390
Distribution of N compounds, %			
Carbazole	0.5	1.3	3.2
Indole	18.1	3.7	39.2
Pyridine	64.3	73.5	13.3
Pyrrole	0.2	3.6	15.9
Quinoline	10.4	4.3	1.2
Tetrahydroquinoline	3.2	9.9	16.7

Table 10. Distribution of N compounds (%) in middle distillates [17].

4.2. Thermodynamics

The HDN is in great contrast to HDS because it requires complete saturation of the aromatic heterocyclic ring prior to nitrogen removal via hydrogenolysis. Nitrogen is removed as ammonia and although ammonia is a base it is less effective in poisoning the acidic catalytic sites. Saturation of the heteroring is necessary to reduce quite high energy of the C-N bonds in aromatic ring, Table 11, and thus allow facile C-N bond cleavage [9].

Bond	Energy, kcal/mol
C - S	65
C - N	73
C - C	83
S - H	83
N - H	93
C - H	99
C = S	128
C = C	146
C = N	147

Table 11. Bond energies between carbon and heteroatoms [9].

Hydrogenation steps in HDN are reversible, exothermic and equilibrium constants decrease with higher temperature. Detailed knowledge of equilibrium constants is necessary for proper understanding of the overall hydrodenitrogenation mechanism. Table 12 contains standard enthalpies and equilibrium constant values at different temperatures for hydrogenation and hydrogenolysis reactions of various nitrogen-containing compounds [9].

Reaction	$\log_{10} K_p$ at T [°C]		ΔH° , kJ/mol
	300	400	
Quinoline + 2H ₂ ↔ 1,2,3,4-Tetrahydroquinoline	-1.4	-3.2	-133
Quinoline + 2H ₂ ↔ 5,6,7,8-Tetrahydroquinoline	-0.7	-3.0	-171
1,2,3,4-Tetrahydroquinoline + 3H ₂ ↔ Decahydroquinoline	-2.8	-5.4	-192
5,6,7,8-Tetrahydroquinoline + 3H ₂ ↔ Decahydroquinoline	-3.5	-5.6	-155
1,2,3,4-Tetrahydroquinoline + H ₂ ↔ o-Propylaniline	4.3	3.0	-96
Decahydroquinoline + 2H ₂ ↔ Propylcyclohexane + NH ₃	6.3	7.9	-117
o-Propylaniline + H ₂ ↔ Propylbenzene + NH ₃	6.0	5.6	-29
Quinoline + 4H ₂ ↔ Propylbenzene + NH ₃	7.0	3.3	-272

Table 12. Equilibrium constants and standard enthalpies of HDN reactions [9].

4.3. Reaction mechanism

Kinetic modeling of the HDN reactions is complex because the reaction network involves many steps. Even though many different studies on the HDN of alkyl amines [18], pyridine [19,20], piperidine [20,21], and indole [22-25] were published, the HDN of quinoline [26-31] draw the most attention because of its bicyclic nature. Quinoline consists of benzoic ring and heterocyclic six-membered ring therefore its HDN reaction pattern is representative of the benzoic derivatives of pyridine [32]. The overall network of HDN of quinoline consists of several equilibrium stages as proposed by Satterfield et al., Fig. 6 [33-38]. It was observed that the quinoline HDN occurs mainly through decahydroquinoline (DHQ) intermediate while propylcyclohexene (PCH) was the main product. Therefore selectivity towards reaction pathway of minimum hydrogen consumption is very low.

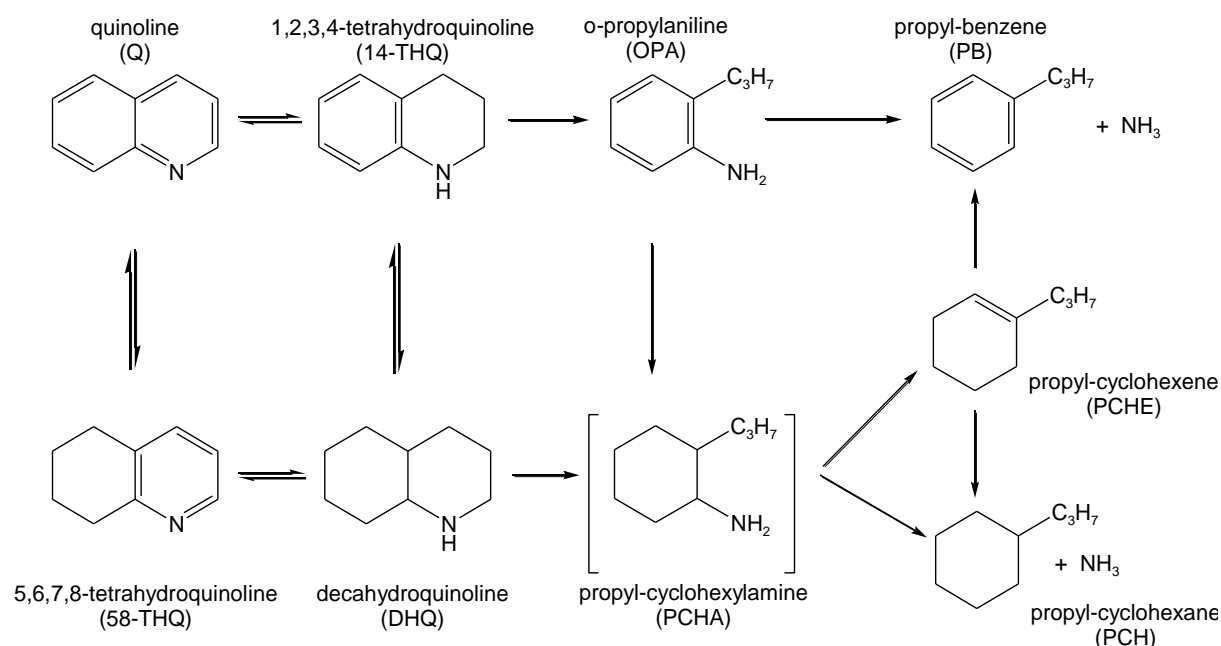


Figure 6. Quinoline HDN overall reaction network.

The initial hydrogenation reactions are all exothermic, with favorable equilibrium constants at low temperatures ($K > 1$, $\log K > 0$) that becomes unfavorable above 225 °C [39]. Higher hydrogen pressure can push the equilibrium towards saturated products. Hydrogenolysis reactions are less exothermic than the hydrogenation reactions because they demand less hydrogen. It should be pointed out that under industrial conditions the HDN reactions are irreversible since their equilibrium constants are large.

Beside the complexity of the reaction network there are couple of variables affecting the HDN rate such as hydrogen pressure, type of substituent, presence of hydrogen disulfide and hydrogen-donor liquids. Effect of hydrogen disulfide was studied for various model compounds. Satterfield et al. studied its influence on the quinoline HDN [26,38]. The study showed that the presence of H_2S , generated in situ from CS_2 , inhibits the hydrogenation and dehydrogenation reactions but significantly accelerates hydrogenolysis, increasing the overall rate of the HDN. Therefore existence of two types of active site was postulated, sulfur vacancies responsible for hydrogenation and hydrogenolysis and Brønsted acid sites, formed by dissociation of H_2S , responsible for hydrogenolysis and ring isomerization. The effect of tetraline was studied as well. Tetraline is hydrogen-donor model compound and it is expected that its presence in feed will enhance the HDN reaction rate. In contrary it was observed that tetraline inhibits overall HDN rate presumably by competitive adsorption with quinoline and intermediates.

5. Hydrotreating catalysts

Industrial hydrotreating is generally carried on transition metal sulfides (TMS) supported on $\gamma-Al_2O_3$ and promoted with Co or Ni. The use of TMS is coming from the early 1920's when urgent need for coal hydrogenation existed. Sabatier won the Nobel Prize in 1912 for describing the mechanism of hydrogenation by transition metals. Nevertheless during coal hydrogenation transition metals were transformed into more stable sulfides (TMS) due to the high content of sulfur-containing compounds in a feedstock. From these beginnings TMS catalysts became the basis of today's conventional $Co(Ni)Mo/\gamma-Al_2O_3$ hydrotreating catalysts.

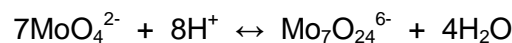
Since that time better understanding of fundamental properties of TMS has been developed [40]. Cobalt is used mainly as a promoter in the HDS while Ni is the choice for the HDN. In addition, hydrotreating catalysts often consist of incorporating elements such as phosphorus, boron, fluorine and chlorine. The overview of major refinery hydrotreating processes and different catalysts is given in Table 13 [41].

Process	Removal of	Catalyst
HDS	Sulfur (H ₂ S)	Co-MoS ₂ /Al ₂ O ₃ and Ni-WS ₂ /Al ₂ O ₃
HDN	Nitrogen (NH ₃)	Ni-MoS ₂ /Al ₂ O ₃ and Co-MoS ₂ /Al ₂ O ₃
HDO	Oxygen (H ₂ O)	Ni-MoS ₂ /Al ₂ O ₃
HDM	Metals (metal sulfides)	Ni-MoS ₂ /Al ₂ O ₃

Table 13. TMS catalysts used in industrial hydrotreating reactions [41].

5.1. Structure of the oxidic catalyst precursor

Hydrotreating catalyst oxidic precursors are usually prepared by incipient wetness impregnation or by coimpregnation of alumina support with a typical surface area from 2 to 3·10⁵ m²/kg, a pore volume of about 5·10⁻⁴ m³/kg and an average pore diameter of 10 nm [42]. Incipient wetness impregnation is commonly done with aqueous solution of ammonium heptamolybdate, and cobalt- or nickel-nitrate. It is preferred that impregnation is done in two steps so that after each step catalyst precursor is dried and calcined [43,44]. Alternatively and preferably in industry, all materials are coimpregnated and resulting material is dried and calcined [45]. The order of impregnation and calcination plays important role in the catalyst activity because if impregnated first, cobalt and nickel can form inactive spinels in alumina support. Impregnation of alumina from an aqueous solution of ammonium heptamolybdate, (NH₄)₆Mo₇O₂₄, can bring different molybdenum species on the support depending on the pH and concentration of the solution. Typical species that can occur are tetrahedral MoO₄²⁻ monomer or octahedral Mo₇O₂₄⁶⁻ heptaanion. The equilibrium between the two species is:



Depending on the isoelectric point (IEP), the support material can have positive polarization (molybdate anions are stabilized by forming Al-O-Mo bonds during drying and calcination procedure) and negative polarization (molybdate anions will not adsorb on the surface and during drying and calcination procedure will decompose to form MoO₃ crystals). Formation of MoO₃ will also occur when the total molybdate loading exceeds the monolayer capacity [46]. Table 14 presents the concentration of several surface metal oxides needed for monolayer formation on different support materials, obtained by Raman spectroscopy [47-50].

atoms/nm ²	Al ₂ O ₃	TiO ₂	ZrO ₂	Nb ₂ O ₅	SiO ₂
Re	2.3	2.4	3.3	-	0.54
Cr	4.0	6.6	9.3	-	0.6
Mo	4.6	4.6	4.3	4.6	0.3
W	4.0	4.2	4.0	3.0	0.1
V	7.3	7.9	6.8	8.4	0.7
Nb	4.8	5.8	5.8	-	0.3

Table 14. Monolayer surface coverage of metal oxides.

A structural characterization of supported transition metal oxides is difficult and two mostly used techniques are Raman and X-ray absorption spectroscopy. Influence of different supports such as TiO_2 , ZrO_2 , Nb_2O_5 , Al_2O_3 and SiO_2 was reported by Wachs et al. [51]. Medema et al. studied the structure of molybdenum and cobalt species as a function of their concentration [52], and Knözinger et al. later reported results on the effect of concentration and pH of molybdenum on alumina support [53,54].

5.2. Structure of sulfide catalyst

Oxidic catalyst precursors, formed by impregnation or coimpregnation, are transformed into actual active catalyst by sulfidation in different sulfiding agents. Properties of the final sulfided catalyst depend on the preparation method and calcination temperature. Optimum calcination and sulfidation temperatures are in the range of 400 to 500°C [32]. Sulfided structure is based on sulfur trigonal prisms that are coordinated to Mo. These sulfur prisms are two-dimensionally bonded to form S-Mo-S sandwiches that are weakly held by van-der Waals interactions along the c-axis forming highly anisotropic three-dimensional MoS_2 crystals [55].

Over the years, four different structural models have been proposed by different authors, i.e., monolayer model, pseudointercalation model, contact synergy model and “Co(Ni)MoS” phase model [16]. Monolayer model is based on the fact that molybdenum species are well dispersed as a monolayer on the alumina support. During sulfidation, this oxidic monolayer structure is converted to MoS_2 two-dimensional layers. Pseudointercalation model is based on the structure of bulk MoS_2 and contact synergy model of mixed sulfide catalyst explains promotion effect at the interface between two phases, i.e. MoS_2 and Co_9S_8 .

Existence of “CoMoS” phase was originally reported by Topsøe et al. [56]. It was suggested that the “CoMoS” phase is present as a single S-Mo-S sheet with Co decorating the edges while existing at the molybdenum sites. High MoS_2 edge dispersion is very important as it increases the amount of the promoter atom that can be accommodated to form the active “CoMoS” phase. Further studies showed existence of two types of “CoMoS” structure, type I and type II [57]. It was reported that type I “CoMoS” phase has lower activity per active site, it is formed at lower temperatures and it has some remaining Mo-O-Al link to the support. In contrary, type II “CoMoS” phase has higher activity per active site and it is formed at higher temperatures which can break all linkages with support material. However, it was found that sulfiding at high temperatures can lead to sintering and loss of important edge sites. In the latest studies Topsøe et al. were exploring the morphology of MoS_2 nanoclusters as a function of the sulfidation conditions using atom resolved scanning tunneling microscopy

(STM). Under the most sulfiding conditions ($\text{H}_2\text{S}:\text{H}_2 = 500$) MoS_2 clusters had triangular shape but under reducing conditions ($\text{H}_2\text{S}:\text{H}_2 = 0.07$) the shape was hexagonal [58]. The STM images provided detailed insight of the unusual sites with metallic-like character. These so-called brim sites, located at the edges of the nanoclusters, play a key role in the catalytic hydrotreating reactions [59].

5.3. Catalytic active sites

The existence of two types of active sites in the conventional hydrotreating catalyst was proposed by Satterfield et al. [36,38]. Sulfur vacancies responsible for hydrogenation and hydrogenolysis and Brønsted acid sites responsible for hydrogenolysis and ring isomerization. It was observed that H_2S increases the rate of DHQ ring opening towards propylcyclohexylamine (PCHA) that is quickly converted to propylcyclohexene (PCH) and ammonia and it increases the rate of 14THQ ring opening towards OPA. Nevertheless, denitrogenation of OPA was inhibited by the presence of hydrogen disulfide.

Great change in activity towards HDS of dibenzothiophene on the transition metal sulfides as a function of their position in the periodic table was observed by Pecoraro and Chianelli [60]. Interpretation of typical “volcano” curve helped understanding the catalytic properties of the hydrotreating catalysts. Fig. 8 (left) is showing the dependency of the HDS activity on the number of d-electrons for the 4d- and 5d-TMS. The 3d-TMS have more complex behavior [61,62]. The highest activity was observed for the TMS which have the maximum d-character, Ru and Os for the second and the third row of transition metals, respectively. It was concluded that these trends must be depending on the electronic configuration of d-orbitals.

The “volcano” curve was explained in terms of Sabatie’s principle. Compounds with a maximum activity for a given reaction have intermediate heat of formation. Therefore TMS with a maximum HDS activity will have the intermediate heat of formation. Fig. 8 (right) shows that the heat of formation, thus, the metal-sulfur bond strength in TMS decreases constantly across the periodic table. From 4d- and 5d-TMS, the most active catalysts have the heat of formation in the range of 30 to 55 kcal/mol. This implies that the metal-sulfur strength should not be too strong and not too weak to obtain high HDS rate. This postulate is in agreement with the generally established model of sulfur vacancies as catalytically active sites in the HDS and HDN reactions.

Studying the layered MoS_2 structure, Daage and Chianelli [63] proposed existence of two types of sites and pointed out the importance of stacking degree on HDS activity. According to this “rim-edge” model catalyst cluster is described as a stack of several layers. Top and

bottom layers contain sites occurring on their edges and they are defined as rim sites. Layers, sandwiched in-between, have only edge sites. The basal planes, away from the edge, are reported to be inert. Sulfur vacancies that are responsible for hydrogenolysis form faster at the edge because sulfur is bonded to one or two molybdenum ions in comparison to triply bonded molybdenum which exists on the basal plane. It was found that hydrogenation reaction is catalyzed on rim sites and hydrogenolysis reaction on edge sites.

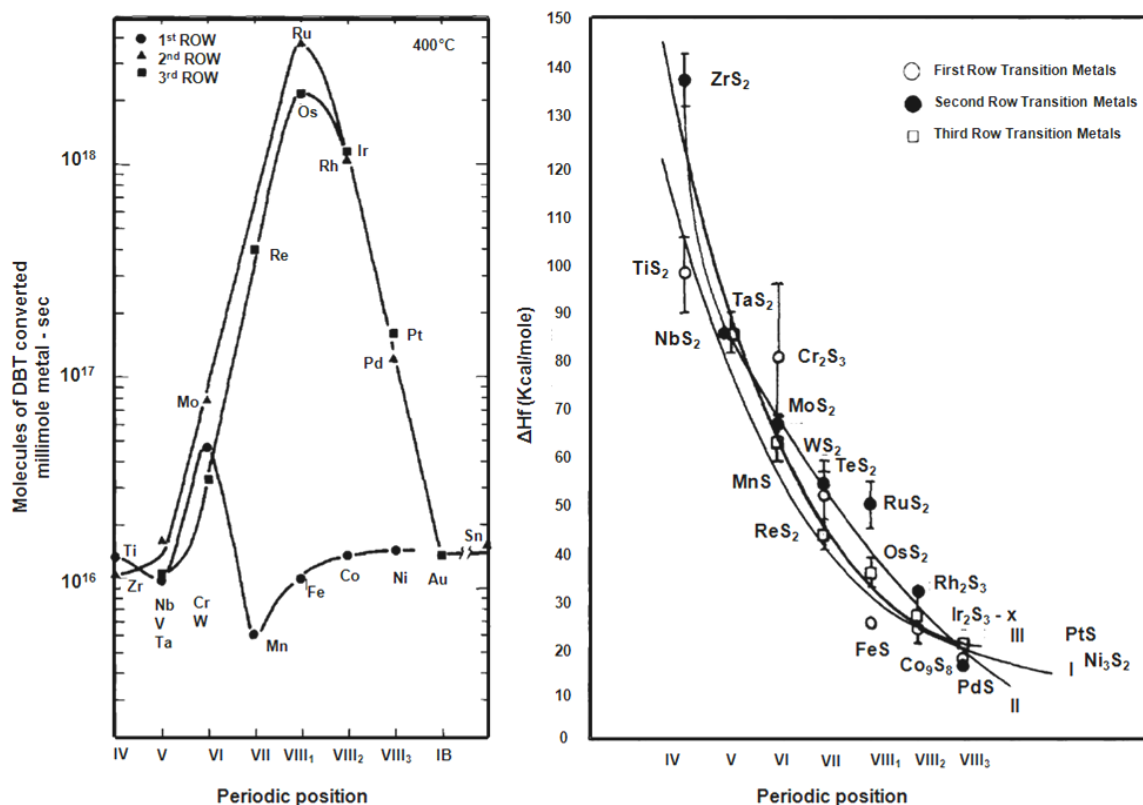


Figure 8. Periodic trends observed in HDS of DBT (left) and in Heat of formation of TMS (right) [60].

Studies were extended on the Co- and Ni-promoted TMS. Promoted “Co(Ni)MoS” catalysts have higher HDS activity compared to the pure MoS₂. Topsøe et al. calculated sulfur binding energies (energy needed for the first sulfur atom removal from the S-edge) for unpromoted and promoted MoS₂ catalysts, Table 15 [64]. The main role of Co and Ni promoter is concluded to be the creation of more vacancies.

ΔEs, kJ/mol	
MoS ₂	47
Co-Mo-S	-34
Ni-Mo-S	-35

Table 15. Sulfur binding energies (removal of the first S atom from the S-edge) [64].

5.4. Further development of hydrotreating catalysts

Hydrotreating catalysts often contain phosphate or fluorine as additives. Phosphates are added as phosphoric acid or ammonium phosphate into the molybdenum impregnating solution to enhance molybdenum solubility by complex formation and thus molybdenum loading can be increased. Many explanations have been given for the promotional effect of phosphorus in HDS and HDN, i.e., improved molybdenum and nickel or cobalt dispersion, different MoS₂ morphology, changes in the support acidity, chemical modifications of active sites and better resistance to coke formation [65].

Higher activity in HDS and HDN reactions can also be achieved by using other metal sulfides than the ones in conventional catalysts. The activity in quinoline HDN is increasing as follows: W < Mo < Ru, Pd < Rh < Re < Pt < Os < Ir [28,29]. Beside γ -Al₂O₃ support many groups studied effect of other support materials such as silica, silica-alumina, zeolites, activated carbon and titania. Pure silica gives lower activity for hydrotreating reactions while silica-alumina is better support for HDN. Carbon and titania have higher activity than alumina supported catalysts per mole of metal present.

Beside the sulfides, new catalysts such as metal carbides and nitrides were developed for use in the two stage hydrotreating processes. In this kind of configuration, the majority of sulfur containing compounds is removed in the first stage by conventional TMS catalysts. Relatively small amount of sulfur that is left is removed in the second stage process [32].

Recently unsupported transition metal catalysts were developed and potentially huge performance benefits were reported. The preparation methods are based on coprecipitation of oxide precursor [66-69] or on the direct precipitation of the sulfide. Although there is a large number of patents describing different unsupported catalytic systems there are only a few commercial bulk hydrotreating catalysts. Due to the high catalytic activity and the fact that reaction is exothermic, high amount of heat is released, the existing refinery process equipment would need to be redesigned. In addition, high concentration of metals would increase the price of the catalyst which would lead to uneconomic process [70].

Although unsupported catalysts didn't find wide industrial use, their study may be important. Supported catalytic systems are difficult to understand because of various phenomena that occur. One way to simplify the system is to eliminate support and its effects and therefore understanding of unsupported hydrotreating catalysts is essential for further improvement in HDS and HDN processes.

6. Scope of the thesis

Increasing demand for transportation fuels and more rigorous specifications for sulfur and nitrogen content have led to high interest in chemistry of light and heavy crude oil refining. As one of the key hydrotreating reactions, HDN has been extensively studied over past decades. Nevertheless many questions about the atomistic picture of the active sites responsible for various reaction steps still remained without straightforward answers. Thus, the main objective of the thesis is to better understand the active sites involved in HDN, in particular *o*-propylaniline (OPA), decahydroquinoline (DHQ) and quinoline, combining different catalyst characterization techniques and kinetic measurements.

A common introduction about hydrotreating chemistry is given in *Chapter 1*. The overview of the generally accepted networks and thermodynamic data of various model compounds are given for the HDS and HDN reactions. Structure of oxide precursors as well as sulfide industrial catalysts is described with a short indication of the active sites involved in reactions for a heteroatom removal.

The HDN of OPA (one of the key intermediates of quinoline HDN) on $\text{MoS}_2/\gamma\text{-Al}_2\text{O}_3$ and $\text{NiMoS}/\gamma\text{-Al}_2\text{O}_3$ catalysts is studied in *Chapter 2*. The impact of Ni on the catalytic properties of $\text{MoS}_2/\gamma\text{-Al}_2\text{O}_3$ is described. The effect of sulfur-containing compound, dibenzothiophene (DBT), on the catalytic activity and selectivity is explored. Overall, the evidence for the nature of the active sites responsible for different reaction routes, such as direct denitrogenation (DDN) via $\text{C}(\text{sp}^2)\text{-N}$ bond cleavage and hydrogenation, is given, using the sites titration and kinetic measurements.

The HDN of DHQ and quinoline on $\text{MoS}_2/\gamma\text{-Al}_2\text{O}_3$ and $\text{NiMoS}/\gamma\text{-Al}_2\text{O}_3$ catalysts is studied in *Chapter 3*. The effect of Ni as a promoter and the impact of DBT are described in detail. The emphasis is put on the active sites involved in the ring opening reaction of DHQ and 1,2,3,4-tetrahydroquinoline (14THQ) via $\text{C}(\text{sp}^3)\text{-N}$ bond cleavage. *Chapter 3* provides not only better understanding of the overall quinoline reaction network but also detailed description of the catalyst itself.

The preparation procedures of the supported $\text{Mo}/\gamma\text{-Al}_2\text{O}_3$ and $\text{NiMo}/\gamma\text{-Al}_2\text{O}_3$ as well as the unsupported NiMo precursors are given in *Chapter 4*. The structure of oxide precursors and sulfide catalysts is studied applying different characterization methods: BET, XRD, TEM, in-situ Raman, UV-vis, and in-situ X-ray adsorption spectroscopy, temperature programmed sulfidation (TPS) and NO adsorption. The effects of support, size and stacking degree of MoS_2 slabs on the quinoline HDN reaction are described for the above mentioned catalysts.

A summary of the most important results and conclusions is given in *Chapter 5*.

7. References

- [1] J.G. Speight, *The Chemistry and Technology of Petroleum*, Marcel Dekker (1999).
- [2] C. Song, C.S. Hsu, I. Mochida, *Chemistry of diesel fuels*, Taylor & Francis (2000).
- [3] <<http://www.dieselnet.com/standards/eu/fuel.php>>, 13.04.2010.
- [4] J.G. Speight, *The Desulfurization of Heavy Oils and Residua*, Marcel Dekker (2000).
- [5] H. Alboudwarej, J.J. Felix, S. Taylor, R. Badry, C. Bremner, B. Brough, C. Skeates, A. Baker, D. Palmer, K. Pattison, M. Beshry, P. Krawchuk, G. Brown, R. Calvo, J.A.C. Triana, R. Hathcock, K. Koerner, T. Hughes, D. Kundu, J.L. de Cardenas, C. West, *Highlighting Heavy Oil*, <<http://www.heavyoilinfo.com>>, 13.04.2010.
- [6] H. Topsøe, B.S. Clausen, F.E. Massoth, *Hydrotreating Catalysis, Science and Technology*, Springer, New York, (1991).
- [7] J.A. Moulijn, M. Makkee, A. Van Diepen, *Chemical Process Technology*, John Wiley & Sons, (2001).
- [8] E. Furimsky, F. E. Massoth, *Catal. Rev.* 47 (2005) 297.
- [9] J. Ancheyta, J.G. Speight, *Hydroprocessing of Heavy Oils and Residua*, Taylor & Francis, (2007).
- [10] J.R. Katzer, R. Sivasubramanian, *Catal. Rev. Sci. Eng.* 20 (1979) 155.
- [11] A.S. Eigenson, E.G. Ivchenko, *Chem. Tech. Fuels Oils* 13 (1977) 542.
- [12] H. Topsøe, B.S. Clausen, F.E. Massoth, *Hydrotreating Catalysis*, Springer, (1996).
- [13] S.C. Schuman, H. Shalit, *Catal. Rev.* 4 (1971) 245.
- [14] R. Prins, M. Egorova, A. Röthlisberger, Y. Zhao, N. Sivasankar, P. Kukula, *Catal. Today* 111 (2006) 84.
- [15] M. Egorova, R. Prins, *J. Catal.* 225 (2004) 417.
- [16] Teh C. Ho, *Catal. Rev. Sci. Eng.* 30 (1988) 117.
- [17] G.W. Mushrush, E.J. Beal, D.R. Hardy, J.M. Hughes, *Fuel Process. Technol.* 61 (1999) 197.
- [18] Y. Zhao, R. Prins, *J. Catal.* 229 (2005) 213.
- [19] M. Egorova, R. Prins, *J. Catal.* 221 (2004) 11.
- [20] M. Egorova, Y. Zhao, P. Kukula, R. Prins, *J. Catal.* 206 (2002) 263.
- [21] M. Egorova, R. Prins, *J. Catal.* 241 (2006) 162.
- [22] E.W. Stern, *J. Catal.* 57 (1979) 390.
- [23] F.E. Massoth, K. Balusami, J. Shabtai, *J. Catal.* 122 (1990) 256.
- [24] A. Bunch, L. Zhang, G. Karakas, U.S. Ozkan, *Appl. Catal. A* 190 (2000) 51.
- [25] S.C. Kim, F.E. Massoth, *J. Catal.* 189 (2000) 70.
- [26] S.H. Yang, C.N. Satterfield, *J. Catal.* 81 (1983) 168.

- [27] H.A. Rangwala, I.G. Dalla Lana, F.D. Otto, H. Yeniova, K. Al-Nuaimi, *Energy & Fuels* 4 (1990) 599.
- [28] S. Eijsbouts, C. Sudhakar, V.H.J. de Beer, R. Prins, *J. Catal.* 127 (1991) 605.
- [29] S. Eijsbouts, V.H.J. de Beer, R. Prins, *J. Catal.* 127 (1991) 619.
- [30] R. Prins, M. Jian, M. Flechsenhar, *Polyhedron* 16 (1997) 3235.
- [31] R.Z. Lee, M. Zhang, F.T.T. Ng, *Top. Catal.* 37 (2006) 121.
- [32] R. Prins, *Adv. Catal.* 46 (2001) 399.
- [33] C.N. Satterfield, M. Modell, R.A. Hites, C.J. Declerck, *Ind. Eng. Chem. Process Des. Dev.* 17 (1978) 141.
- [34] J.F. Cocchetto, C.N. Satterfield, *Ind. Eng. Chem. Process Des. Dev.* 20 (1981) 49.
- [35] C.N. Satterfield, J.F. Cocchetto, *Ind. Eng. Chem. Process Des. Dev.* 20 (1981) 53.
- [36] C.N. Satterfield, S. Gültekin, *Ind. Eng. Chem. Process Des. Dev.* 20 (1981) 62.
- [37] C.N. Satterfield, S.H Yang, *Ind. Eng. Chem. Process Des. Dev.* 23 (1984) 11.
- [38] S.H Yang, C.N. Satterfield, *Ind. Eng. Chem. Process Des. Dev.* 23 (1984) 20.
- [39] J.F. Cocchetto, C.N. Satterfield, *Ind. Eng. Chem. Process Des. Dev.* 15 (1976) 272.
- [40] R.R. Chianelli, *Oil Gas Sci. Technol.* 61 (2006) 503.
- [41] I. Chorkendorff, J.W. Niemantsverdriet, *Concepts of Modern Catalysis and Kinetics*, WILEY-VCH, (2007).
- [42] G.C.A. Schuit, B.C. Gates, *AIChE Journal* 19 (1973) 417.
- [43] X Li, A. Wang, M. Egorova, R Prins, *J. Catal.* 250 (2007) 283.
- [44] B.S. Clausen, H. Topsøe, R. Candia, J. Villadsen, B. Lengeler, J. Als-Nielsen, F. Christensen, *J. Phys. Chem.* 85 (1981).
- [45] H. Topsøe, B.S. Clausen, R. Candia, C. Wivel, S. Mørup, *J. Catal.* 68 (1981) 433.
- [46] G. Ertl, H. Knözinger, J. Weitkamp, *Handbook of Heterogeneous Catalysis*, WILEY-VCH, (1997).
- [47] I.E. Wachs, *Catal. Today* 27 (1996) 437.
- [48] M.A. Vuurman, D.J. Stufkens, A. Oskam, I.E. Wachs, *J. Mol. Catal.* 76 (1992) 263.
- [49] G. Deo, I.E. Wachs, *J. Catal.* 146 (1994) 323.
- [50] J.-M. Jehng, I.E. Wachs, *J. Mol. Catal.* 67 (1991) 369.
- [51] H. Hu, I.E. Wachs, S.R. Bare, *J. Phys. Chem.* 99 (1995) 10897.
- [52] J. Medema, C. Van Stam, V.H.J. de Beer, A.J.A. Konings, D.C. Koningsberger, *J. Catal.* 53 (1978) 386.
- [53] H. Knözinger, H. Jezlorowski, *J. Phys. Chem.* 82 (1978) 2002.
- [54] H. Jezlorowski, H. Knözinger, *J. Phys. Chem.* 83 (1979) 1166.
- [55] R.R. Chianelli, M.H. Siadati, M.P. De la Rosa, G. Berhault, J.P. Wilcoxon, R. Bearden Jr, B.L. Abrams, *Catal. Rev.* 48 (2006) 1.
- [56] H. Topsøe, B.S. Clausen, *Catal. Rev. Sci. Eng.* 26 (1984) 395.

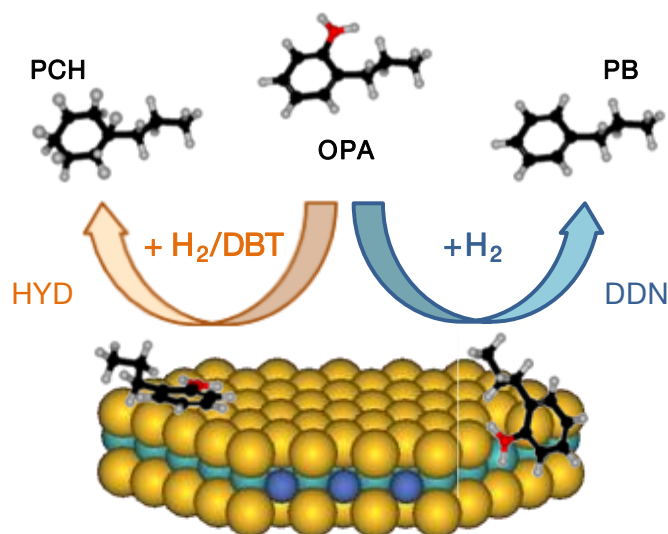
- [57] H. Topsøe, B. Hinnemann, J.K. Nørskov, J.V. Lauritsen, F. Besenbacher, P.L. Hansen, G. Hytoft, R.G. Egeberg, K.G. Knudsen, *Catal. Today* 107-108 (2005) 12.
- [58] J.V. Lauritsen, M.V. Bollinger, E. Laegsgaard, K.W. Jacobsen, J.K. Nørskov, B.S. Clausen, H. Topsøe, F. Besenbacher, *J. Catal.* 221 (2004) 510.
- [59] H. Topsøe, *Appl. Catal. A* 322 (2007) 3.
- [60] T.A. Pecoraro, R.R. Chianelli, *J. Catal.* 67 (1981) 430.
- [61] H. Topsøe, B.S. Clausen, N.-Yu Topsøe, J. Hyldtoft, Symposium on the Mechanism of HDS/HDN Reactions, 206th National meeting, American Chemical Society, (1993).
- [62] H. Topsøe, B.S. Clausen, N.-Yu Topsøe, J.K. Nørskov, C.V. Ovesen, C.J.H. Jacobsen, *Bull. Soc. Chim. Belg.* 104 (1995) 283.
- [63] M. Daage, R.R. Chianelli, *J. Catal.* 149 (1994) 414.
- [64] L.S. Byskov, J.K. Nørskov, B.S. Clausen, H. Topsøe, Sulphur bonding in transition metal sulphides and MoS₂ based structures, in T. Weber, R. Prins, R.A. van Santen (eds.), *Transition Metal Sulphides – Chemistry and Catalysis*, Kluwer Academic Publishers, (1998).
- [65] V. Sundaramurthy, A.K. Dalai, J. Adjaye, *Appl. Catal. A* 311 (2006) 155.
- [66] US 2009/0107883 A1.
- [67] WO 2007/050636 A2.
- [68] WO 2007/050633 A2.
- [69] WO 2006/036610 A1.
- [70] S. Eijsbouts, S.W. Mayo, K. Fujita, *Appl. Catal. A* 322 (2007) 58.

Chapter 2

Selective poisoning of the direct denitrogenation route in the o-propylaniline HDN by DBT on Mo and NiMo/ γ -Al₂O₃ sulfide catalysts

The hydrodenitrogenation of o-propylaniline on MoS₂/ γ -Al₂O₃ and NiMoS/ γ -Al₂O₃ catalysts proceeds via two parallel routes, i.e., direct denitrogenation (DDN) by C(sp²)-N bond cleavage to form propylbenzene and hydrogenation (HYD) of the phenyl ring to form propylcyclohexylamine, followed by C(sp³)-N bond cleavage. Coordinatively unsaturated sites (CUS) at the edges of the sulfide slabs are catalytically active for the DDN. Dibenzothiophene (DBT) decreases the DDN rate while it is mainly converted via direct desulfurization. Adding Ni to MoS₂ increases the CUS concentration and promotes the HYD but inhibits the DDN, suggesting that Ni cations are not involved in the active sites for DDN route. Catalytically active sites for the HYD route are the sites at the basal plane near the edges of the sulfide slabs (brim sites). The presence of DBT strongly increases the HYD rate on NiMoS/ γ -Al₂O₃, increasing the electron density at the brim sites due the electron pair donor properties of DBT and biphenyl.

1. Graphical abstract



The HDN of o-propylaniline on MoS₂/γ-Al₂O₃ and NiMoS/γ-Al₂O₃ catalysts proceeds via two parallel routes on two separate sites. Direct denitrogenation (DDN) is catalyzed only by accessible Mo cations, while the sites at the basal plane near the edge of the sulfide slabs (brim sites) are active for hydrogenation (HYD).

2. Introduction

As one of the key hydrotreating reactions, hydrodenitrogenation (HDN) on sulfide-based catalysts has been studied extensively, because of its complexity and inhibiting effects on other hydrotreating reactions. Despite these efforts it is still difficult to unequivocally establish an atomistic picture of the active sites involved in the various elementary steps of HDN [1].

Although basic nitrogen-containing compounds adsorb readily onto the acidic surface of the sulfides and the support, it is not likely that every sorbate will lead to reaction and in turn reactants and products may inhibit certain pathways. Thus, better knowledge of the active sites is expected to lead to a more specific optimization of hydrotreating catalysts. With this in mind we attempt in the present contribution to specify the sites active for HDN, in particular of o-propylaniline (OPA), a key intermediate in the HDN of quinoline.

MoS₂, which is the basis of most HDN catalysts, is built up by trigonal sulfur prisms coordinated to Mo, which are, in turn, two-dimensionally bound, forming S-Mo-S sandwiched structures. These slabs exhibit two different active edges, so-called Mo-edge and S-edge. The nano-crystalline MoS₂ slabs are weakly held together by van-der Waals interactions

along the c-axis. The degree of stacking of the S-Mo-S layers depends on the synthesis conditions, metal loading, and surface area of the used support material.

Upon addition of Co and Ni, the Mo cations are substituted at the edge positions of the MoS₂ slabs. This substitution of Mo cations by the divalent cations is believed to be crucial in the creation of new and more active catalytic sites [2,3]. Recent DFT studies show that Co and Ni substitutions are favorable at the S-edge and Mo-edge, respectively [4,5]. Co as a promoter is predominantly located in a tetrahedral coordination, while Ni exists in a square-planar environment and under typical hydrotreating conditions, the equilibrium morphology for CoMoS and NiMoS are close to hexagon and deformed hexagon, respectively [6]. Upon substitution, sulfur vacancies are formed, i.e., coordinatively unsaturated sites (CUS), because the sulfur binding energy decreases in the order MoS₂ > CoMoS > NiMoS [7], thus reducing the equilibrium sulfur coverage and increasing the concentration of accessible metal cations. Electron-rich zones have been identified on the basal plane in model catalysts by high-resolution scanning tunneling microscopy and have been associated with metal-like states [8,9].

While it is considered that the direct removal of sulfur and nitrogen atoms by CUS sites proceed via a reverse Mars-van Krevelen mechanism (the S or N atom, initially in the molecule, remains in the catalyst surface after the reaction), the sites involved in hydrogenation reactions are less understood. In essence, the hydrogenation involving CUS sites at the edge, sites at the basal plane near the edge (brim sites) and sites that combine both have been proposed [10-12]. The role of the promoter is on the one hand to increase the concentration of sulfur vacancies (CUS, accessible metal cations) and on the other hand to increase the electron density at the brim sites [13]. Both factors may influence the activity and selectivity of the HDN reaction and we will therefore attempt to relate the observed reaction pathways to these two sites or their combination.

The HDN of quinoline [14-21] has been explored frequently over the last decades, because of its bicyclic nature, which allows exploring all elementary HDN steps. The reaction starts with the hydrogenation of the pyridinic ring followed by ring opening via C(sp³)-N bond cleavage forming OPA, followed by direct nitrogen removal (DDN) or hydrogenation of benzoic ring followed by nitrogen removal either by ammonia elimination or by substitution of NH₂ by -SH and further C-S hydrogenolysis. In order to better understand the critical reaction steps in the overall sequence, this study is focused on the HDN of the key intermediate o-propylaniline. Competitive adsorption of various basic nitrogen-containing intermediates is so avoided ensuring the absence of additional inhibition effects. The OPA

HDN proceeds via hydrogenation of the aromatic ring and aliphatic C(sp³)-N bond cleavage (HYD), as well as direct aromatic C(sp²)-N bond cleavage (DDN).

In this contribution the HDN of OPA on MoS₂/γ-Al₂O₃ and NiMoS/γ-Al₂O₃ sulfide catalyst is explored. The aim of the paper is to address the impact of Ni on the catalytic properties of MoS₂ and to study the impact of sulfur-containing compounds (using dibenzothiophene) on the catalytic activity and selectivity. Overall, it is aimed to provide evidence for the nature of the active sites responsible for different reaction routes using titration of sites and kinetic measurements.

3. Experimental

3.1. Catalyst preparation

The supported Mo and NiMo oxide catalyst precursors were prepared by incipient wetness impregnation of γ-Al₂O₃. Prior to impregnation, the support was dried at 120 °C and then calcined at 560 °C for 2 h in synthetic air flow. At first, molybdenum was impregnated using an aqueous solution of ammonium heptamolybdate, (NH₄)₆Mo₇O₂₄·4H₂O (Aldrich). After impregnation, the catalyst was dried overnight at 120 °C in static air atmosphere and then thermally treated at 500 °C for 4 h (heating rate 1 °C/min) in flowing synthetic air [22]. One part of the prepared Mo catalyst was kept as precursor for kinetic experiments, and the other was used as a support for further nickel impregnation with an aqueous solution of nickel nitrate, Ni(NO₃)₂·6H₂O (Aldrich) [23]. After impregnation, the NiMo catalyst was dried and thermally treated as in case of the Mo catalyst.

3.2. Catalyst characterization

Physicochemical properties. The BET surface area and pore size distribution were determined by N₂ adsorption-desorption at -196 °C using a PMI Automated BET Sorptomatic 1900 Series instrument. Prior to the adsorption, the samples were evacuated at 250 °C for 2 h. Elemental analysis was carried out in the Microanalytical Laboratory at the TU München.

X-ray diffraction (XRD). The crystalline structure of the catalysts was determined by powder X-ray diffraction. XRD patterns were collected with a Philips X'Pert System (Cu-Kα radiation, 0.1542 nm), using a nickel K_β-filter and solid-state detector (X'Celerator). The operating conditions were 45 kV/40 mA. The measurements were carried out in a range from 5° to 70° 2θ with a step size of 0.017° and scan time of 115 s per step.

Transmission electron microscopy (TEM). Sulfided catalysts were ground, suspended in ethanol, and ultrasonically dispersed. Dispersion drops were applied on a copper-carbon grid. Measurements were carried out on transmission electron microscope device JEOL JEM-2011 with an accelerating voltage of 120 keV.

Raman spectroscopy. Raman spectra of oxide precursors and sulfided catalysts were obtained with a Renishaw Raman Spectrometer (Type 1000), equipped with CCD detector and Leica microscope, using 514 nm Ar laser. Prior to the measurements, calibration was done with Si (111) crystal. The wavenumber accuracy was within 1 cm^{-1} . Oxidic catalyst precursors were analyzed under ambient conditions, and therefore, the samples were pressed into self-supported wafers and placed onto a quartz sample holder. The used sulfide catalyst was analyzed using a diode 785 nm laser.

Temperature-programmed sulfidation (TPS). To study the influence of nickel as a promoter on the sulfidation mechanism, catalyst activation was performed by temperature-programmed reaction/sulfidation (TPS). The oxide precursor (0.1 g) was placed in the flow reactor equipped with a ceramic oven (Horst GmbH). The activation was performed in 10% H_2S in H_2 with a heating rate of $5 \text{ }^\circ\text{C}/\text{min}$. At $400 \text{ }^\circ\text{C}$, the temperature was held isothermally for 1 h. Evolved gases were detected by a mass spectrometer (Balzers QME 200).

NO adsorption. NO adsorption was applied to probe the active sites and average edge dispersion in the supported metal sulfide catalysts, such as unpromoted $\text{MoS}_2/\gamma\text{-Al}_2\text{O}_3$ and promoted $\text{NiMoS}/\gamma\text{-Al}_2\text{O}_3$. NO adsorption was performed as a flow pulse experiment at room temperature. After activation in 10% H_2S in H_2 at $400 \text{ }^\circ\text{C}$, the catalyst was cooled to room temperature in the presence of the sulfiding agent. Then, the catalyst was flushed with high purity He for 1 h. Pulses of 10% NO in He were injected every 0.5 h to determine the concentration of adsorbed NO on the sulfided catalyst. Evolved gases were detected by a Balzers mass spectrometer. The mixture ensured a pulse size of $7.5 \text{ } \mu\text{mol NO}/\text{pulse}$. Injections were repeated until adsorption was not longer detected. NO adsorption was calculated as the difference between the NO signal at a given pulse and an NO signal at which adsorption was not observed. The total concentration of NO adsorbed ($\mu\text{mol per 1 g catalyst}$) was calculated as the sum of the individual NO uptakes per pulse [24,25].

3.3. Kinetic test

Kinetic studies were carried out in a continuous flow fixed-bed reactor system. The stainless steel, glass-lined coated reactor was loaded with 0.05 g of catalyst, diluted in 1 g SiC, for each run, and the HDN reaction was performed at constant temperature, pressure, and feed

composition. Gas and liquid feed were introduced to the reactor via high pressure mass flow meters (Bronkhorst) and a HPLC pump (Shimadzu LC-20AD), respectively. After separation of liquid and gas effluent phase, the liquid was collected via a 16 port sampling valve every 1.5 h. The liquid samples were analyzed by off-line gas chromatography with a HP 6890 GC instrument equipped with a flame ionization detector (FID) and 60 m long DB-17 capillary column (Agilent, 0.25 mm i.d., 0.25 μm film thickness). The reproducibility of the measurements was $\pm 5\%$.

Prior to the kinetic experiments, the catalysts were activated in situ in 10% H_2S in H_2 flow at 400 $^\circ\text{C}$ and 1.8 MPa for 8 h. After cooling to room temperature in the sulfiding agent, the catalysts were flushed with hydrogen and the liquid feed flow. The reaction temperature was set to 370 $^\circ\text{C}$ and the total pressure to 5.0 MPa. The kinetic study was obtained from the samples taken after 16 h time on stream (TOS).

HDN was investigated as a function of space time. Space time was based on the OPA feed rate only and is defined as $m_{\text{cat}}/F_{\text{OPA}}$, where m_{cat} is the amount of the oxide catalyst precursor and F_{OPA} is the molar flow of OPA [(h) \cdot (g of catalyst)/(mol of OPA)]. Reactions were performed in great excess of hydrogen, keeping the ratio of liquid and gas flow constant to ensure constant partial pressures. The H_2/HC value is 330 Ndm^3/dm^3 , whereas the H_2/OPA molar ratio is approximately 220. The initial OPA partial pressure was 17.9 kPa in a mixture of hexadecane and tetradecane as a solvent. To study the effect of dibenzothiophene (DBT) on OPA HDN, feed with different DBT partial pressures were used: 0, 1.7, 3.4, and 5.1 kPa. To determine the hydrogenation to dehydrogenation ratio, ethylbenzene or ethylcyclohexane was added (4.4 kPa).

In order to better understand the impact of DBT on the OPA HDN carried out on $\text{NiMoS}/\gamma\text{-Al}_2\text{O}_3$, an independent set of experiments was performed at identical reaction conditions ($T= 370\text{ }^\circ\text{C}$, $p= 5.0\text{ MPa}$) and the space time of 82 $\text{h}\cdot\text{g}_{\text{cat}}/\text{mol}$. After catalyst activation, as described previously, the reaction was performed applying the feed containing only 17.9 kPa OPA. After 16 h time on stream, the steady state was reached, and 3.4 kPa of DBT was cofed into the reactor. Finally, DBT was removed, after 6 h TOS, and the reaction was run for further 24 h in a feed containing only OPA. During the transient time, the product analysis was performed more frequently to ensure appropriate following of the concentration profile.

The stability of the $\text{NiMoS}/\gamma\text{-Al}_2\text{O}_3$ catalyst was studied to understand the deactivation when the OPA HDN is carried out in the absence of DBT. After activation, as described earlier, the catalyst was reduced under reaction conditions of temperature and pressure (370 $^\circ\text{C}$ and 5 MPa) in pure H_2 for 2, 6, and 10 h. Then, the liquid phase containing only OPA (17.9 kPa)

was introduced into the reactor with the space time of 82 h·g_{cat}/mol. The product analysis was performed every 5 min in the first hour and further on every hour.

The conversion of OPA to nitrogen-free products is referred to as the HDN conversion and is calculated according to the equation:

$$\text{OPA HDN conversion} = \frac{C_{[\text{OPA}]_0} - C_{[\text{OPA}]} - C_{[\text{N}]}}{C_{[\text{OPA}]_0}}$$

where $C_{[\text{OPA}]_0}$ and $C_{[\text{OPA}]}$ are the OPA concentrations at time zero and at the measured space time and $C_{[\text{N}]}$ is the concentration of all nitrogen-containing intermediates at the measured space time. As nitrogen-containing intermediates were not detected, the OPA HDN conversion was equal to the total OPA conversion.

The determination of the OPA HDN reaction order was done using the integral method, applying appropriate concentration-space time dependency. The following power law model was used:

$$-r = \frac{dp_{[\text{OPA}]}}{dt} = k \cdot p_{[\text{OPA}]}^n \cdot p_{[\text{H}_2]}^m$$

where r is the rate of the OPA HDN reaction, k the apparent rate constant, $p_{[\text{OPA}]}$ the partial pressure of OPA, $p_{[\text{H}_2]}$ the partial pressure of hydrogen, t the space time based on OPA feed rate, n the reaction order in OPA, and m is the reaction order in hydrogen. Considering that reaction is carried out in great excess of hydrogen (H_2 partial pressure is considered constant), the rate expression can be simplified as:

$$-r = \frac{dp_{[\text{OPA}]}}{dt} = k' \cdot p_{[\text{OPA}]}^n$$

where k' is the apparent rate constant that includes the factor of the hydrogen partial pressure. Calculation of the rate constants for the proposed mechanism was carried out by the Berkeley Madonna 7.0 program using the Runge-Kutta integration method.

Temperature-dependent experiments were performed in absence and presence of 3.4 kPa DBT to determine the apparent energy of activation for the OPA HDN on unpromoted $\text{MoS}_2/\gamma\text{-Al}_2\text{O}_3$ and promoted $\text{NiMoS}/\gamma\text{-Al}_2\text{O}_3$ catalysts. The temperature range studied was from 330 to 390 °C with 20 °C step. The total pressure was 5 MPa and the space time of 82 h·g_{cat}/mol was chosen in order to obtain low OPA conversions. The apparent activation

energies were calculated from a semilogarithmic plot of $\ln k'$ vs. $1/T$, using the Arrhenius equation:

$$\ln k' = \ln A - \frac{E_a}{RT}$$

where E_a is the apparent activation energy (kJ/mol), A is the pre-exponential factor, R is the molar gas constant ($R= 8.314 \text{ J}/(\text{mol K})$), and T is the absolute temperature (K).

4. Results

4.1. Catalyst characterization

4.1.1. Physicochemical properties

An overview of the physicochemical characteristics of the materials applied in this study is given in Table 1. The specific surface area of $\gamma\text{-Al}_2\text{O}_3$ support was $237 \text{ m}^2/\text{g}$. The Mo concentration in the oxide precursor was 8.6 wt.%, which corresponds to 2.5 Mo atoms/nm². The Ni concentration was 3.6 wt.% leading to a molar fraction of 0.4 Ni in the bimetallic catalyst precursor.

Catalyst	Metal concentration wt.% ($\mu\text{mol}/\text{g}$)		Surface area m^2/g	Pore volume cm^3/g	Pore diameter nm
	Mo	Ni			
$\gamma\text{-Al}_2\text{O}_3$	-	-	237	0.75	8.5
Mo/ $\gamma\text{-Al}_2\text{O}_3$	8.6 (895)	-	220	0.62	8.5
NiMo/ $\gamma\text{-Al}_2\text{O}_3$	8.6 (895)	3.6 (610)	206	0.60	8.5

Table 1. Physicochemical properties of the $\gamma\text{-Al}_2\text{O}_3$ support and the oxidic catalyst precursors.

4.1.2. X-ray diffraction (XRD)

Oxidic catalyst precursors, Mo/ $\gamma\text{-Al}_2\text{O}_3$ and NiMo/ $\gamma\text{-Al}_2\text{O}_3$, did not show any additional diffraction reflections except the ones characteristic for the used support material ($37, 39, 46, 61$ and $67^\circ 2\theta$), Fig. 1 (A) and (B). Thus, after molybdenum and nickel impregnation, new crystalline phases were not observed. The sulfided catalysts exhibited two diffraction peaks at around 33 and $59^\circ 2\theta$ characteristic for the interplanar distances of 2.7 and 1.5 \AA of the MoS_2 crystalline structure [26]. The diffraction peak at $14^\circ 2\theta$, characteristic for the (002) plane with interplanar distance of 6.1 \AA , was not observed probably due to the low degree of stacking in the formed MoS_2 and NiMoS particles, Fig. 1 (C) and (D).

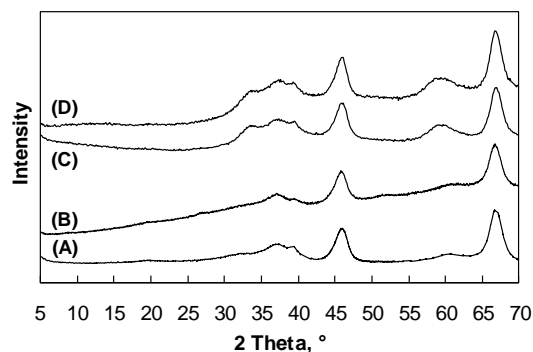


Figure 1. X-ray diffraction patterns of: (A) γ - Al_2O_3 , (B) $\text{Mo}/\gamma\text{-Al}_2\text{O}_3$, (C) $\text{MoS}_2/\gamma\text{-Al}_2\text{O}_3$, and (D) $\text{NiMoS}/\gamma\text{-Al}_2\text{O}_3$ catalysts.

4.1.3. Transmission electron microscopy (TEM)

Fig. 2 presents the TEM micrographs of the sulfided catalysts. The catalysts revealed the presence of typical layer like MoS_2 phase. The observed stacking did not exceed three layers confirming a good dispersion of the sulfided slabs on the $\gamma\text{-Al}_2\text{O}_3$ support as suggested by XRD.

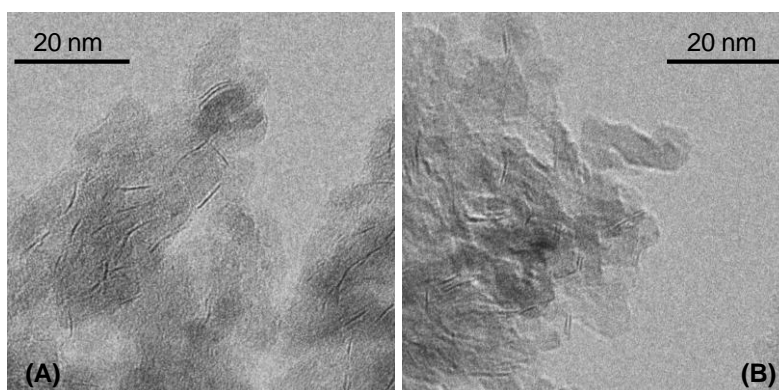


Figure 2. TEM micrographs of sulfided (A) $\text{MoS}_2/\gamma\text{-Al}_2\text{O}_3$, and (B) $\text{NiMoS}/\gamma\text{-Al}_2\text{O}_3$ catalysts.

4.1.4. Raman spectroscopy

The Raman spectra of the oxidic catalyst precursors are shown in Fig. 3 (A). The Raman spectrum of $\text{Mo}/\gamma\text{-Al}_2\text{O}_3$ catalyst exhibits bands at 961, 860, 350, and 224 cm^{-1} . These vibrations are assigned to the stretching of terminal $\text{Mo}=\text{O}$, asymmetric stretching of bridging $\text{Mo}-\text{O}-\text{Mo}$, bending of terminal $\text{Mo}=\text{O}$ and deformation of bridging $\text{Mo}-\text{O}-\text{Mo}$ bonds, respectively [27]. Due to the position of the highest frequency vibration and the presence of the characteristic bridging $\text{Mo}-\text{O}-\text{Mo}$ bond vibration, it is proposed that the surface molybdenum species are present as polymolybdates [28]. After nickel impregnation, the Raman band corresponding to the terminal $\text{Mo}=\text{O}$ symmetric stretching vibration was shifted downwards from 961 to 947 cm^{-1} . The shoulder at 860 cm^{-1} assigned to the asymmetric stretching vibration of $\text{Mo}-\text{O}-\text{Mo}$ bridging bond became more intense.

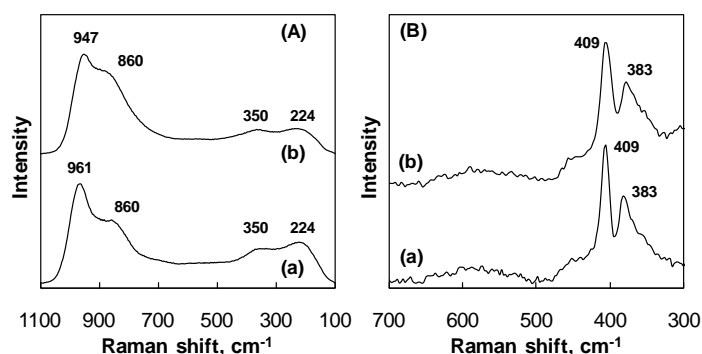


Figure 3. Raman spectra of (A) oxidic catalyst precursors and (B) sulfided catalysts: (a) Mo/ γ -Al₂O₃, and (b) NiMo/ γ -Al₂O₃.

Raman spectra of the sulfided catalysts are given in Fig. 3 (B). The bands related to the MoS₂ phase are found in both samples: 383 and 409 cm⁻¹, corresponding to Mo-S vibration along the basal plane and S-Mo-S vibration along the c-axis, respectively [29,30].

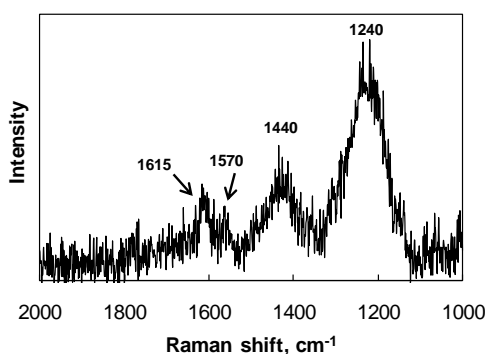


Figure 4. Raman spectrum of a used NiMoS/ γ -Al₂O₃ catalyst in the HDN of OPA in the absence of DBT.

At the end of the stability test described in section 4.2.4. (HDN of OPA in the absence of DBT), the used NiMoS/ γ -Al₂O₃ catalyst was carefully washed with n-hexane and i-propanol, dried, and analyzed by means of Raman spectroscopy and elemental analysis. As shown in Fig. 4, the Raman spectrum of the used NiMoS/ γ -Al₂O₃ catalyst exhibited bands at around 1240, 1440, 1570, and 1615 cm⁻¹. These weak bands can be related to polymeric aniline [31], suggesting the presence of N-containing coke. The precise assignment of the bands is difficult because the defined structure of the coke formed is not known; however, the elemental analysis of the used samples confirmed the presence of C and N in 1.93 and 0.16 wt.%, which corresponds to a C/N molar ratio of 14.

4.1.5. Temperature-programmed sulfidation (TPS)

The rate of sulfidation was followed by temperature-programmed reaction (10% H₂S in H₂) increasing the temperature by 5 °C/min. As previously established by Nag [32] and Arnoldy [33], the sulfidation mechanism is governed by oxygen for sulfur exchange reactions leading

the oxide catalyst transformation through the oxy-sulfides to the fully sulfided species. The presence of three characteristic sections during sulfidation was common for the monometallic Mo/ γ -Al₂O₃ and bimetallic NiMo/ γ -Al₂O₃ catalyst, see Fig. 5. In the first section, oxygen is exchanged for sulfur bonded to Mo⁶⁺, as observed by H₂S consumption and parallel H₂O production. The temperature of the maximum H₂S consumption remained 120 °C for both Mo/ γ -Al₂O₃ and NiMo/ γ -Al₂O₃ catalysts. The second region is characteristic by the evolution of H₂S, which is paralleled/followed by H₂ consumption, which is used for the molybdenum reduction to Mo⁴⁺. Introduction of Ni into the catalyst shifted the reduction temperature from 225 °C for the monometallic Mo/ γ -Al₂O₃ catalyst to 205 °C for the bimetallic NiMo/ γ -Al₂O₃ catalyst. The consumption of H₂S in the third section indicates further oxygen for sulfur exchange on Mo⁴⁺, leading to the fully sulfided catalyst.

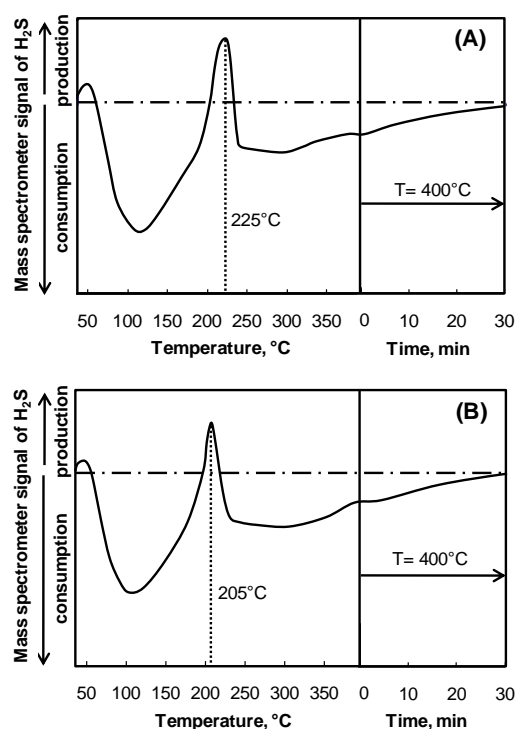


Figure 5. H₂S profile and characteristic Mo reduction temperatures during activation of (A) unpromoted Mo/ γ -Al₂O₃ (225 °C) and (B) promoted NiMo/ γ -Al₂O₃ (205 °C) catalyst in 10% H₂S in H₂.

4.1.6. NO adsorption

NO preferentially adsorbs on coordinatively unsaturated metal cations at the edge sites of the sulfide particles [24]. Molybdenum Mo⁶⁺ cations do not adsorb NO strongly because they have a d⁰ configuration, which does not allow the accommodation of the unpaired antibonding electron of NO [34-36]. The support material (γ -Al₂O₃) does not adsorb NO as well. Volumetric adsorption of NO has been widely used to correlate the catalyst activity with the concentration of the active sites or Co and Ni atoms in the MoS₂ phase [37-41]. The

adsorption mode of NO molecules on Mo and Co(Ni) cations is still controversial. Mononitrosyl or dinitrosyl species and different adsorption mechanisms have been proposed with basis on IR spectroscopy, STM, and DFT calculations [34,42]. Thus, it is difficult to calculate the exact concentration of the active sites using NO adsorption. Nevertheless, the concentration of active sites calculated under the assumption of dinitrosyl species formation [38], is the lowest boundary.

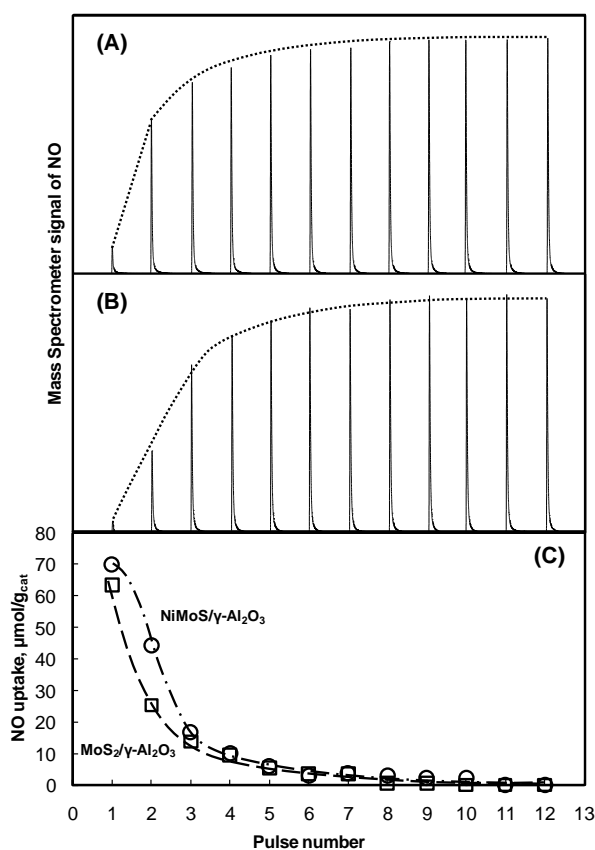


Figure 6. NO pulses during adsorption carried out on $\text{MoS}_2/\gamma\text{-Al}_2\text{O}_3$ (A) and $\text{NiMoS}/\gamma\text{-Al}_2\text{O}_3$ (B) catalyst previously activated at 400°C in 10% H_2S in H_2 . The corresponding NO uptake in $\mu\text{mol}/\text{g}_{\text{cat}}$ (C).

As shown in Fig. 6 (A) and (B), the intensity of the NO peaks increased more rapidly in the case of $\text{MoS}_2/\gamma\text{-Al}_2\text{O}_3$ than in the case of $\text{NiMoS}/\gamma\text{-Al}_2\text{O}_3$, indicating a larger concentration of active sites in the latter material. A slower uptake following an initial rapid one indicated that a subtle rearrangement is needed to accommodate all NO, see Fig. 6 (C). At the steady state further adsorption was not observed after the same number of pulses for both catalysts. The total NO uptake corresponded to $130 \mu\text{mol}/\text{g}_{\text{cat}}$ for the $\text{MoS}_2/\gamma\text{-Al}_2\text{O}_3$ and $160 \mu\text{mol}/\text{g}_{\text{cat}}$ for the $\text{NiMoS}/\gamma\text{-Al}_2\text{O}_3$ sulfide catalyst. Thus, considering the stoichiometry of the dinitrosyl species, the concentration of the active sites is $65 \mu\text{mol}/\text{g}_{\text{cat}}$ for the $\text{MoS}_2/\gamma\text{-Al}_2\text{O}_3$ and $80 \mu\text{mol}/\text{g}_{\text{cat}}$ for the $\text{NiMoS}/\gamma\text{-Al}_2\text{O}_3$. Thus, the addition of 3.6 wt.% of Ni as a metal promoter enhanced the concentration of coordinatively unsaturated cations by about 25%.

4.2. Hydrodenitrogenation of o-propylaniline (OPA)

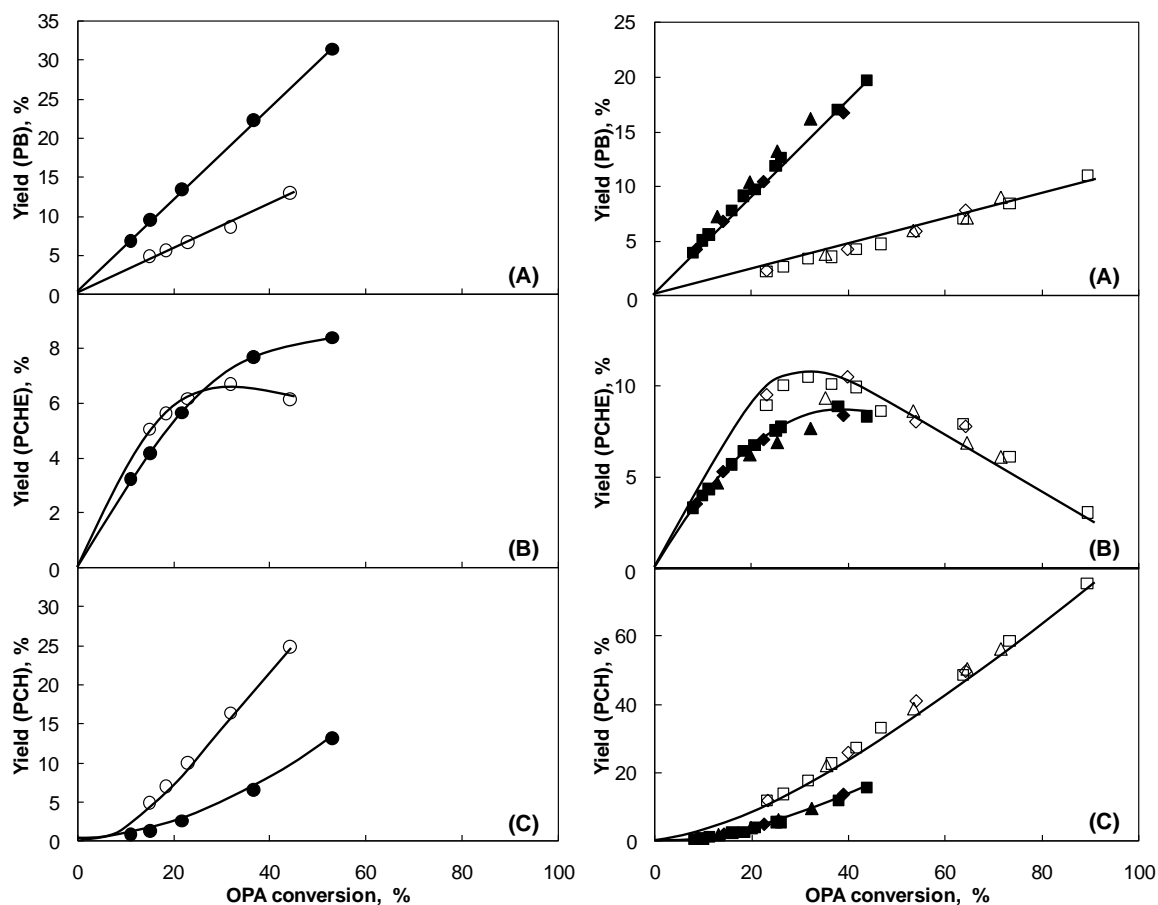


Figure 7. Yield of propylbenzene (A), propylcyclohexene (B), and propylcyclohexane (C) as a function of OPA HDN conversion on MoS₂/γ-Al₂O₃ (●,▲,■,◆) and NiMoS/γ-Al₂O₃ (○,△,□,◇) catalyst. The experiments were carried out in absence (left) and in the presence (right) of DBT. The following symbols are used for different DBT partial pressures: (●,○) 0 kPa, (▲,△) 1.7 kPa, (■,□) 3.4 kPa, and (◆,◇) 5.1 kPa.

The product yields as a function of the OPA conversion are presented in Fig. 7 in the absence and presence of DBT. Nitrogen-free products detected on both catalysts were propylbenzene (PB), propylcyclohexane (PCH), and three isomers of propylcyclohexene (PCHE): 1-propylcyclohexene, 3-propylcyclohexene, and propylidene cyclohexane. The yield of 1-propylcyclohexene was the highest, which is in line with its highest stability, suggesting that the isomers are equilibrated. Thus, for further analysis, all three isomers were lumped together. PB (formed from OPA via direct C(sp²)-N bond cleavage) with around 20% and PCH (formed as a secondary end product) together with PCHE with combined 12% were the main products detected in the absence and presence of DBT on MoS₂/γ-Al₂O₃. The intermediate product of HYD, propylcyclohexylamine (PCHA), was not detected on both catalysts. PCHE was the single intermediate observed.

Two additional reaction pathways were also examined, i.e., the hydrogenation of propylbenzene to propylcyclohexane and the reverse dehydrogenation of propylcyclohexane

to propylbenzene. From the parallel reaction of OPA and ethylbenzene/ethylcyclohexane, it is concluded that hydrogenation and dehydrogenation of aromatic rings without basic nitrogen does not occur under our conditions or are very slow compared with the conversion of substituted propylbenzene. Conversion of ethylbenzene or ethylcyclohexane was not observed over the whole space time range. This is attributed to the strong competitive adsorption of molecules containing an amine functional group [11,43,44].

4.2.1. Kinetic modeling of the HDN OPA network

The HDN reaction was first order in OPA for MoS₂/γ-Al₂O₃ and NiMoS/γ-Al₂O₃ catalysts and all reaction conditions studied. Corresponding concentration-time profiles, as presented in Fig. 8, show a linear correlation with the apparent rate constant as the slope.

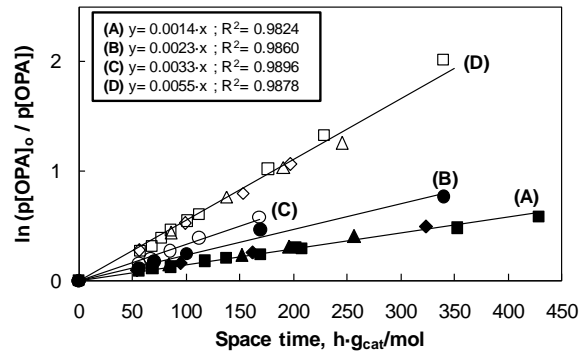


Figure 8. Determination of the apparent rate constants (mol/h·g_{cat}) for the first rate reaction of the o-propylaniline HDN carried out on MoS₂/γ-Al₂O₃ (●,▲,■,◆) and NiMoS/γ-Al₂O₃ (○,△,□,◇) catalyst. The following symbols are used for different DBT partial pressures: (●,○) 0 kPa, (▲,△) 1.7 kPa, (■,□) 3.4 kPa, and (◆,◇) 5.1 kPa. The reactions carried out in the presence of DBT are marked with (A) for MoS₂/γ-Al₂O₃ and (D) for NiMoS/γ-Al₂O₃, and in the absence of DBT are marked with (B) for MoS₂/γ-Al₂O₃ and (C) for NiMoS/γ-Al₂O₃ catalyst.

Considering the proposed reaction network, see Fig. 9, the following differential equations are obtained:

$$\frac{dp[\text{OPA}]}{dt} = -k_1' \cdot p[\text{OPA}] - k_2' \cdot p[\text{OPA}]$$

$$\frac{dp[\text{PB}]}{dt} = k_1' \cdot p[\text{OPA}]$$

$$\frac{dp[\text{PCHE}]}{dt} = k_2' \cdot p[\text{OPA}] - k_3' \cdot p[\text{PCHE}]$$

$$\frac{dp[\text{PCH}]}{dt} = k_3' \cdot p[\text{PCHE}]$$

Note that propylcyclohexene (PCHE) is considered as kinetic primary product, because propylcyclohexylamine (PCHA) was not observed. After data fitting, applying the Runge-Kutta integration method, rate constants were obtained in mol/h·g_{cat} (see Table 2).

Fitting results of the OPA HDN product distribution on MoS₂ and NiMoS/γ-Al₂O₃ catalysts in absence and presence of DBT are presented in Fig. 10.

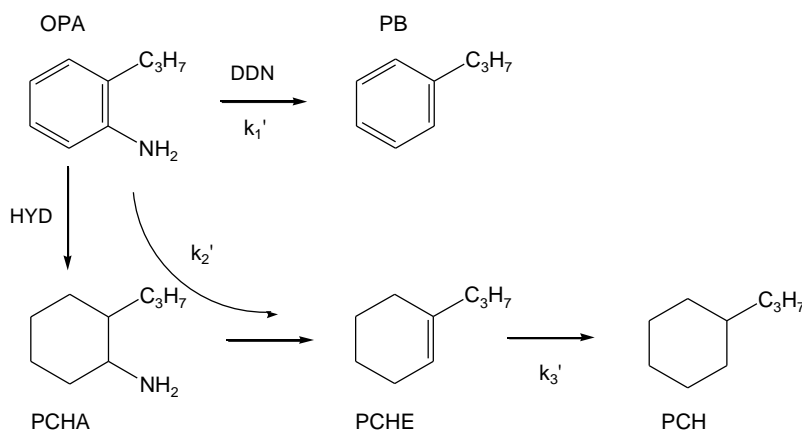


Figure 9. Reaction network of the o-propylaniline (OPA) HDN reaction with differentiation between the direct denitrogenation (DDN) and the hydrogenation (HYD) pathway, where different abbreviations are defined as follows:
 PB – propylbenzene
 PCHA – propylcyclohexylamine
 PCHE – propylcyclohexene
 PCH – propylcyclohexane.

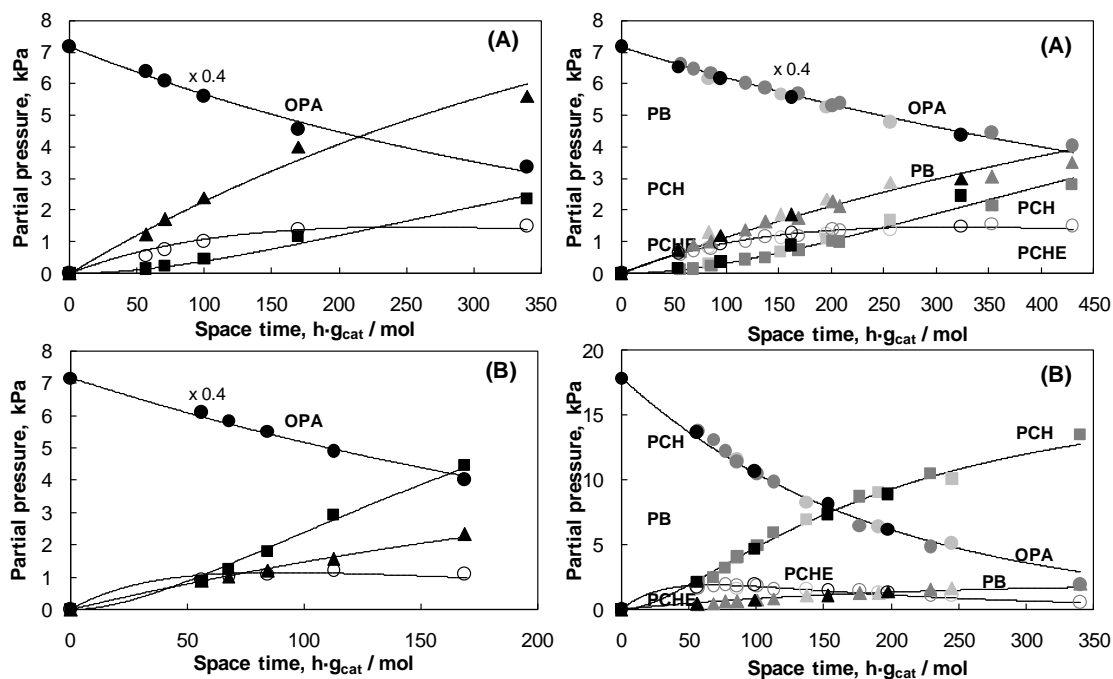


Figure 10. Fitting results of the product distribution in the HDN of o-propylaniline on (A) MoS₂/γ-Al₂O₃ and (B) NiMoS/γ-Al₂O₃ catalyst; ● o-propylaniline (OPA), ■ propylcyclohexane (PCH), ▲ propylbenzene (PB), ○ propylcyclohexene (PCHE). The reactions were carried out in absence (left) and in the presence of DBT (right) with partial pressures of 1.7 (light grey), 3.4 (dark grey) and 5.1 kPa (black color). As shown, the OPA HDN is zero order with respect to DBT. The points present the experimental data and the lines fitted results.

Catalyst	Feed	Rate constants, mol / h·g _{cat}			
		k'	k ₁ '	k ₂ '	k ₃ '
MoS ₂ /γ-Al ₂ O ₃	OPA	0.0023	0.0014	0.0009	0.0062
	OPA + DBT	0.0015	0.0007	0.0008	0.0060
NiMoS/γ-Al ₂ O ₃	OPA	0.0033	0.0010	0.0023	0.0270
	OPA + DBT	0.0053	0.0006	0.0047	0.0312

Table 2. The rate constants (mol/h·g_{cat}) obtained for the OPA HDN at 370 °C, 5 MPa on MoS₂/γ-Al₂O₃ and NiMoS/γ-Al₂O₃ catalysts.

4.2.2. Influence of Ni substitutions on the OPA HDN

HDN conversion of OPA is equal to the total OPA conversion, because the only nitrogen-containing intermediate, PCHA, was not detected in the products. Both in the absence and in the presence of DBT, NiMoS/γ-Al₂O₃ was more active for nitrogen removal than MoS₂/γ-Al₂O₃, Fig. 8. With nickel promotion of MoS₂/γ-Al₂O₃ catalyst, the total apparent rate constant ($k' = k_1' + k_2'$) increased from 2.3 to 3.3 mmol/h·g_{cat} in sulfur free conditions and from 1.5 to 5.3 mmol/h·g_{cat} in the presence of DBT.

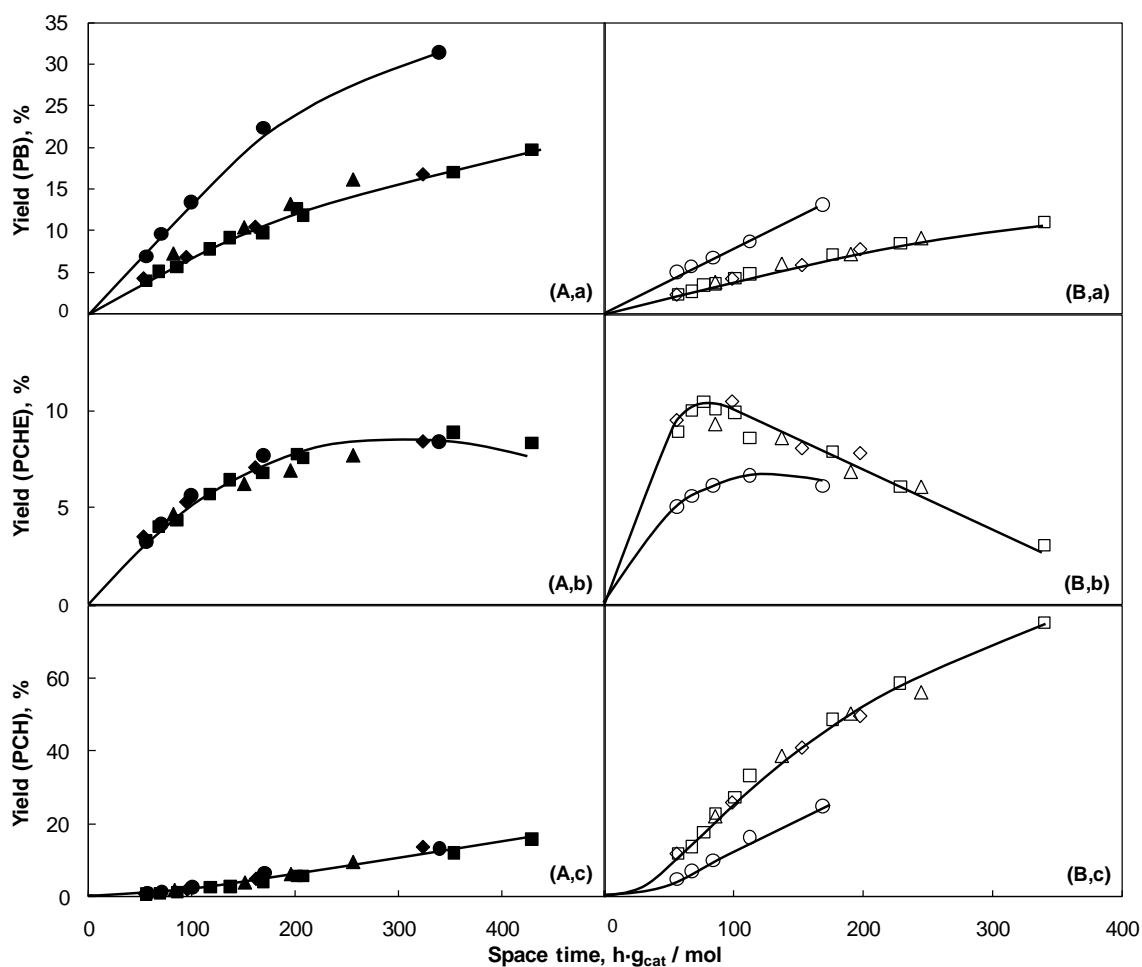


Figure 11. Yield of propylbenzene (a), propylcyclohexene (b), and propylcyclohexane (c) as a function of space time on MoS₂/γ-Al₂O₃ (A) and NiMoS/γ-Al₂O₃ (B) catalyst. Diverse symbols are used for different DBT partial pressures: (●,○) 0 kPa, (▲,△) 1.7 kPa, (■,□) 3.4 kPa, and (◆,◇) 5.1 kPa.

For a detailed analysis of how nickel influences the HDN network, the yield of individual products are presented as a function of space time in Fig. 11 for reactions carried out in absence and in the presence of 1.7, 3.4, and 5.1 kPa DBT. For all conditions studied, the yield of propylbenzene, the product of the DDN route, was higher for the unpromoted MoS_2 catalyst (see Fig. 11 (A,a) and (B,a)). Promotion by Ni cations led to a decrease in the DDN rate by approximately 40% in absence and presence of DBT.

In contrast, the HYD rate was enhanced by Ni promotion, indicated by the higher yield of PCHE and PCH (see Fig. 11 (A,b), (A,c) and (B,b), (B,c)). In absence of DBT, the HYD rate was enhanced 2.5 times, and in the presence of DBT, the rate was approximately five times higher than for $\text{MoS}_2/\gamma\text{-Al}_2\text{O}_3$. As previously noted, the intermediate product of the OPA hydrogenation route (propylcyclohexylamine, PCHA) was not detected; therefore, (PCH + PCHE) to PB ratios are calculated in order to compare HYD to DDN rates. See Tables 3 and 4 for the OPA HDN carried out in the absence and presence of 3.4 kPa DBT, respectively.

Catalyst	Space time, $\text{h}\cdot\text{g}_{\text{cat.}}/\text{mol}$	HDN conversion, %	Yield, %			(PCH+PCHE)/PB
			PB	PCHE	PCH	
$\text{MoS}_2/\gamma\text{-Al}_2\text{O}_3$	56	11.0	6.9	3.2	0.8	0.6
	169	36.6	22.4	7.7	6.5	0.7
$\text{NiMoS}/\gamma\text{-Al}_2\text{O}_3$	56	14.9	5.0	5.1	4.9	2.0
	169	44.1	13.1	6.1	24.9	2.4

Table 3. Yield of the OPA HDN products in the absence of DBT.

Catalyst	Space time, $\text{h}\cdot\text{g}_{\text{cat.}}/\text{mol}$	HDN conversion, %	Yield, %			(PCH+PCHE)/PB
			PB	PCHE	PCH	
$\text{MoS}_2/\gamma\text{-Al}_2\text{O}_3$	56	8.0	4.0	3.3	0.7	1.0
	353	37.9	17.0	8.9	12.0	1.2
$\text{NiMoS}/\gamma\text{-Al}_2\text{O}_3$	56	23.1	2.3	9.0	11.9	9.2
	176	63.8	7.1	7.9	48.7	8.0
	340	89.4	11.0	3.1	75.3	7.1

Table 4. Yield of the OPA HDN products in the presence of 3.4 kPa DBT.

4.2.3. Effect of dibenzothiophene (DBT) on the OPA HDN

The comparison between OPA HDN carried out in the absence and the presence of 1.7, 3.4, and 5.1 kPa DBT is given for $\text{MoS}_2/\gamma\text{-Al}_2\text{O}_3$ and $\text{NiMoS}/\gamma\text{-Al}_2\text{O}_3$ in Fig. 8. DBT reduces the rate of HDN on $\text{MoS}_2/\gamma\text{-Al}_2\text{O}_3$, while it increases the rate on $\text{NiMoS}/\gamma\text{-Al}_2\text{O}_3$. The apparent rate constant decreased from 2.3 to 1.5 $\text{mmol}/\text{h}\cdot\text{g}_{\text{cat}}$ for the former, while it increased from 3.3 to 5.3 $\text{mmol}/\text{h}\cdot\text{g}_{\text{cat}}$ for the latter. As soon as a small amount of DBT was present, the impact on the HDN rate was observed, and there were no further changes with increase in the DBT partial pressure.

To inspect more closely the influence of DBT, the yield of the individual products is displayed as a function of space time in Fig. 11 (A) and (B), for MoS₂/γ-Al₂O₃ and NiMoS/γ-Al₂O₃, respectively. In case of MoS₂/γ-Al₂O₃, the DDN rate was selectively reduced (see Fig. 11 (A,a)). The HYD route remained in contrast unaffected (see Fig. 11 (A,b) and (A,c)). Also with NiMoS/γ-Al₂O₃ the rate of the DDN was reduced by DBT (Fig. 11 (B,a)). Interestingly, the HYD route was promoted, as seen by the increase in the yields of PCHE and PCH (see Fig. 11 (B,b) and (B,c)). Thus, the overall effect of DBT on the OPA HDN rate is negative on the MoS₂/γ-Al₂O₃ catalyst, because of poisoning of the DDN route, while on NiMoS/γ-Al₂O₃, the reduction in the DDN rate is overcompensated by the higher HYD rate. Again, it should be emphasized that under the chosen operating conditions the variation in the concentration of DBT did not affect the rates effect on individual pathways.

The rate of the DDN route on the MoS₂/γ-Al₂O₃ catalyst was reduced by the addition of DBT, indicated by change in the rate constant (k_1') from 1.4 to 0.7 mmol/h·g_{cat}. On NiMoS/γ-Al₂O₃, the rate constant of DDN route (k_1') decreased from 1.0 to 0.6 mmol/h·g_{cat}. Thus, the presence of DBT reduced the DDN reaction route by approximately 50% for both catalysts. Interestingly, increasing concentrations of DBT did not further reduce the rate of DDN. In the presence of DBT, the HYD rate on MoS₂/γ-Al₂O₃ was unaffected, while on NiMoS/γ-Al₂O₃, it doubled (see the PCHE + PCH yields in Tables 3 and 4 for the reaction carried out in the absence and presence of 3.4 kPa DBT).

In addition, the hydrodesulfurization (HDS) of DBT during OPA HDN has been followed to monitor the preferred reaction pathway of sulfur removal. The DBT conversion over unpromoted MoS₂/γ-Al₂O₃ catalyst reached 50% at the highest OPA space time. In Fig. 12, DBT HDS product distribution is presented for both MoS₂/γ-Al₂O₃ (A) and NiMoS/γ-Al₂O₃ (B) catalysts. Biphenyl (BPh), the product of the direct desulfurization (DDS) route, was the main sulfur-free product in both cases, while the partly hydrogenated product, phenylcyclohexane (PhCH) is minority product. With increasing DBT conversion, the yield of PhCH increased linearly up to 7% and 15% on the Mo and NiMo catalyst, respectively. Note that the DBT conversion range is very different for the two catalysts. However, the low concentration of PhCH and the absence of the fully hydrogenated HDS product bicyclohexyl on both catalysts suggest that the hydrogenation route of DBT is severely hindered by the presence of nitrogen-containing compounds.

Transient experiments with DBT were performed to better understand the impact of DBT on the OPA HDN, especially on the HYD route. The NiMoS/γ-Al₂O₃ catalyst was first stabilized for 16 h in pure OPA feed after which 3.4 kPa of DBT was cofed into the reactor for 6 h. Finally, DBT was removed. The OPA HDN conversion as a function of time on stream is

shown in Fig. 13, and comparison was made with the reaction carried out from the beginning in the presence of 3.4 kPa of DBT.

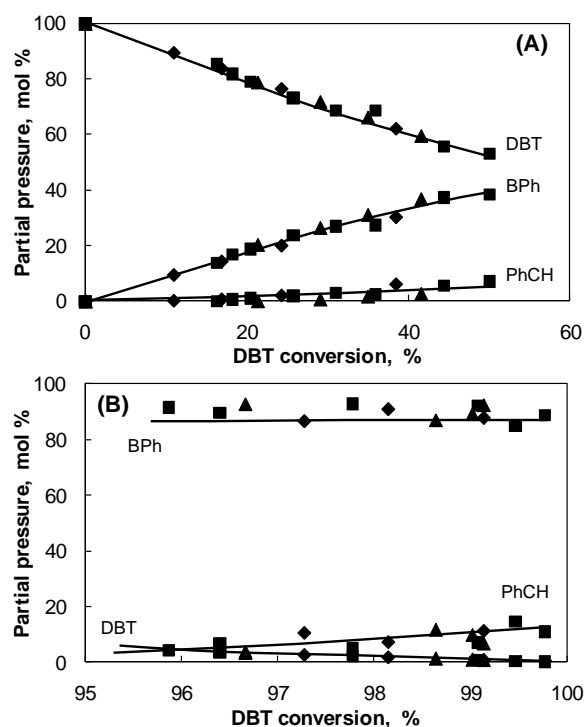


Figure 12. The product distribution in HDS of dibenzothiophene (DBT) during HDN of *o*-propylaniline on $\text{MoS}_2/\gamma\text{-Al}_2\text{O}_3$ (A) and $\text{NiMoS}/\gamma\text{-Al}_2\text{O}_3$ (B) catalyst. The following symbols are used for different DBT partial pressures: (▲) 1.7 kPa, (■) 3.4 kPa, and (◆) 5.1 kPa.

Stronger catalyst deactivation is observed, when the reaction is carried out in the absence of DBT. Further, it is confirmed that the OPA HDN conversion on NiMoS catalyst is higher in the presence (36.7%) than in absence of DBT (27.4%). After cofeeding DBT, at first, the OPA HDN conversion dropped (23.7%) and then slowly increased reaching slightly higher value (30.5%) than the value obtained after the first 16 h (27.4%). Nevertheless, the conversion never reached the value obtained when the reaction was run from the beginning in the presence of DBT. After removing DBT from the feed, the conversion swiftly increased (48.5%) and then gained a declining trend.

Attention must be put on the yield of individual products to analyze the complex behavior in detail, see Fig. 14. The PB yield, as the only product of the DDN route, was higher in the absence (6.9%) than in the presence of DBT (3.5%). After cofeeding DBT, the PB yield dropped to the same level like when the reaction was run from the beginning in the presence of DBT. Removing DBT from the feed brought back the yield level to the previous value. The yield of PCHE, the only intermediate of the HYD route, was lower in absence (7.0%) than in the presence of DBT (9.7%). After cofeeding DBT, the PCHE yield increased to the same level as if the reaction was run from the beginning in the presence of DBT. Final removal of

DBT from the feed depressed the yield again to the previous level. The yield of PCH, as the main end product from the HYD route, exhibited the same trend as the OPA HDN conversion, i.e., a negative effect caused by DBT co-feeding, followed by a positive yield recovery and finally followed by very positive effect once DBT was removed from the feed.

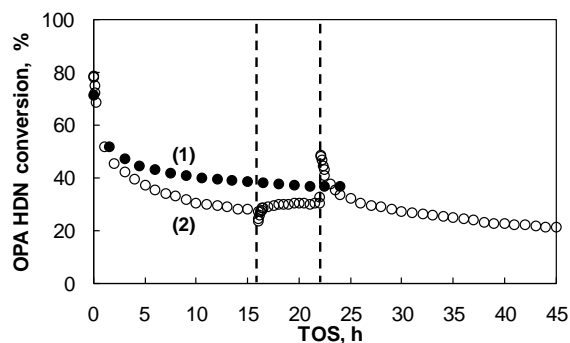


Figure 13. OPA HDN conversion as a function of time on stream for the reaction carried out on NiMoS/ γ -Al₂O₃ catalyst. Steady state was reached after 16 h TOS in the: (1) presence of 3.4 kPa DBT and (2) absence of DBT. Experiment (2) was performed as a transient; 3.4 kPa DBT was co-fed for 6 h after steady state was reached.

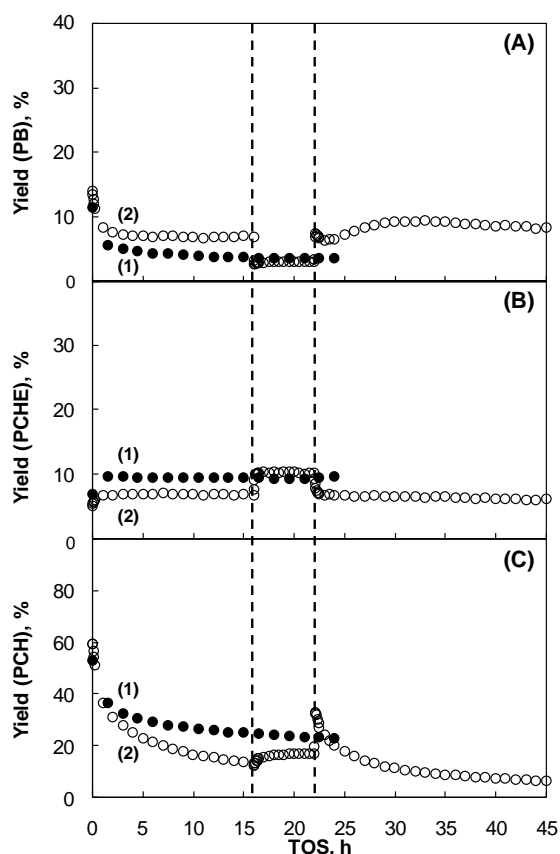


Figure 14. Yield of propylbenzene (A), propylcyclohexene (B), and propylcyclohexane (C) as a function of time on stream for the reaction carried out on NiMoS/ γ -Al₂O₃ catalyst. Steady state was reached after 16 h TOS in the: (1) presence of 3.4 kPa DBT and (2) absence of DBT. Experiment (2) was performed as a transient; 3.4 kPa DBT was co-fed for 6 h after steady state was reached.

4.2.4. Stability of the NiMoS/ γ -Al₂O₃ catalyst in the OPA HDN

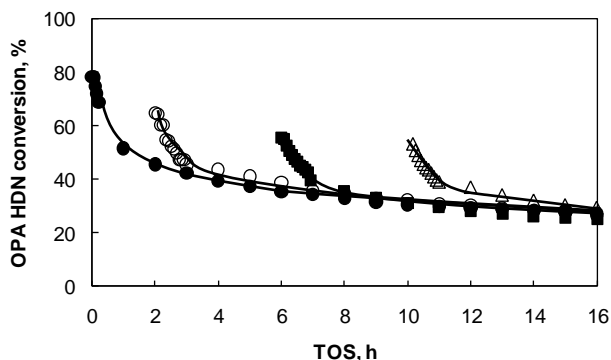


Figure 15. OPA HDN conversion as a function of time on stream for the reaction carried out on NiMoS/ γ -Al₂O₃ catalyst in the absence of DBT. The following symbols are used for different catalyst pretreatment: (●) 8-h sulfidation in 10% H₂S in H₂ (400 °C, 1.8 MPa), (○) 8-h sulfidation in 10% H₂S in H₂ (400 °C, 1.8 MPa) followed by 2-h reduction in H₂ (370 °C, 5 MPa), (■) 8-h sulfidation in 10% H₂S in H₂ (400 °C, 1.8 MPa) followed by 6-h reduction in H₂ (370 °C, 5 MPa), and (Δ) 8-h sulfidation in 10% H₂S in H₂ (400 °C, 1.8 MPa) followed by 10-h reduction in H₂ (370 °C, 5 MPa).

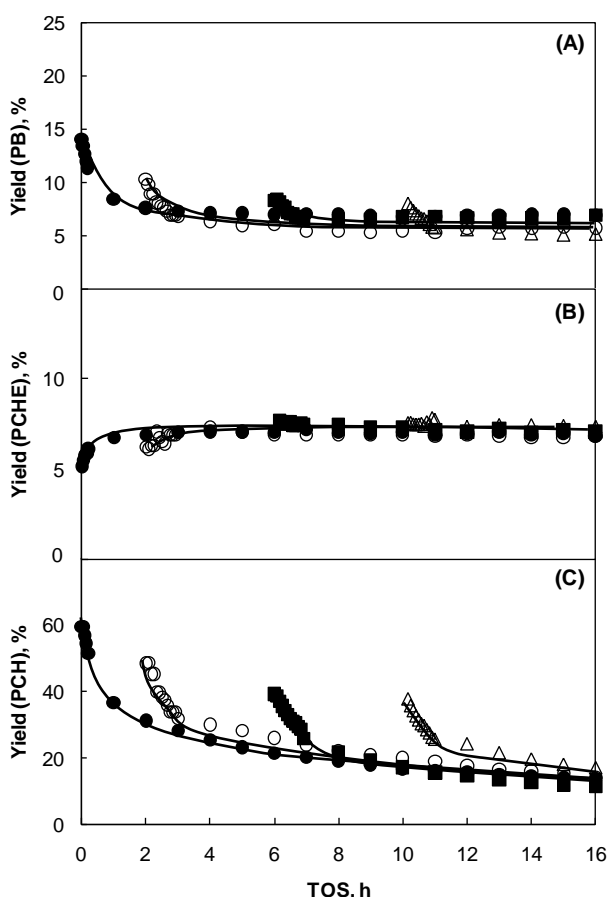


Figure 16. Yield of propylbenzene (A), propylcyclohexene (B), and propylcyclohexane (C) as a function of time on stream for the reaction carried out on NiMoS/ γ -Al₂O₃ catalyst in the absence of DBT. The following symbols are used for different catalyst pretreatment: (●) 8-h sulfidation in 10% H₂S in H₂ (400 °C, 1.8 MPa), (○) 8-h sulfidation in 10% H₂S in H₂ (400 °C, 1.8 MPa) followed by 2-h reduction in H₂ (370 °C, 5 MPa), (■) 8-h sulfidation in 10% H₂S in H₂ (400 °C, 1.8 MPa) followed by 6-h reduction in H₂ (370 °C, 5 MPa), and (Δ) 8-h sulfidation in 10% H₂S in H₂ (400 °C, 1.8 MPa) followed by 10-h reduction in H₂ (370 °C, 5 MPa).

Different hydrogen treatments were applied before HDN reactions to better understand the initial activity and deactivation on the NiMoS/ γ -Al₂O₃ catalyst (in the absence of DBT). The highest initial OPA HDN conversion (78.5%) was observed when the catalyst was activated only by sulfidation (8 h at 400 °C in 1.8 MPa of 10% H₂S in H₂), Fig. 15. The initial conversion dropped when the catalyst sulfidation was followed by reduction at 370 °C in 5 MPa of H₂ for 2 h (65.0%), 6 h (55.5%), and it stayed almost constant after 10-h reduction (53.3%).

The product distribution as a function of the catalyst pretreatment is given in Fig. 16. The highest initial yield of PB and PCH was observed when the catalyst was only sulfided, 14.0% and 59.4%. When the reduction followed the activation, the PB and PCH yield decreased to 10.3% and 48.4% (2-h reduction), 8.3% and 39.3% (6-h reduction), and 8.0% and 37.7% (10-h reduction), respectively. The initial yield of PCHE increased from 5.1% (after catalyst sulfidation) to 6.2% (2-h reduction) reaching the final value of 8.1% (10-h reduction).

4.2.5. Temperature dependence of the catalytic reaction

The OPA HDN conversion for unpromoted MoS₂/ γ -Al₂O₃ and promoted NiMoS/ γ -Al₂O₃ catalysts as a function of reaction temperature is shown in Fig. 17, for the experiments performed in the presence and absence of DBT. For the studied temperature range (330 to 390 °C), in the presence of DBT, the OPA HDN conversion increased from 5.5 to 18.9% and from 18.9 to 55.9%, while in the absence of DBT, increased from 6.5 to 27.5% and from 17.5 to 41.9% for MoS₂/ γ -Al₂O₃ and NiMoS/ γ -Al₂O₃ catalyst, respectively.

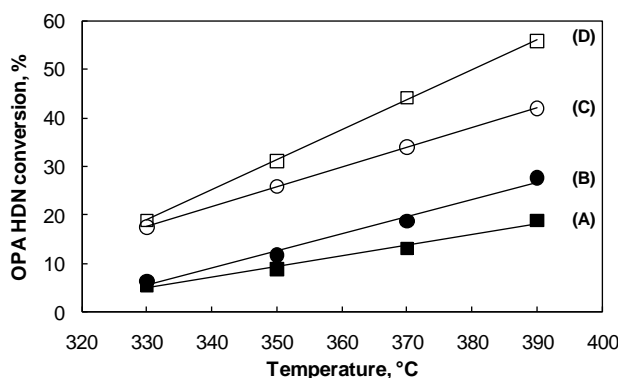


Figure 17. The o-propylaniline HDN conversion as a function of reaction temperature at the space time of 82 h·g_{cat}/mol and total pressure of 5 MPa. The reactions carried out in the presence of 3.4 kPa DBT are marked with (A) for MoS₂/ γ -Al₂O₃ and (D) for NiMoS/ γ -Al₂O₃, and in the absence of DBT are marked with (B) for MoS₂/ γ -Al₂O₃ and (C) for NiMoS/ γ -Al₂O₃ catalyst.

To look more closely how the temperature influences the two parallel reaction routes, the yield of DDN (equal to PB yield) and HYD route products (equal to sum of PCHE and PCH yields) is shown in Fig 18 (A) and (B), respectively. On both, MoS₂/ γ -Al₂O₃ and

NiMoS/ γ -Al₂O₃ catalyst, poisoning of DDN route by DBT was more intense at higher temperature. The yield of HYD products on MoS₂/ γ -Al₂O₃ catalyst was not affected by DBT over the whole range of temperature. On the contrary, on NiMoS/ γ -Al₂O₃ catalyst, increase in yield was more pronounced at the higher temperatures. It is important to note that in the case of the OPA HDN reaction carried out in the absence of DBT on NiMoS/ γ -Al₂O₃ catalyst, at 390 °C, certain activity decrease in the HYD route is observed.

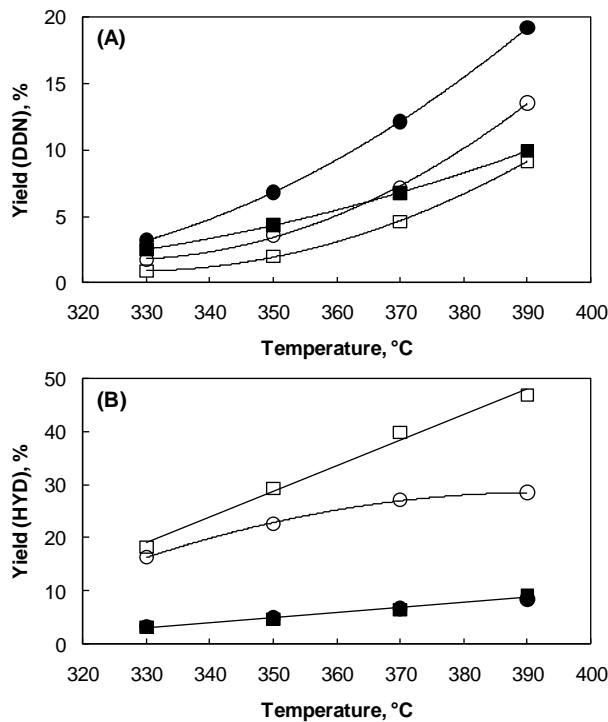


Figure 18. Products yield of the two parallel reaction pathways: (A) direct denitrogenation and (B) hydrogenation as a function of temperature on MoS₂/ γ -Al₂O₃ (●,■) and NiMoS/ γ -Al₂O₃ (○,□) catalyst and at the space time of 82 h·g_{cat}/mol and total pressure of 5 MPa. The following symbols are used for different DBT partial pressures: (●,○) 0 kPa, and (■,□) 3.4 kPa.

The apparent activation energy for both catalysts was obtained from the Arrhenius equation using the semilogarithmic plot $\ln k'$ vs. $1/T$ plot, shown in Figs. 19 and 20, for the experiments performed in the presence and absence of DBT, respectively. In addition, the apparent activation energies for the two parallel routes were calculated based on the rate constants k'_1 for DDN and k'_2 HYD pathway. The corresponding rate constants were calculated (see Table 5) according to the first-order kinetics following the equations:

$$k' = \frac{1}{t} \cdot \ln \frac{P[\text{OPA}]_0}{P[\text{OPA}]}$$

$$k' = k'_1 + k'_2$$

$$k'_1 = \frac{P[\text{PB}] \cdot k'}{P[\text{OPA}]_0 \cdot [1 - e^{-k' \cdot t}]}$$

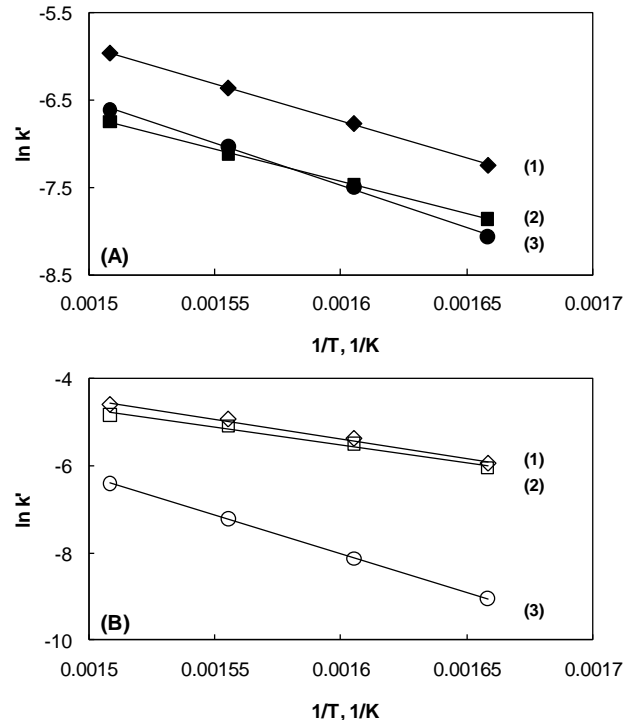


Figure 19. The Arrhenius plot of the first order apparent rate constants for the OPA HDN reaction, carried out in the presence of 3.4 kPa DBT on MoS₂/γ-Al₂O₃ (A) and NiMoS/γ-Al₂O₃ (B) catalyst and at the space time of 82 h·g_{cat}/mol and total pressure of 5 MPa. The values are used for determination of the total apparent activation energy (1), and apparent activation energies for the two parallel routes: HYD (2) and DDN (3).

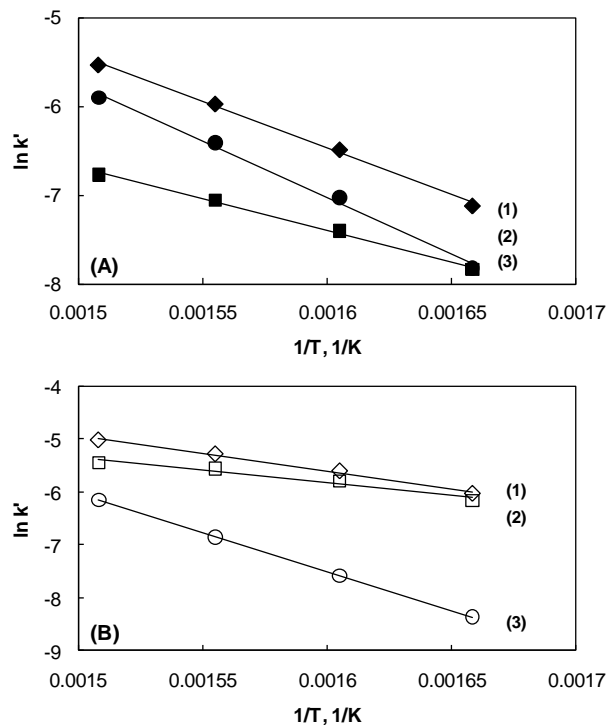


Figure 20. The Arrhenius plot of the first order apparent rate constants for the OPA HDN reaction, carried out in absence of DBT on MoS₂/γ-Al₂O₃ (A) and NiMoS/γ-Al₂O₃ (B) catalyst. The values are used for determination of the total apparent activation energy (1), and apparent activation energies for the two parallel routes: HYD (2) and DDN (3).

The values obtained for the apparent activation energy are listed in Table 6 for all conditions studied. In the presence of DBT, apparent activation energies of OPA HDN did not differ for the two catalysts, MoS₂/γ-Al₂O₃ (71 ± 1.8 kJ/mol) and NiMoS/γ-Al₂O₃ (75 ± 1.9 kJ/mol). In the absence of DBT, the apparent activation energy for MoS₂/γ-Al₂O₃ catalyst increased to 88 ± 2.2 kJ/mol. On the contrary, for NiMoS/γ-Al₂O₃ catalyst, it decreased to 56 ± 1.4 kJ/mol.

Feed	Catalyst	Temperature, °C	Rate constants, mol / h·g _{cat}		
			k'	k' ₁	k' ₂
OPA + DBT	MoS ₂ /γ-Al ₂ O ₃	330	0.0007	0.0003	0.0004
		350	0.0012	0.0006	0.0006
		370	0.0015	0.0007	0.0008
		390	0.0026	0.0013	0.0013
	NiMoS/γ-Al ₂ O ₃	330	0.0026	0.0001	0.0023
		350	0.0046	0.0003	0.0043
		370	0.0071	0.0007	0.0064
		390	0.0100	0.0016	0.0084
OPA	MoS ₂ /γ-Al ₂ O ₃	330	0.0008	0.0004	0.0004
		350	0.0015	0.0009	0.0006
		370	0.0023	0.0014	0.0009
		390	0.0039	0.0027	0.0012
	NiMoS/γ-Al ₂ O ₃	330	0.0024	0.0002	0.0022
		350	0.0037	0.0005	0.0032
		370	0.0051	0.0011	0.0040
		390	0.0066	0.0021	0.0045

Table 5. The rate constants (mol/h·g_{cat}) obtained for the OPA HDN at the space time t= 82 h·g_{cat}/mol, p=5 MPa on MoS₂ and NiMoS/γ-Al₂O₃ catalysts.

Feed	Catalyst	Apparent activation energy, kJ / mol		
		E _a	E _a (DDN)	E _a (HYD)
OPA + DBT	MoS ₂ /γ-Al ₂ O ₃	71 ± 1.8	81 ± 2.0	61 ± 1.5
	NiMoS/γ-Al ₂ O ₃	75 ± 1.9	147 ± 3.7	68 ± 1.7
OPA	MoS ₂ /γ-Al ₂ O ₃	88 ± 2.2	106 ± 2.7	59 ± 1.5
	NiMoS/γ-Al ₂ O ₃	56 ± 1.4	123 ± 3.0	40 ± 1.0

Table 6. The apparent activation energy (kJ/mol) obtained for the OPA HDN, in the absence and presence of 3.4 kPa DBT on MoS₂ and NiMoS/γ-Al₂O₃ catalysts.

5. Discussion

The oxide catalyst precursors compared in this study have a Mo concentration of 2.5 Mo atoms/nm², which is below the monolayer concentration of approximately 4.6-5 atoms/nm² given for the γ-Al₂O₃ support [28,45]. XRD patterns of the oxide precursors do not exhibit reflections of Mo crystalline species, and the Raman spectra imply the existence of the polymolybdate species, see Figs. 1 and 3 (A) [46,47]. Neither the presence of isolated MoO₄ tetrahedra nor crystalline MoO₃ was observed, due to the absence of the characteristic Raman bands at 896, 846, and 318 cm⁻¹ and 996, 821, 667, and 377 cm⁻¹,

respectively [48]. Thus, the oxidic precursors are polymolybdates, well dispersed on the γ -Al₂O₃ support. Sulfided catalysts, as shown in Raman spectra of Fig. 3 (B), revealed the presence of the typical MoS₂ phase. In line with the characteristics of the oxide Mo species, the sulfide phase also exhibited high dispersion. XRD indicated low MoS₂ stacking degree with the absence of the diffraction peak at 14° 2 θ , Fig. 1. TEM micrographs confirmed the high dispersion of the sulfided slabs with average MoS₂ stacking degree of two and slabs length below 10 nm on the γ -Al₂O₃ support, see Fig. 2. Furthermore, the formation of Ni sulfides was not observed (XRD and TEM).

The concentration of the accessible metal cations was 65 and 80 $\mu\text{mol/g}_{\text{cat}}$ for MoS₂/ γ -Al₂O₃ and NiMoS/ γ -Al₂O₃, indicating that the presence of Ni cations enhanced their concentration by approximately 25%. This is in line with the higher tendency of the lower valent cations in mixed sulfides to be accessible. It is interesting to note that this increase is considerably lower than the concentration of Ni added, suggesting the absence of NO specificity to exposed cations. We assume, therefore, for the following discussions that Ni incorporates only at the edges of the MoS₂ slabs, and the cations are exposed randomly.

Both materials showed a well-known profile with three sections during the reductive conversion (H₂S in H₂ mixture) from the supported oxide precursor to the final sulfide material. In the initial sulfiding section, low temperature sulfiding, oxygen is substituted by sulfur as seen in the marked consumption of H₂S followed by parallel H₂O production (not shown). H₂ is not consumed in this section (not shown). As previously published, the first Mo-S bond formation is leading to the conversion of oxides to different oxy-sulfidic species [33,49]. Cattaneo et al. published that the terminal Mo=O bonds, characteristic for the molybdenum monolayer species, are the first one to react forming Mo=S bonds [50]. XPS studies showed that at the low temperatures molybdenum reduces from Mo⁶⁺ to Mo⁵⁺ by oxidation of S²⁻ to bridging S₂²⁻ [51,52]. Further conversion above 150 °C shows that the sulfidation process is reversed, and for a short temperature interval, H₂S is released. The maximum of H₂S evolution between 205 and 225 °C is coupled with a maximum in H₂ consumption (not shown) indicating molybdenum reduction to Mo⁴⁺. This reduction maximum is shifted from 225 °C for MoS₂/ γ -Al₂O₃ to 205 °C in the presence of Ni cations. This indicates that incorporated Ni cations facilitate H₂ dissociation and so the overall catalyst reducibility. The subsequent consumption of H₂S, again followed by H₂O production, is concluded to be a high temperature sulfiding, related to full conversion of the precursor materials to the corresponding MoS₂ and NiMoS particles.

Under all reaction conditions and with all catalysts studied, the HDN of OPA follows two reaction pathways, which are summarized in Fig. 9. One involves the cleavage of the

aromatic C(sp²)-N bond and is assigned as the DDN, while the other involves the hydrogenation of the aromatic ring followed by nitrogen removal in form of NH₃ or substitution with an -SH group. That latter nitrogen removal is concluded to be so fast after the aromatic ring is hydrogenated that the intermediate propylcyclohexylamine has not been detected in the present experiments. In agreement with the literature, we conclude that the rate of the phenyl ring hydrogenation is limiting, while that of nitrogen removal is comparably large [53].

A question that must be addressed at this point is whether the nitrogen removal from the PCHA proceeds via Hofmann elimination or via nucleophilic substitution of NH₂ by an -SH group, followed by further C-S bond hydrogenolysis. The Hofmann-type elimination has been considered to be the main mechanism for nitrogen removal in the HDN of, e.g., cyclohexylamine and aniline-type compounds [54-57], when the reactions are carried out at the high temperature (350-370 °C) and pressure (3-5 MPa) and with H₂S partial pressure up to 17.5 kPa.

The other explanation, the S_N2 substitution of the NH₂ group with an -SH group has been as well published [58,59]. For the first time, the thiol-type intermediates were obtained in the HDN reactions of n-hexylamines [60-63] carried out at the relatively low temperatures (270-320 °C) and pressure (3 MPa) and with high H₂S partial pressure (10-100 kPa). It was concluded that the selectivity to hexenes increases with lower and to thiols with higher H₂S partial pressure. Because of the relatively high reaction temperature and pressure (370 °C, 5 MPa) and the fact that the thiol-type compound was not identified (the carbon balance was fully closed under all reaction conditions), we can propose that the nitrogen removal after hydrogenation of the phenyl ring is governed by a Hofmann-type elimination of the aliphatic C(sp³)-N bond.

Under the current reaction conditions, the products from the two pathways, DDN and HYD, are not interconnected, as Fig. 7 (A) and (B) show a perfectly linear correlation to the overall conversion. This indicates that hydrogenation or dehydrogenation rates of the hydrocarbon products must be at least two orders of magnitude slower than the other reactions involved in the network. Because the reactions are first order in all reacting substrates, the question arises, whether this is a direct consequence of a slow true rate constant for the hydrogenation or of a very low adsorption constant. While we were unable to directly determine the adsorption constant, the high rate of the hydrogenation of the aromatic ring of o-propylaniline indicates that the low rate of hydrogenation of propylbenzene is related to a very low adsorption constant.

Intuitively, one would assume that the direct denitrogenation must be related to the presence of CUS, Lewis acid sites at the perimeter of the MoS₂ slabs. If this holds true, a higher concentration of such coordinatively unsaturated sites should enhance the rate of the DDN reaction. For the materials studied, that concentration of accessible Lewis acid sites was 25% higher for NiMoS/γ-Al₂O₃ than for MoS₂/γ-Al₂O₃.

Despite this higher concentration of coordinatively unsaturated sites on NiMoS/γ-Al₂O₃, the rate of DDN decreased drastically, in agreement with an earlier observation [64]. It is surprising that this decrease appears to be directly related to the relative concentration of accessible Mo cations at the perimeter of the MoS₂ slabs. Both samples, MoS₂/γ-Al₂O₃ and NiMoS/γ-Al₂O₃, contain identical concentration of Mo (895 μmol/g_{cat}). The additional concentration of Ni added is 610 μmol/g_{cat} leading to a mol fraction of 0.4 for Ni. The rate of DDN decreased with NiMoS/γ-Al₂O₃ to 60% of the value observed with MoS₂/γ-Al₂O₃. In parallel, the apparent energy of activation for the DDN route (in the presence of DBT) with NiMoS/γ-Al₂O₃ was almost twice higher than the one observed with MoS₂/γ-Al₂O₃ catalyst. It would be a remarkable coincidence, if the relative decrease in rate would be fortuitously identical to the nominal decrease in the average concentration of Mo available cations. Thus, we conclude that only Mo cations are associated with the active sites of the DDN pathway, i.e., that Ni cations are inactive. Note that we were not able to directly assess the relative concentration of Ni among the accessible cations. It should be emphasized, however, that the increase in the apparent activation energy indicates a slightly higher adsorption enthalpy for NiMoS/γ-Al₂O₃ catalyst.

It is also remarkable that this relative reduction induced by the presence of Ni (to 60%) also holds for the experiments in the presence of DBT, although the overall rate along that pathway decreased by about 50% in the presence of DBT. This decrease is attributed to the competitive adsorption of OPA and DBT on the accessible Lewis acid sites. Thus, all experimental evidence is in line with the conclusion that only accessible Mo cations participate in the DDN.

While the DDN of OPA is concluded to only occur on Mo cations, the analogous reaction of DBT desulfurization is not restricted. On MoS₂/γ-Al₂O₃ and NiMoS/γ-Al₂O₃, the dominating reaction pathway was the DDS leading to biphenyl as dominating product. The much higher rate of HDS with NiMoS/γ-Al₂O₃ than with MoS₂/γ-Al₂O₃ catalyst suggests that not only the concentration of CUS has increased but also the intrinsic rate constant of that reaction.

It has been established earlier that the sulfur vacancies as electron withdrawing sites are responsible for the DDS of DBT. Given that the DDS route requires DBT adsorption via sulfur σ-bonding, an analogous sorption mode of OPA is proposed, i.e., adsorption via

σ -bonding of the amine nitrogen on the sulfur vacancy. DFT calculations for the sulfur edge also suggest that such vacancies are crucial for the sulfur removal. Besenbacher et al. [12] found that the C-S scission reaction has lower barriers at the S-edge than on the opposite Mo-edge. Consequently, it is suggested that the sites responsible for the DDN route in OPA HDN are sulfur vacancies at the S-edge of the MoS₂ cluster with preferred adsorption via σ -bonding, Fig. 21 (C) and lead to an overall mechanism via this route as proposed in Fig. 22.

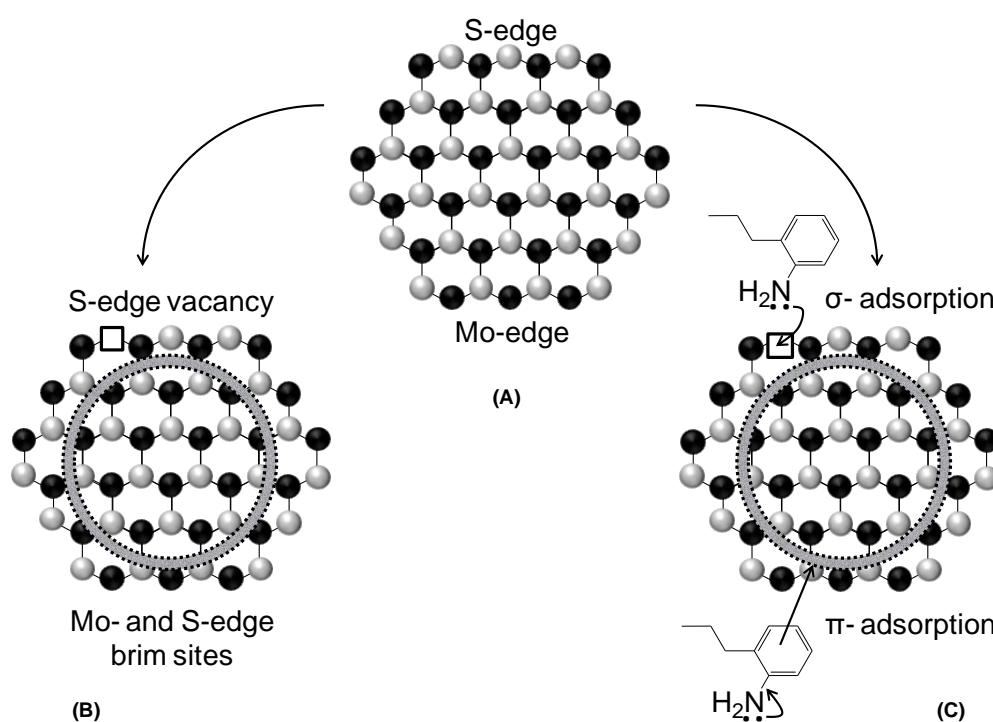


Figure 21. Schematic presentation of MoS₂ structure: (A) differentiation between Mo- and S-edge; (B) different active sites: S-edge vacancies and Mo- and S-edge brim sites; (C) preferred adsorption modes of o-propylaniline depending on the available active sites; where Mo atoms are black and S atoms grey colored.

Let us now turn to the second pathway, the reaction route relying on the hydrogenation of the aromatic ring. If accessible metal cations would be part of the active site, one would expect an increase in the rate proportional to the 25% increase in the concentration of CUS for NiMoS/ γ -Al₂O₃ compared with MoS₂/ γ -Al₂O₃. Therefore, the increase in the HYD rate (2.5 times when the reaction was carried out in absence of DBT) is twice as high as the rate that would be expected on the basis of the formation of new CUS sites for o-propylaniline adsorption. Thus, the higher HYD rate is attributed to an increase in the activity of the existing CUS sites or to a second more active site for hydrogenation. As the HYD rate is the first order in H₂ [65] and in OPA, the difference in the HYD rate can be caused by higher concentrations of adsorbed hydrogen and OPA or a higher intrinsic rate constant.

Many of speculations and suggestions have been put forward for this pathway. In essence, it is suggested that OPA adsorbs via the nitrogen atom of the amine group coordinating to a CUS site with the phenyl ring bends toward the electron-rich zone at the edge of the MoS₂ slab ("brim site") showing a metal-like character [66-68]. DFT calculations imply that this edge acts as sites for the dissociative adsorption of hydrogen. Addition of Ni to the MoS₂/γ-Al₂O₃ catalyst increases the electron density of the brim sites [13,69], which would enhance the hydrogen dissociation on the catalyst surface needed for saturation of phenyl ring in OPA.

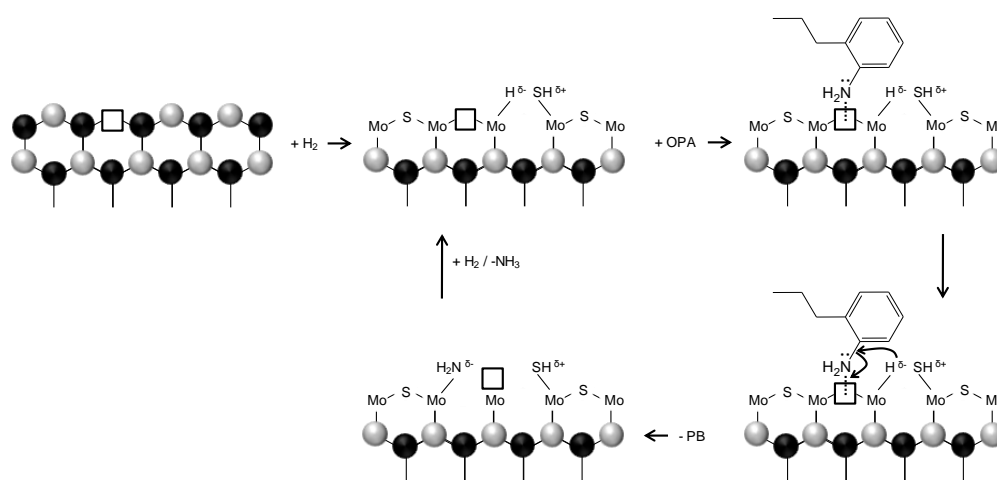


Figure 22. Proposed mechanism of the o-propylaniline direct denitrogenation (DDN) on the S-edge of MoS₂ surface in the sulfur free conditions; where Mo atoms are black and S atoms grey colored.

Having established that the presence of Ni in the MoS₂ layer induces a significantly higher rate in HYD of OPA by enhancing the electron density at the outer part of the basal plane of the sulfide slab, let us use the competitive HDS of DBT to better understand the nature and location of the sites for the HYD route for MoS₂/γ-Al₂O₃ and NiMoS/γ-Al₂O₃.

DBT induced neither promotion nor inhibition of the hydrogenation rate in the OPA HDN on MoS₂/γ-Al₂O₃ catalyst. As the presence of DBT must cause a reduction in the availability of the CUS sites at the rim by the adsorption of either DBT or H₂S, we conclude from the invariance of the rates that the sites for the hydrogenation and, hence, for the adsorption must be different from the CUS sites at the edge of the MoS₂ slab. In consequence, and in the absence of a fortuitous compensation, the equal rate allows us to conclude that the sites at the rim of MoS₂ are hardly involved in the HYD of OPA. This is in stark contrast to the suggestion of Sun et al. [66], indicating that the amine nitrogen does not interact with the accessible metal cations and would indicate also that the actual NH₃ elimination occurs on the brim sites. If OPA adsorbs on the brim zone, it would suggest that the interaction with the aromatic ring and the propyl group must outweigh the direct bonding of the amine nitrogen to

Mo or Ni cations. The elimination of ammonia is concluded to occur via Hofmann-type elimination catalyzed by weak Brønsted acid sites available on the edge of the MoS₂ slabs in the presence of hydrogen. With respect to the reaction temperature, this proposal is well in line with the ammonia elimination from larger aliphatic amines observed during amine synthesis on zeolites [70].

DBT enhanced the HYD rate by a factor of five on NiMoS/γ-Al₂O₃. The positive influence was observed already at the lowest DBT partial pressure but increase in the DBT partial pressure did not further affect the HYD rate. On the level of individual products, only PCH is affected by the long-term deactivation, Fig. 14 (C). Surprisingly, PB and PCHE were quite stable over the TOS, Fig. 14 (A) and (B). Besides the competitive adsorption of DBT and OPA on the sites responsible for the DDN route, competition was observed as well on the sites responsible for the HYD route. After the DBT removal, the yield of PCH drastically increased, Fig. 14 (C). Generally, the presence of DBT retarded the catalyst deactivation caused partially by reduction, as suggested by the results obtained after different hydrogen pretreatments, Figs. 15 and 16. The initial OPA HDN conversion, observed when the catalyst sulfidation was followed by reduction, 65.0% after 2-h reduction, 55.5% after 6-h reduction, and 53.3% after 10-h reduction, was higher than the OPA HDN conversion at the corresponding TOS, observed when the catalyst was only sulfided, 45.0% after 2 h TOS, 35.0% after 6 h TOS, and 31.4% after 10 h TOS. Besides the catalyst deactivation by reduction, there is the second effect that induces very fast initial deactivation, 20% in all conditions studied, that occurs within the first hour after which the common activity level is reached, Fig. 15. The decrease in activity is attributed to the formation of coke from OPA as suggested by the Raman characterization and elemental analysis of the used catalyst. This is supported by the well-known fact that N-containing basic compounds are good coke precursors [71]. Furthermore, the polymerization of the reactant during the HDN process is well documented, and the structure of some dimers and trimers has been solved [72,73]. The rapid decrease in activity is also in line with the quick buildup of coke as soon as the reactant is introduced, as reported in [74]. The hindering of coke formation in the presence of DBT is assigned to the competitive adsorption of DBT or BPh, which decreases the concentration of OPA in the surface and thus decreases the presence of polymers. Moreover, the higher impact on the hydrogenation pathway implies that the formation of coke is favored on hydrogenation sites.

The promotion of the HYD route by the sulfur-containing compound is in contrast to the work previously published where the hydrogenation of OPA and 2,6-dimethylaniline was inhibited by the presence of H₂S [53,75]. However, one must notice that in those studies, H₂S was directly introduced in the feed or generated from dimethyldisulfide, while in the present

study, the effect of DBT is followed. The conversion of DBT, which was very selective to BPh (Fig. 12), leads to a high concentration of H_2S in the system; thus, one might anticipate the same effect. However, as it is seen from our results, it is certainly not true, and thus, the effect of sulfur compounds in the feed is more complex than expected. The difference can be attributed to the mechanisms of interaction between the different sulfur-containing compounds and the catalyst surface. Both DBT and H_2S adsorb on CUS via σ -bonding of the sulfur atom. When H_2S is adsorbed, one can only imagine the creation of -SH groups, which increases the acidity of the surface. In contrast, the direct desulfurization of DBT leads to BPh desorption and S^{2-} ions instead of CUS. Moreover, DBT and BPh, as polyfunctional Lewis bases, can also donate π -electrons from the aromatic rings. Hence, DBT and the products of the HDS process modify the electronic environment in the vicinity of CUS and brim sites in a rather different manner than H_2S . Thus, it is reasonable to propose that the interaction of DBT and BPh with the metal cations (CUS) enhances the basicity of the surface, i.e., the electronic density of the brim sites.

Thus, it is remarkable that the higher concentration of accessible Ni cations at the rim of the NiMoS particles induces such a dramatic electronic effect that leads to a markedly higher hydrogenation rate. Scanning tunneling microscopy (STM) and DFT calculations suggest a significantly higher electron density in the NiMoS phase that is close to the edge of the sulfide slabs [12]. In the absence of specific DFT calculations on these sites, we would like to speculate that the intrinsically high electron density at these sites facilitates dissociative hydrogen adsorption and hydrogenation and that the presence of the polyfunctional Lewis bases such as DBT increases this electron density further or extends the electron-rich metallic-like zone.

6. Conclusion

The partial substitution of Ni in MoS_2 slabs of $\text{MoS}_2/\gamma\text{-Al}_2\text{O}_3$ increases the reducibility in the sulfidation procedure as well as the concentration of accessible metal cations in $\text{NiMoS}/\gamma\text{-Al}_2\text{O}_3$. The catalytic hydroconversion of *o*-propylaniline occurs via two reaction routes that have been shown unequivocally to occur on two separate sites.

The first reaction pathway, under our experimental conditions the direct elimination of NH_3 from *o*-propylaniline (DDN route), is catalyzed by accessible Mo cations. The presence of Ni cations dilutes these sites and leads to a reduction in the reaction rate along this pathway. It is interesting to note that the reduction in activity fits well to the statistical incorporation of Ni into MoS_2 . If DBT is converted in parallel to *o*-propylaniline, its competitive adsorption reduces the DDN reaction rate by 50%. The identical relative reduction in the DDN rate by

DBT for $\text{MoS}_2/\gamma\text{-Al}_2\text{O}_3$ and $\text{NiMoS}/\gamma\text{-Al}_2\text{O}_3$ is a strong indirect proof that the nature of these sites is identical in both catalysts.

The second reaction pathway, the hydrogenation of the aromatic ring with the subsequent elimination of NH_3 from *o*-propylcyclohexylamine (HYD route), is catalyzed only by brim sites. This is concluded from the absence of a negative effect of the parallel conversion of DBT on the hydroconversion of *o*-propylaniline on $\text{MoS}_2/\gamma\text{-Al}_2\text{O}_3$ and the dramatic enhancement of the rate for $\text{NiMoS}/\gamma\text{-Al}_2\text{O}_3$. If accessible metal cations would be involved in the adsorption site or the active site for the reaction, the presence of DBT should lead to a decrease in the reaction rate, because of the competitive adsorption of DBT. Using the argumentation from STM model studies, we suggest that the higher intrinsic rate is related to the higher electron density at the brim sites in the presence of Ni. It is remarkable that the presence of sulfur compounds enhance this in a dramatic way.

The present contribution shows, therefore, that the local manipulation of the substitution in MoS_2 structures and subtle promotion by coreactants could drastically enhance the hydrogenation ability of supported sulfides enhancing so their ability to hydroconvert heavy feeds.

7. Acknowledgements

This work was supported by Chevron Energy Technology Company. The authors would like to thank Dr. Alexander Kuperman and Dr. Axel Brait for fruitful discussions. The authors are also indebted to Prof. Roel Prins for discussion on the topic of hydrodenitrogenation.

8. References

- [1] T.C. Ho, *Catal. Rev. Sci. Eng.* 30 (1998) 117.
- [2] F. Besenbacher, M. Brorson, B.S. Clausen, S. Helveg, B. Hinnemann, J. Kibsgaard, J.V. Lauritsen, P.G. Moses, J.K. Nørskov, H. Topsøe, *Catal. Today* 130 (2008) 86.
- [3] R. Prins, V.H.J. de Beer, G.A. Somorjai, *Catal. Rev. Sci. Eng.* 31 (1989) 1.
- [4] P. Raybaud, *Appl. Cat. A* 322 (2007) 76.
- [5] M. Sun, A.E. Nelson, J. Adjaye, *J. Catal.* 226 (2004) 32.
- [6] E. Krebs, B. Silvi, P. Raybaud, *Catal. Today* 130 (2008) 160.
- [7] L.S. Byskov, J.K. Nørskov, B.S. Clausen, H. Topsøe, Sulphur bonding in transition metal sulphides and MoS₂ based structures, in T. Weber, R. Prins, R.A. van Santen (eds.), *Transition Metal Sulphides – Chemistry and Catalysis*, Kluwer Academic Publishers, 1998
- [8] Henrik Topsøe, *Appl. Cat. A* 322 (2007) 3.
- [9] J. Kibsgaard, A. Tuxen, K.G. Knudsen, M. Brorson, H. Topsøe, E. Laegsgaard, J.V. Lauritsen, F. Besenbacher, *J. Catal.* 272 (2010) 195.
- [10] M. Sun, J. Adjaye, A.E. Nelson, *Appl. Cat. A* 263 (2004) 131.
- [11] C. Moreau, J. Joffre, C. Saenz, P. Geneste, *J. Catal.* 122 (1990) 448.
- [12] F. Besenbacher, M. Brorson, B.S. Clausen, S. Helveg, B. Hinnemann, J. Kibsgaard, J.V. Lauritsen, P.G. Moses, J.K. Nørskov, H. Topsøe, *Catal. Today* 130 (2008) 86.
- [13] T.C. Ho, L. Qiao, *J. Catal.* 269 (2010) 291.
- [14] S.H. Yang, C.N. Satterfield, *J. Catal.* 81 (1983) 168.
- [15] H.A. Rangwala, I.G. Dalla Lana, F.D. Otto, H. Yeniova, K. Al-Nuaimi, *Energy Fuels* 4 (1990) 599.
- [16] S. Eijsbouts, C. Sudhakar, V.H.J. de Beer, R. Prins, *J. Catal.* 127 (1991) 605.
- [17] S. Eijsbouts, V.H.J. de Beer, R. Prins, *J. Catal.* 127 (1991) 619.
- [18] L. Viver, V. Dominguez, G. Perot, S. Kasztelan, *J. Mol. Catal.* 67 (1991) 267.
- [19] J.L. Lemberon, N. Gnofam, G. Perot, *Appl. Cat. A* 90 (1992) 175.
- [20] R. Prins, M. Jian, M. Flechsenhar, *Polyhedron* 16 (1997) 3235.
- [21] R.Z. Lee, M. Zhang, F.T.T. Ng, *Top. Catal.* 37 (2006) 121.
- [22] X. Li, A. Wang, M. Egorova, R. Prins, *J. Catal.* 250 (2007) 283.
- [23] B.S. Clausen, H. Topsøe, R. Candla, J. Villadsen, B. Lengeler, J. Als-Nielsen, F. Christensen, *J. Phys. Chem.* 85 (1981) 3868.
- [24] Y. Okamoto, K. Ochiai, M. Kawano, K. Kobayashi, T. Kubota, *Appl. Cat. A* 226 (2002) 115.
- [25] A.N. Desikan, L. Huang, S.T. Oyama, *J. Phys. Chem.* 95 (1991) 10050.

- [26] R.W.G. Wyckoff, *Crystal Structures*, 1 (1963) 280, Second edition. Interscience Publishers, New York.
- [27] G. Mestl, T.K.K. Srinivasan, *Catal. Rev. Sci. Eng.* 40 (1998) 451.
- [28] I.E. Wachs, *Catal. Today* 27 (1996) 437.
- [29] J.L. Verble, T.J. Wieting, *Phys. Rev. Letters* 25 (1970) 362.
- [30] T.J. Wieting, J.L. Verble, *Phys. Rev. B* 3 (1971) 4286.
- [31] G.M. do Nascimento, T.B. Silva, P. Corio M.S. Dresselhaus, *J. Raman Spectrosc.* 41 (2010) 1587.
- [32] N.K. Nag, D. Fraenkel, J.A. Moulijn, B.C. Gates, *J. Catal.* 66 (1980) 162.
- [33] P. Arnoldy, J.A.M. van den Heijkant, G.D. de Bok, J.A. Moulijn, *J. Catal.* 92 (1985) 35.
- [34] F. Mauge, J. Lamotte, N.S. Nesterenko, O. Manoilova, A.A. Tsyganenko, *Catal. Today* 70 (2001) 271.
- [35] N.-Y. Topsøe, H. Topsøe, *Bull. Soc. Chim. Belg.* 90 (1981) 1311.
- [36] N.-Y. Topsøe, H. Topsøe, *J. Catal.* 75 (1982) 354.
- [37] Y. Okamoto, A. Maezawa, T. Imanaka, *J. Catal.* 120 (1989) 29.
- [38] N. Koizumi, S. Jung, Y. Hamabe, H. Suzuki, M. Yamada, *Catal. Lett.* 135 (2010) 175.
- [39] N.-Y. Topsøe, H. Topsøe, *J. Catal.* 77 (1982) 293.
- [40] N.-Y. Topsøe, H. Topsøe, *J. Catal.* 84 (1983) 386.
- [41] N.-Y. Topsøe, H. Topsøe, O. Sørensen, B.S. Clausen, R. Candia, *Bull. Soc. Chim. Belg.* 93 (1984) 727.
- [42] N.-Y. Topsøe, A. Tuxen, B. Hinnemann, J.V. Lauritsen, K.G. Knudsen, F. Besenbacher, H. Topsøe, *J. Catal.* 279 (2011) 337.
- [43] B.S. Gevert, J-E. Otterstedt, F.E. Massoth, *Appl. Cat.* 31 (1987) 119.
- [44] R. Prins, *Adv. Catal.* 46 (2001) 399.
- [45] X. Wang, B. Zhao, D. Jiang, Y. Xie, *Appl. Cat. A* 188 (1999) 201.
- [46] J. Medema, C. van Stam, V.H.J. de Beer, A.J.A. Konings, D.C. Koningsberger, *J. Catal.* 53 (1978) 386.
- [47] C.P. Cheng, G.L. Schrader, *J. Catal.* 60 (1979) 276.
- [48] J. Leyrer, M.I. Zaki, H. Knözinger, *J. Phys. Chem.* 90 (1986) 4775.
- [49] P. Zeuthen, P. Blom, B. Muegge, F.E. Massoth, *Appl. Cat.* 68 (1991) 117.
- [50] R. Cattaneo, T. Weber, T. Shido, R. Prins, *J. Catal.* 191 (2000) 225.
- [51] J.C. Muijsers, T. Weber, R.M. van Hardeveld, H.W. Zandbergen, J.W. Niemantsverdriet, *J. Catal.* 157 (1995) 698.
- [52] T. Weber, J.C. Muijsers, J.H.M.C. van Wolput, C.P.J. Verhagen, J.W. Niemantsverdriet, *J. Phys. Chem.* 100 (1996) 14144.

- [53] M. Jian, R. Prins, *Catal. Today* 30 (1996) 127.
- [54] M. Sun, R. Prins, *J. Catal.* 201 (2001) 138.
- [55] L. Qu, R. Prins, *J. Catal.* 210 (2002) 183.
- [56] P. Clark, X. Wang, P. Deck, S.T. Oyama, *J. Catal.* 210 (2002) 116.
- [57] L. Qu, M. Flechsenhar, R. Prins, *J. Catal.* 217 (2003) 284.
- [58] F. Rota, R. Prins, *Top. Catal.* 11/12 (2000) 327.
- [59] L. Qu, R. Prins, *Appl. Catal. A* 250 (2003) 105.
- [60] Y. Zhao, P. Kukula, R. Prins, *J. Catal.* 221 (2004) 441.
- [61] Y. Zhao, R. Prins, *J. Catal.* 229 (2005) 213.
- [62] R. Prins, Y. Zhao, N. Sivasankar, P. Kukula, *J. Catal.* 234 (2005) 509.
- [63] R. Prins, M. Egorova, A. Röthlisberger, Y. Zhao, N. Sivasankar, P. Kukula, *Catal. Today* 111 (2006) 84.
- [64] K. Shanthi, C.N. Pillai, J.C. Kuriacose, *Appl. Catal.* 46 (1989) 241.
- [65] R.T. Hanlon, *Energy Fuels* 1 (1987) 424.
- [66] M. Sun, A.E. Nelson, J. Adjaye, *Catal. Lett.* 109 (2006) 133.
- [67] T.F. Jaramillo, K.P. Jørgensen, J. Bonde, J.H. Nielsen, S. Horch, I. Chorkendorff, *Science*, 317 (2007) 100.
- [68] B. Hinnemann, P.G. Moses, J. Bonde, K.P. Jørgensen, J.H. Nielsen, S. Horch, I. Chorkendorff, J.K. Nørskov, *J. Am. Chem. Soc.* 127 (2005) 5308.
- [69] H. Topsøe, B.S. Clausen, N.-Y. Topsøe, E. Pedersen, W. Niemann, A. Müller, H. Bögge, B. Lengeler, *J. Chem. Soc., Faraday Trans. I* 83 (1987) 2157.
- [70] V. Veefkind, J.A. Lercher, *J. Catal.* 180 (1998) 258.
- [71] E. Furimsky, F. Massoth, *Catal. Rev.* 47 (2005) 297.
- [72] G.C. Hadjiloizou, J.B. Butt, J.S. Dranoff, *J. Catal.* 135 (1992) 27.
- [73] F.E. Massoth, S.C. Kim, *Catal. Lett.* 57 (1999) 129.
- [74] M. Marafi, A. Stanislaus, *Appl. Catal. A* 159 (1997) 259.
- [75] J. Van Gestel, C. Dujardin, J.C. Duchet, *J. Catal.* 202 (2001) 78.

Chapter 3

C(sp³)-N bond cleavage in the ring opening of 1,2,3,4-tetrahydroquinoline and decahydroquinoline on Mo and NiMo/ γ -Al₂O₃ sulfide catalysts

The hydrodenitrogenation (HDN) of decahydroquinoline and quinoline was studied at 370 °C and 5 MPa on MoS₂/ γ -Al₂O₃ and NiMoS/ γ -Al₂O₃ catalysts in the presence and absence of dibenzothiophene. The reaction proceeds via two sequences, i.e., decahydroquinoline → propylcyclohexylamine → propylcyclohexene → propylcyclohexane, in which the ring opening is the rate limiting step, and via 1,2,3,4-tetrahydroquinoline → o-propylaniline → propylcyclohexylamine and propylbenzene, in which the o-propylaniline hydrogenation is the rate limiting step. The intrinsic rate of C(sp³)-N bond cleavage is lower in 1,2,3,4-tetrahydroquinoline than in decahydroquinoline, because the nitrogen free electron pair in 1,2,3,4-tetrahydroquinoline interacts with the aromatic ring. The active sites for the ring opening via Hofmann elimination are acidic -SH groups and basic S²⁻ ions. The conversion of dibenzothiophene via direct desulfurization on coordinatively unsaturated sites provides surface sulfur increasing the concentration of S²⁻ ions and -SH groups. Nickel facilitates activation and mobility of hydrogen and simultaneously increases the basicity of S²⁻ groups.

1. Introduction

The increasing demand for transportation fuels and the rigorous specifications for sulfur and nitrogen content in these fuels have led to a high interest in the catalytic chemistry of the removal of heteroatoms [1,2]. Conventionally, the conversion of nitrogen-containing compounds is achieved by hydrodenitrogenation (HDN) on alumina-supported MoS₂ catalysts promoted with Ni or Co, at high hydrogen pressures. Nitrogen-containing organic compounds can be present as, non-heterocyclic and heterocyclic structures. The non-heterocyclic anilines and aliphatic amines undergo HDN quickly, whereas the more abundant heterocyclic compounds containing five-member pyrrolic or six-member pyridinic rings are difficult to convert [3].

Quinoline is a good model compound for HDN studies, because its bicyclic aromatic nature provides detailed insight to the HDN elementary steps expected in a real feedstock [4-9]. The saturation of the heteroatom containing quinoline ring prior to C(sp³)-N bond cleavage is mandatory, because the high energy of the C(sp²)-N bond in an aromatic ring prevents its cleavage [10]. This hydrogenation step and the subsequent saturation of the benzoic ring are reversible and exothermic, thus, the equilibrium concentration of the saturated ring decreases with temperature [11]. In contrast, the ring opening via C(sp³)-N bond cleavage is an irreversible reaction under typical HDN reaction conditions.

Understanding the mechanistic differences in the C(sp³)-N bond cleavage of the intermediates is challenging, even when quinoline is used as the single model compound, because the nitrogen-containing intermediates adsorb strongly and compete for the adsorption sites. Therefore, we have decided to address the initial steps, i.e., the HDN of quinoline and decahydroquinoline (DHQ). This approach offers the possibility to evaluate the initial hydrogenation/dehydrogenation steps followed by the C(sp³)-N bond cleavage in 1,2,3,4-tetrahydroquinoline (14THQ) and DHQ leading to o-propylaniline (OPA) and propylcyclohexylamine (PCHA), respectively.

The individual rates are not only strongly influenced by the adsorption of intermediates, but also by the presence of sulfur-containing compounds and by the promotion of MoS₂ by cations such as Ni and Co. The presence of H₂S or sulfur containing reactants such as dibenzothiophene (DBT) during HDN promotes the C(sp³)-N bond cleavage, while it inhibits the hydrogenation [12-14]. These effects are usually rationalized in terms of S²⁻ and -SH groups formation that are crucial for the catalyst activity [15-16].

The role of Ni as promoter and key element of forming coordinatively unsaturated sites (CUS) in HDN is controversial. It has been established that the direct removal of sulfur and

nitrogen atoms occurs on CUS via a reverse Mars-van Krevelen-type mechanism. However, the promoter atom inhibits the direct denitrogenation (DDN) route for several model compounds even though the addition of Ni increases the CUS concentration [14,17-19]. On the other hand the addition of Ni to MoS₂ promotes the hydrogenation of the phenyl ring of OPA. Thus, it has been concluded that only Mo-associated CUS are catalytically active for the direct C(sp²)-N bond cleavage, whereas nickel increases the electron density close to the edges of the sulfide slabs (brim sites) where hydrogenation may take place [20-22].

The ring opening steps of bicyclic molecules, e.g., 14THQ and DHQ, has received less attention than the DDN and hydrogenation steps. However the efficiency of the overall quinoline HDN process depends in a large extent in the ability of the catalyst to cleavage the C(sp³)-N bond prior to the complete removal of N. In the current work, we explore the effect of Ni as promoter in MoS₂ and the impact of DBT for the separate HDN of quinoline and DHQ. The emphasis is put on the understanding of the active sites involved in the ring opening reaction via C(sp³)-N bond cleavage.

2. Experimental

2.1. Catalyst synthesis and characterization

Catalyst synthesis and physicochemical properties. The Mo and NiMo oxide catalyst precursors were prepared by consecutive incipient wetness impregnation on γ -Al₂O₃ support (BET specific surface area of 237 m²/g) using aqueous solution of ammonium heptamolybdate, (NH₄)₆Mo₇O₂₄·4H₂O (Aldrich), and nickel nitrate, (NO₃)₂·6H₂O (Aldrich). After each impregnation, the oxide catalysts were dried overnight at 120 °C and then calcined at 500 °C for 4 h (heating rate of 1 °C/min) in synthetic air flow. Hereafter, the oxidic precursors are referred as Mo/ γ -Al₂O₃ and NiMo/ γ -Al₂O₃, whereas the sulfide catalysts are denoted as MoS₂/ γ -Al₂O₃ and NiMoS/ γ -Al₂O₃.

The chemical composition of the synthesized oxidic catalyst precursors was determined by elemental analysis carried out at the Microanalytical Laboratory at the TU München.

NO adsorption as a pulse experiment at room temperature was applied to probe the active sites and the average edge dispersion in the metal sulfide catalysts, such as MoS₂/ γ -Al₂O₃ and NiMoS/ γ -Al₂O₃. The pulses were applied in a quartz flow reactor with a Balzers mass spectrometer as detector. Prior to the NO adsorption, the catalysts were activated in situ in 10% H₂S in H₂ as described elsewhere [16].

Temperature-programmed reduction and desorption. Temperature-programmed reduction (TPR) was used to analyze the reducibility of the Mo/ γ -Al₂O₃ and NiMo/ γ -Al₂O₃ sulfide catalysts, while temperature-programmed desorption (TPD) was used to analyze the strength of potentially active site via desorption of the adsorbed species. Experiments were carried out in a quartz tubular reactor and the evolved gases were detected by a mass spectrometer (Balzers QME 200). Prior to the experiments, oxidic catalyst precursors (0.1 g) were activated in situ for 2 h in 10% H₂S in H₂ at 400 °C, with a heating rate of 5 °C/min. Cooling to room temperature in the presence of the sulfiding agent was followed by flushing of the reactor with high purity He for 1 hour, in order to remove H₂S. In the case of TPR studies, the catalysts were then heated in 20% H₂ in He to 750 °C with an increment of 5 °C/min, while the desorbed H₂S formed in the surface reaction with H₂ was measured. For the TPD studies, after cooling to room temperature the reactor was flushed with pure He flow to 400 °C with heating rate of 5 °C/min. The desorption of H₂S and H₂ was followed.

2.2. Kinetic test

The kinetic studies were carried out in a continuous flow trickle bed reactor system at a constant temperature, pressure and feed composition. A stainless steel, glass lined coated reactor was loaded with 0.05 g of catalyst for each run. Gas and liquid feed were introduced into the reactor via high pressure mass flow meters (Bronkhorst) and a HPLC pump (Shimadzu LC-20AD), respectively. After separation of liquid and gas effluent phase, the liquid was collected via 16 port sampling valve every 1.5 hours. The liquid samples were analyzed by off line gas chromatography with a HP 6890 GC instrument equipped with a flame ionization detector (FID) and an Agilent DB-17 capillary column.

Prior to the experiments, catalysts were activated in situ in 10% H₂S in H₂ flow at 400 °C and 1.8 MPa for 8 hours. The HDN reactions were performed at 370 °C and total pressure of 5.0 MPa. The steady state was reached after 16 hour time on stream. The HDN was investigated as a space time dependent experiment. Space time was defined as m_{cat}/F_N , where m_{cat} is the amount of the oxide catalyst precursor and F_N is the molar flow of nitrogen-containing compound [(h)·(g of catalyst)/(mol of N-containing compound)]. The reactions were performed in excess of hydrogen keeping the ratio of liquid and gas flow constant to ensure constant partial pressures. The initial concentration of quinoline (Aldrich, 98%) and DHQ (Aldrich, mixture of cis and trans, 97%) was set to 1000 ppm N in a mixture of 5% hexadecane (Merck, 99%) in tetradecane (Alfa Aesar, 99+%) as a solvent. For studying the effect of sulfur containing compound on the HDN reaction, DBT (Aldrich, 99%) was applied in a concentration of 500 ppm S.

The conversion towards nitrogen free products was referred as the HDN conversion and it is calculated accordingly:

$$\text{HDN conversion} = \frac{C_{[\text{Nx}]_0} - C_{[\text{Nx}]} - C_{[\text{N}]}}{C_{[\text{Nx}]_0}}$$

where $C_{[\text{Nx}]_0}$ is the initial concentration of the studied compound x (quinoline or decahydroquinoline) and $C_{[\text{Nx}]}$ is the concentration of the studied compound x at the measured space time and $C_{[\text{N}]}$ is the concentration of all nitrogen containing compounds at the measured space time.

3. Results

3.1. Catalyst characterization

3.1.1. Physicochemical properties

The metal concentration as determined by elemental analysis was 8.6 wt.% Mo in the unpromoted and 8.6 wt.% Mo and 3.6 wt.% Ni in the promoted oxidic catalyst precursor. The concentration of Mo in both Mo/ γ -Al₂O₃ and NiMo/ γ -Al₂O₃ catalysts was 2.5 atoms/nm² which is far below the monolayer concentration of 4.6 atoms/nm² determined for the oxide precursors on alumina [23]. Therefore, the samples are considered to be well dispersed on the alumina support and even after catalyst activation in 10% H₂S in H₂, stacking of the MoS₂ or NiMoS slabs was not observed, as seen in the XRD (as shown in Fig. 1 in Chapter 2). The total NO uptake on the MoS₂/ γ -Al₂O₃ and NiMoS/ γ -Al₂O₃ catalysts was 130 and 160 $\mu\text{mol/g}_{\text{cat}}$. Considering that neither the support material (γ -Al₂O₃) nor Mo⁶⁺ cations adsorb NO strongly [24,25] and that two molecules of NO adsorb on one exposed cation [26], the concentration of CUS was estimated to be 65 $\mu\text{mol/g}_{\text{cat}}$ for MoS₂/ γ -Al₂O₃ and 80 $\mu\text{mol/g}_{\text{cat}}$ for NiMoS/ γ -Al₂O₃. Therefore, the addition of 3.6 wt.% of Ni, with the molar fraction of Ni/(Ni+Mo)=0.4, enhanced the concentration of the CUS by approximately 25%. This is in good agreement with the generally accepted idea that the promoters facilitate the creation of accessible cations in sulfide catalysts.

3.1.2. Temperature-programmed desorption (TPD) and reduction (TPR)

The TPD profiles of H₂S and H₂ are shown in Figs. 1 and 2, respectively for MoS₂/ γ -Al₂O₃ and NiMoS/ γ -Al₂O₃ catalyst. Both catalysts exhibited equal profile of H₂S desorption, Fig. 1. The low temperature peak, at 110 °C, assigned to physisorbed H₂S, exhibited the most intense maximum among the peaks. The low intensity peak at around 320 °C and the one at 400 °C are associated to the desorption of H₂S after recombination of -SH groups within the

same MoS₂ or NiMoS slab. As a result of this recombination, bridging S²⁻ groups are formed (Mo-S-Mo) without consumption of H₂ [27]. The peak at 400 °C is assigned to the recombination of two -SH groups from different slabs that sinter due to the high temperature [27]. The TPD profile of H₂ exhibited the onset of desorption at around 100 °C for both sulfide catalysts even though the complete profile differed, Fig. 2. On the MoS₂/γ-Al₂O₃ catalyst, two desorption peaks were observed at 230 and 330 °C with a shoulder at 400 °C. The promoted NiMoS/γ-Al₂O₃ catalysts exhibited a main desorption peak at 320 °C with two shoulders at 245 and 400 °C.

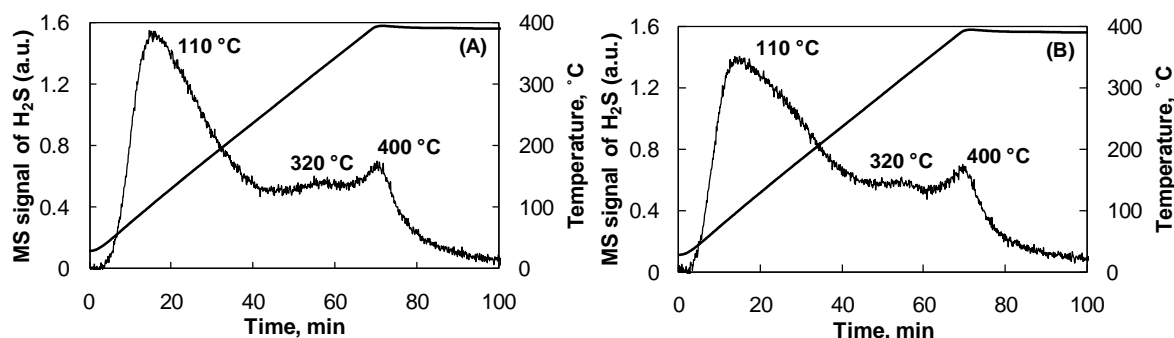


Figure 1. Temperature programmed desorption of H₂S from (A) MoS₂/γ-Al₂O₃ and (B) NiMoS/γ-Al₂O₃ catalyst.

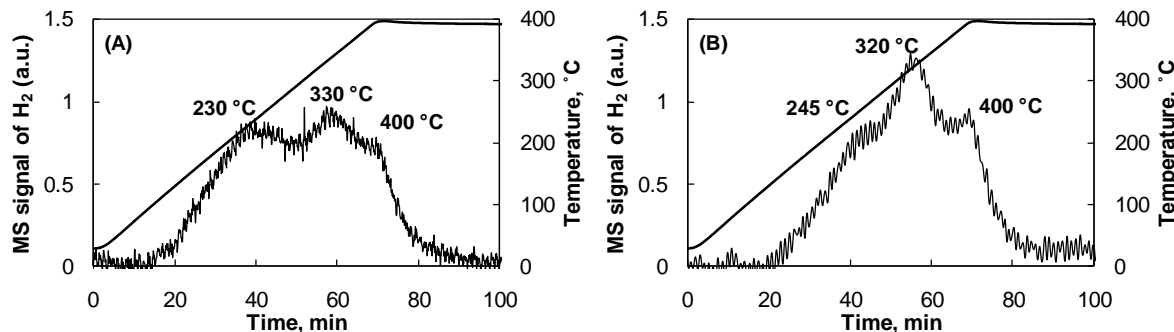


Figure 2. Temperature programmed desorption of H₂ from (A) MoS₂/γ-Al₂O₃ and (B) NiMoS/γ-Al₂O₃ catalyst.

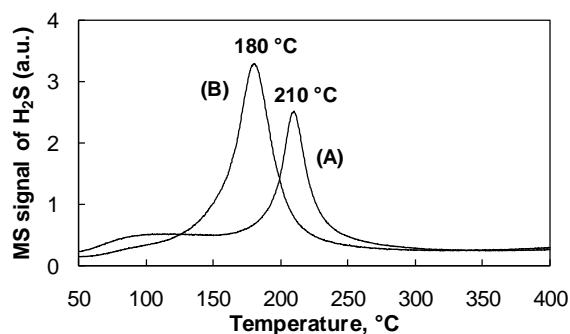


Figure 3. H₂S mass spectrometer signal followed during the temperature programmed reduction of (A) MoS₂/γ-Al₂O₃ and (B) NiMoS/γ-Al₂O₃ catalyst.

The TPR of MoS₂/γ-Al₂O₃ and NiMoS/γ-Al₂O₃ catalysts was followed through the H₂S mass signal as shown in Fig. 3. The H₂S release at low temperature (onset at 70 °C) can be attributed to physisorbed H₂S. The H₂S release at higher temperature is a product of the catalyst reduction by H₂ and not a product of -SH groups recombination, given that the TPD did not exhibit any H₂S desorption in the same temperature range. The reduction temperature shifted from 210 °C for MoS₂/γ-Al₂O₃ to 180 °C for NiMoS/γ-Al₂O₃.

3.2. Hydrodenitrogenation of decahydroquinoline (DHQ)

3.2.1. HDN reaction network

The product yield as a function of the DHQ conversion in absence and presence of DBT is shown in Figs. 4 and 5 for MoS₂/γ-Al₂O₃ and NiMoS/γ-Al₂O₃. The dehydrogenated products detected were 14THQ, 5,6,7,8-tetrahydroquinoline (58THQ), and quinoline. Products formed from ring opening reactions were OPA and PCHA and the final nitrogen free products in all studied conditions were propylbenzene (PB), PCH, and PCHE in form of three equilibrated isomers: 1-propylcyclohexene, 3-propylcyclohexene and propylidene cyclohexane. The primary products, exhibiting a linear correlation between yield and initial DHQ conversion, were 14THQ (dehydrogenation of the benzoic ring in DHQ), 58THQ (dehydrogenation of the pyridinic ring in DHQ) and PCHA (ring opening reaction via C(sp³)-N bond cleavage). The equilibrium between quinoline and 14THQ was rapidly reached, as shown in Fig. 6 (A), thus quinoline is also discussed as primary product. For the following analysis, therefore, quinoline and 14THQ were lumped together. The rate of 58THQ formation was the highest among the observed primary products as seen in Fig. 4 (B). The thermodynamic equilibrium between 58THQ and DHQ is reached at space time longer than 120 h·g_{cat}/mol, as shown in Fig. 6 (B). The PCHA and OPA intermediates, formed from the ring opening reactions, were detected in very low concentrations (< 3%), Fig. 4 (C) and (D). Among the nitrogen free products, Fig. 5, the only aromatic end product PB, exhibited the lowest yield compared to the unsaturated PCHE intermediate and the saturated PCH end product.

During the HDN of DHQ, the conversion of DBT was also followed on MoS₂/γ-Al₂O₃ and NiMoS/γ-Al₂O₃, see Fig. 7. The promoted catalyst exhibited higher hydrodesulfurization (HDS) activity, e.g., at the space time of 100 h·g_{cat}/mol, the DBT conversion was 12% on MoS₂/γ-Al₂O₃ and 95% on NiMoS/γ-Al₂O₃ catalyst. The product distribution, shown in Fig. 8 (B), indicated that the main route for DBT conversion was the direct desulfurization (DDS), in which biphenyl (BPh) was formed. Low concentrations of phenylcyclohexane (PhCH) were detected over the whole space time, < 2% on MoS₂/γ-Al₂O₃ and < 8% on NiMoS/γ-Al₂O₃ catalyst, Fig. 8 (A).

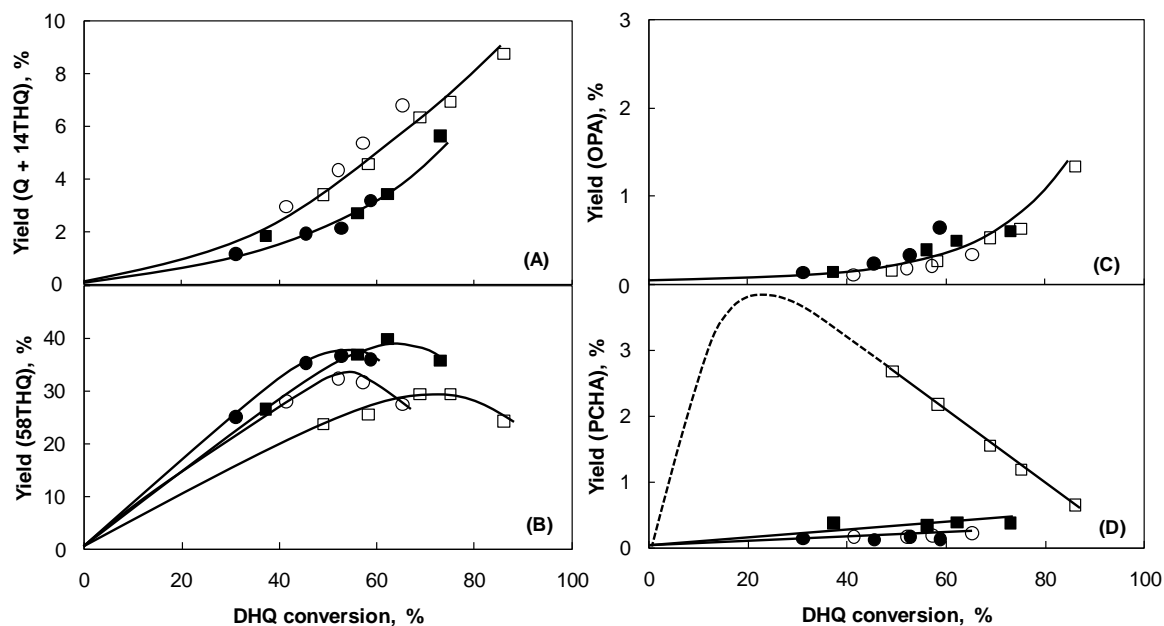


Figure 4. Yield of quinoline + 1,2,3,4-tetrahydroquinoline (A), 5,6,7,8-tetrahydroquinoline (B), o-propylaniline (C), and propylcyclohexylamine (D) as a function of DHQ conversion on MoS₂/γ-Al₂O₃ (●,■) and NiMoS/γ-Al₂O₃ (○,□) catalyst. The experiments were carried out in the absence (●,○) and presence of 3.4 kPa DBT (■,□).

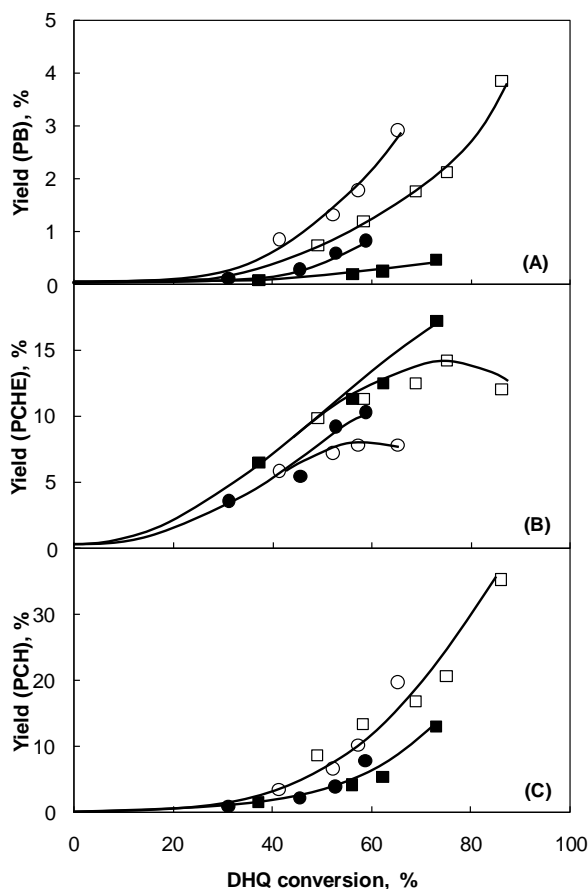


Figure 5. Yield of propylbenzene (A), propylcyclohexene (B), and propylcyclohexane (C) as a function of DHQ conversion on MoS₂/γ-Al₂O₃ (●,■) and NiMoS/γ-Al₂O₃ (○,□) catalyst. The experiments were carried out in the absence (●,○) and presence of 3.4 kPa DBT (■,□).

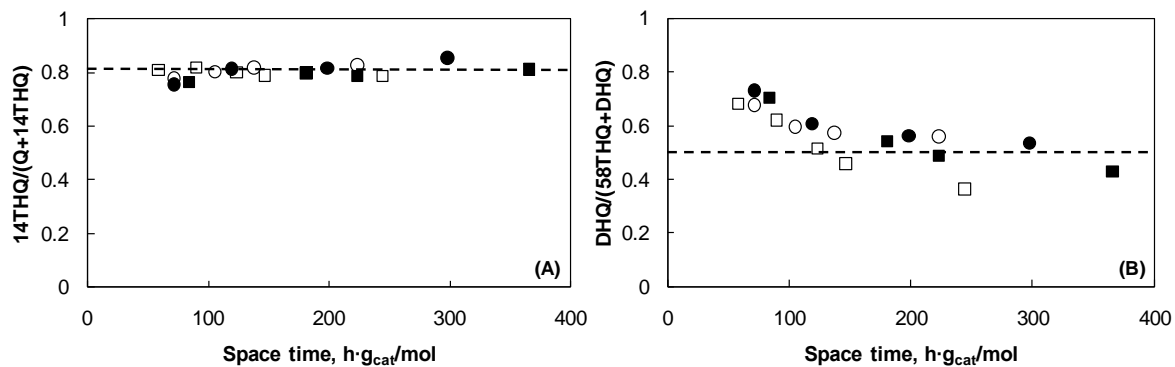


Figure 6. Equilibrium (dotted line) between: quinoline and 14THQ (A) and DHQ and 58THQ (B), when the DHQ HDN is carried out on $\text{MoS}_2/\gamma\text{-Al}_2\text{O}_3$ (●,■) and $\text{NiMoS}/\gamma\text{-Al}_2\text{O}_3$ (○,□) catalyst in the absence (●,○) and presence of 3.4 kPa DBT (■,□).

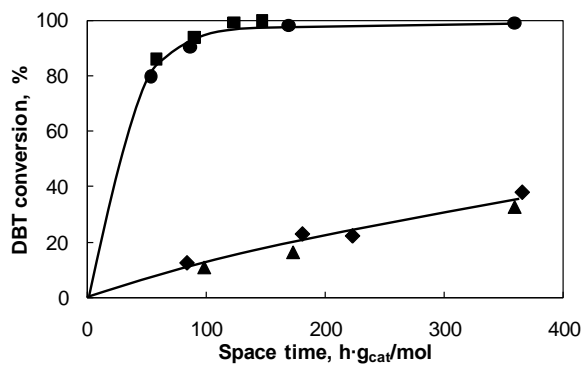


Figure 7. DBT conversion in the parallel reaction with the HDN of DHQ (◆,■) or quinoline (▲,●), carried out on $\text{MoS}_2/\gamma\text{-Al}_2\text{O}_3$ (◆,▲) and $\text{NiMoS}/\gamma\text{-Al}_2\text{O}_3$ (■,●) catalyst.

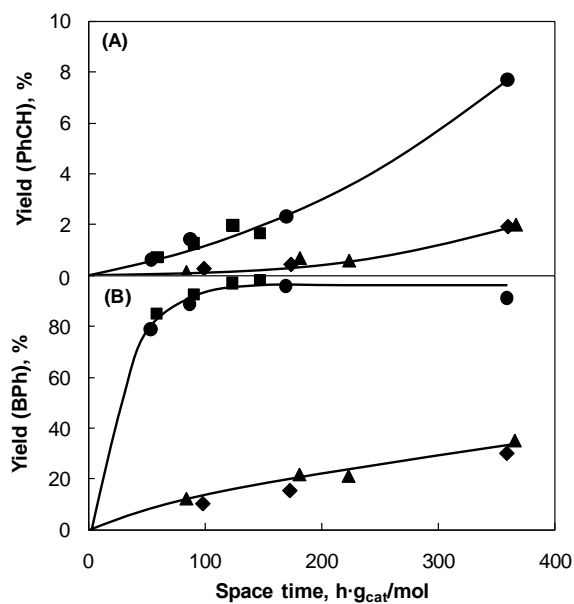


Figure 8. The yield of PhCH (A) and BPh (B) in the parallel HDS of DBT and HDN of DHQ (◆,■) or quinoline (▲,●), carried out on $\text{MoS}_2/\gamma\text{-Al}_2\text{O}_3$ (◆,▲) and $\text{NiMoS}/\gamma\text{-Al}_2\text{O}_3$ (■,●) catalyst.

3.2.2. Effect of Ni promoter and dibenzothiophene (DBT)

The total conversion of DHQ and HDN conversion are shown in Fig. 9 (A) and (B), respectively. For both studied conditions, in the absence and presence of 3.4 kPa DBT, NiMoS/ γ -Al₂O₃ was more active than MoS₂/ γ -Al₂O₃. The promoting effect of Ni was more pronounced, when the reaction was carried out in the presence of DBT, i.e., DBT influenced only slightly the conversion on MoS₂/ γ -Al₂O₃, but a clear positive effect was observed on NiMoS/ γ -Al₂O₃. The non-linear increase of the total DHQ conversion, Fig. 9 (A), is a direct consequence of approaching the equilibrium between DHQ and 58THQ on a longer space time, as shown in Fig. 6 (B). Equilibrium concentrations, predicted by thermodynamic calculations (shown in the Supplementary material), between the two, are reached on space time approximately above 120 h·g_{cat}/mol.

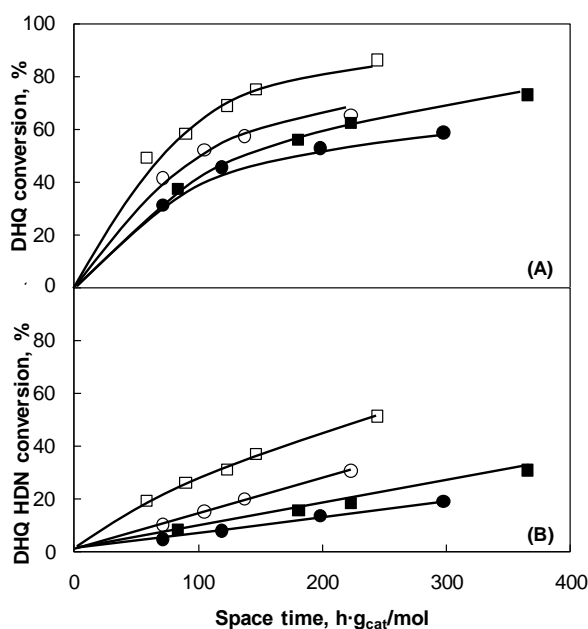


Figure 9. DHQ conversion (A) and HDN conversion (B) as a function of space time on MoS₂/ γ -Al₂O₃ (●,■) and NiMoS/ γ -Al₂O₃ (○,□) catalyst. The experiments were carried out in the absence (●,○) and presence of 3.4 kPa DBT (■,□).

The yields of the individual products are presented in Figs. 10 and 11 for better understanding of how Ni and DBT affect the HDN product distribution. The rate of DHQ dehydrogenation to 14THQ was three times higher on NiMoS/ γ -Al₂O₃ than on MoS₂/ γ -Al₂O₃ catalyst in the absence and presence of DBT, Fig. 10 (A). DBT enhanced the dehydrogenation rate of DHQ to 14THQ by 25% on both catalysts. The initial rate of DHQ dehydrogenation to 58THQ was affected, in contrast, neither by Ni nor by the presence of DBT, Fig. 10 (B). Further conversion of 58THQ was higher on NiMoS/ γ -Al₂O₃, especially in the presence of DBT.

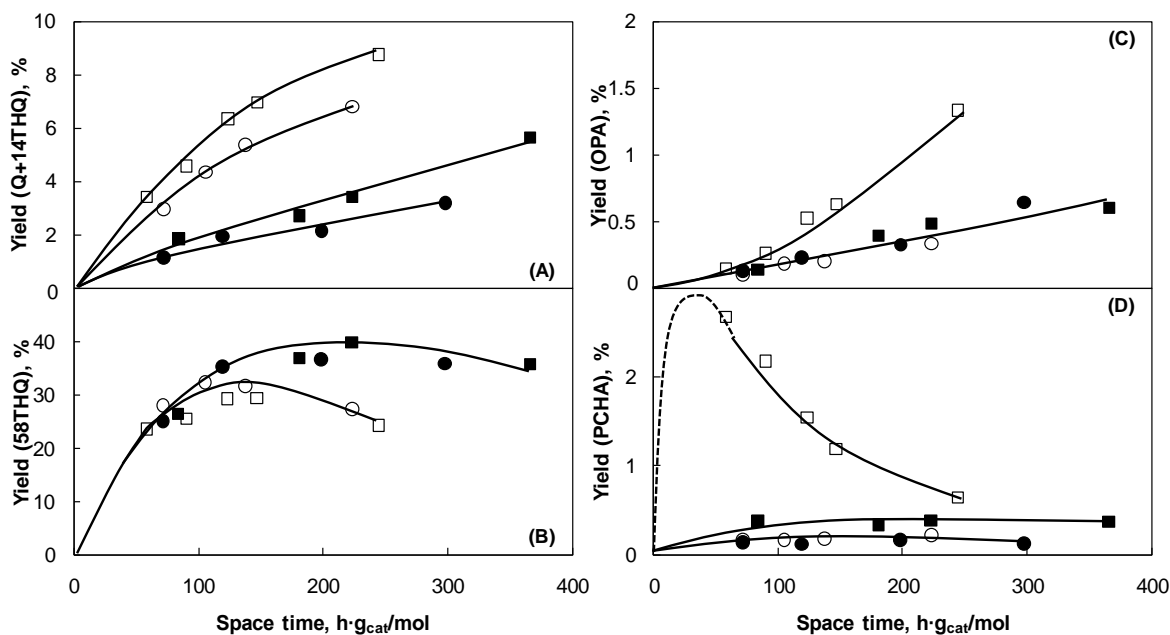


Figure 10. Yield of quinoline + 1,2,3,4-tetrahydroquinoline (A), 5,6,7,8-tetrahydroquinoline (B), o-propylaniline (C), and propylcyclohexylamine (D) as a function of space time in DHQ HDN carried out on MoS₂/γ-Al₂O₃ (●,■) and NiMoS/γ-Al₂O₃ (○,□) catalyst. The experiments were carried out in the absence (●,○) and presence of 3.4 kPa DBT (■,□).

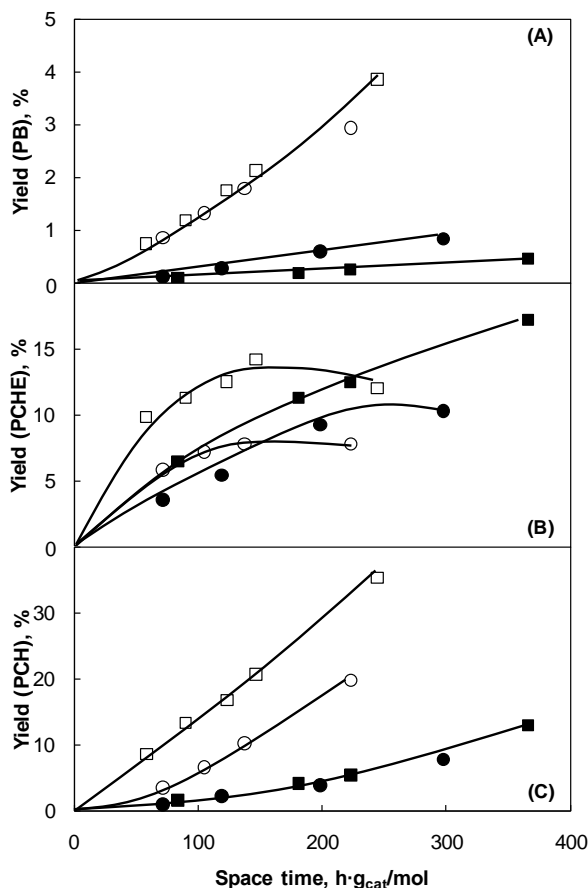


Figure 11. Yield of propylbenzene (A), propylcyclohexene (B), and propylcyclohexane (C) as a function of space time in DHQ HDN carried out on MoS₂/γ-Al₂O₃ (●,■) and NiMoS/γ-Al₂O₃ (○,□) catalyst. The experiments were carried out in the absence (●,○) and presence of 3.4 kPa DBT (■,□).

Fig. 10 shows that the rates of OPA and PCHA formation via C(sp³)-N bond cleavage of 14THQ and DHQ, respectively, were very low. This reaction step was promoted by DBT on both catalysts, but the effect was much more pronounced on NiMoS/ γ -Al₂O₃. Also the rates of formation of nitrogen free products PB, PCHE, and PCH (Fig. 11) were higher on NiMoS/ γ -Al₂O₃ than on MoS₂/ γ -Al₂O₃. DBT inhibited the rate of PB formation by 50% on MoS₂/ γ -Al₂O₃ catalyst, while effects of DBT were not observed on NiMoS/ γ -Al₂O₃. The rate of PCHE formation was promoted by DBT on both catalysts. The rate of PCH formation was not affected by DBT on MoS₂/ γ -Al₂O₃, while it was promoted on NiMoS/ γ -Al₂O₃.

3.3. Hydrodenitrogenation of quinoline

3.3.1. HDN reaction network

The product yields as a function of the quinoline conversion in the absence and in the presence of DBT are shown in Figs. 12 and 13 for MoS₂/ γ -Al₂O₃ and NiMoS/ γ -Al₂O₃. The products detected were equal to the ones in the HDN of DHQ. The fast equilibrium between quinoline and 14THQ was confirmed, as shown in Fig. 14 (A), thus, in the further discussion, the two equilibrated compounds are considered as educts. Moreover, (quinoline + 14THQ) conversion is presented in the following instead of quinoline conversion alone.

The primary products were DHQ, 58THQ and OPA because they exhibited a linear dependency of the concentration at the initial quinoline + 14THQ conversion. DHQ, formed by the hydrogenation of the benzoic ring in 14THQ, and 58THQ, formed by the hydrogenation of the benzoic ring in quinoline, exhibited concentrations of about 10%, at 30% conversion, Fig. 12 (A) that correspond to equilibrium concentrations, as seen in Fig. 14 (B).

OPA, formed from the ring opening of 14THQ, exhibited maximum yield of about 8%, after which it was further converted, Fig. 12 (C). The other ring opening intermediate, PCHA, was either not detected or the concentration did not exceed 1%. PB, the only aromatic nitrogen free end product, exhibited the lowest yield compared to unsaturated PCHE intermediate and saturated PCH end product, Fig. 13.

During the HDN of quinoline, the conversion of DBT was also followed for both catalysts, Fig. 7. As in the case of the DHQ HDN reaction, the promoted catalyst exhibited higher HDS activity. The main route for DBT conversion was the DDS route, in which BPh was formed, Fig. 8 (B). In parallel, low concentration of PhCH was observed on both catalysts, Fig. 8 (A).

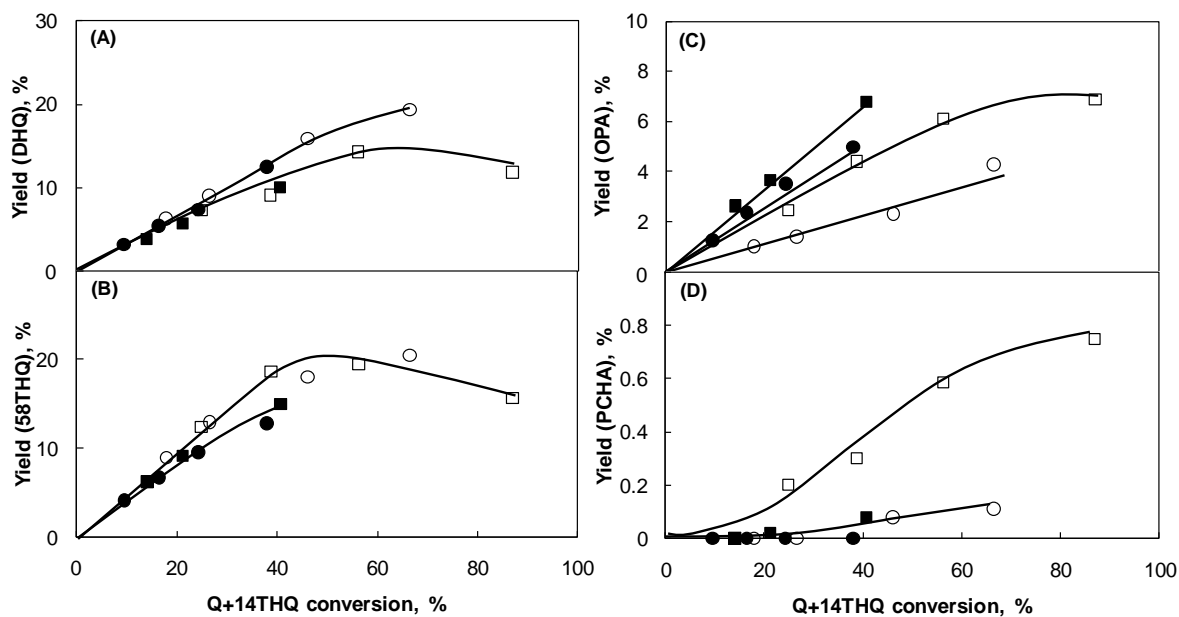


Figure 12. Yield of decahydroquinoline (A), 5,6,7,8-tetrahydroquinoline (B), o-propylaniline (C), and propylcyclohexylamine (D) as a function of (Q+14THQ) conversion on MoS₂/γ-Al₂O₃ (●,■) and NiMoS/γ-Al₂O₃ (○,□) catalyst. The experiments were carried out in the absence (●,○) and presence of 3.4 kPa DBT (■,□).

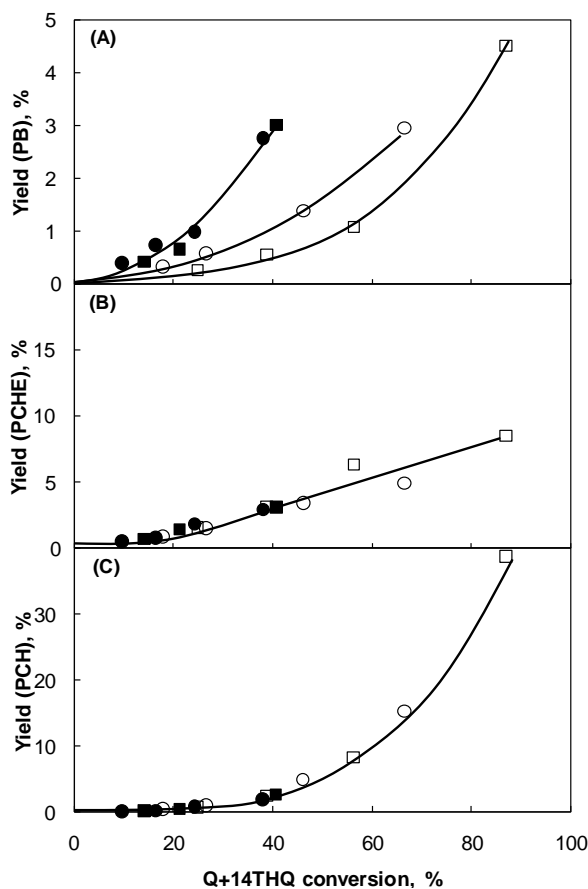


Figure 13. Yield of propylbenzene (A), propylcyclohexene (B), and propylcyclohexane (C) as a function of (Q+14THQ) conversion on MoS₂/γ-Al₂O₃ (●,■) and NiMoS/γ-Al₂O₃ (○,□) catalyst. The experiments were carried out in the absence (●,○) and presence of 3.4 kPa DBT (■,□).

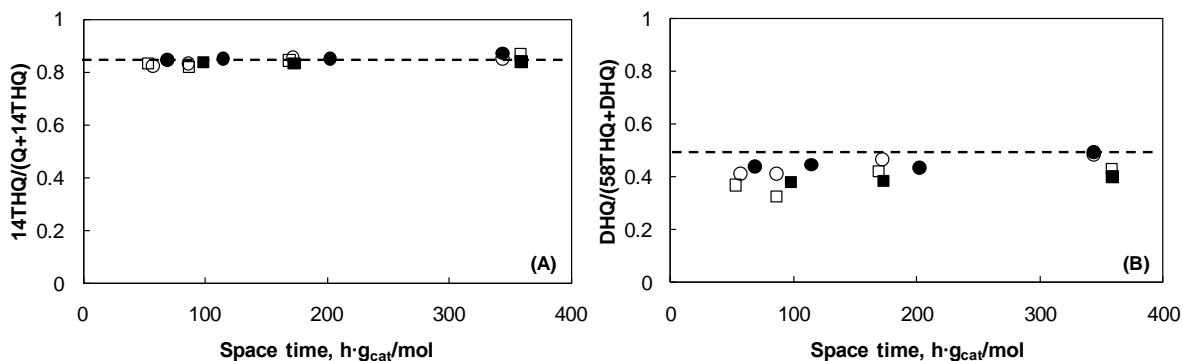


Figure 14. Equilibrium (dotted line) between: quinoline and 14THQ (A) and DHQ and 58THQ (B), when quinoline HDN is carried out on $\text{MoS}_2/\gamma\text{-Al}_2\text{O}_3$ (●,■) and $\text{NiMoS}/\gamma\text{-Al}_2\text{O}_3$ (○,□) catalyst in the absence (●,○) and presence of 3.4 kPa DBT (■,□).

3.3.2. Effect of Ni promoter and DBT

The total conversion of quinoline and 14THQ and HDN conversion are shown in Fig. 15 (A) and (B), respectively. The rate of nitrogen removal was at first negligible and only at space time above 100 $\text{h}\cdot\text{g}_{\text{cat}}/\text{mol}$ the rate increased. $\text{NiMoS}/\gamma\text{-Al}_2\text{O}_3$ catalyst was superior to $\text{MoS}_2/\gamma\text{-Al}_2\text{O}_3$ catalyst under both conditions studied, i.e., in the absence and presence of 3.4 kPa DBT. The promoting effect of Ni was more pronounced, when the reaction was carried out in the presence of DBT, i.e., DBT did not influence the conversion when the quinoline HDN was carried out on $\text{MoS}_2/\gamma\text{-Al}_2\text{O}_3$; in contrast, a positive effect was observed on $\text{NiMoS}/\gamma\text{-Al}_2\text{O}_3$ catalyst.

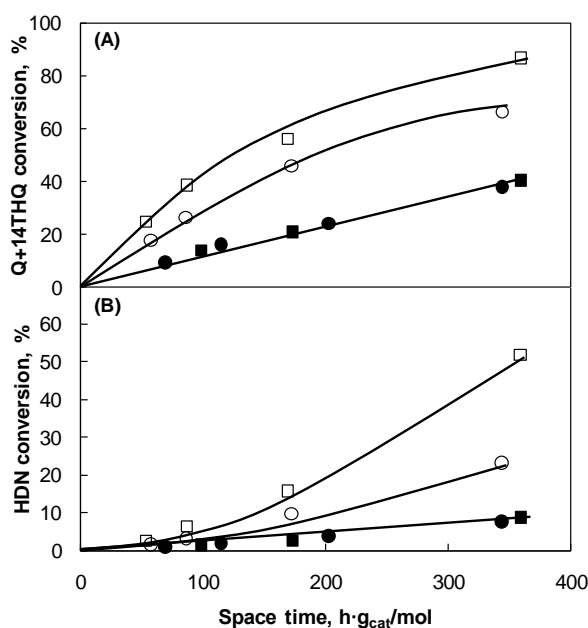


Figure 15. (Q+14THQ) conversion (A) and HDN conversion (B) as a function of space time on $\text{MoS}_2/\gamma\text{-Al}_2\text{O}_3$ (●,■) and $\text{NiMoS}/\gamma\text{-Al}_2\text{O}_3$ (○,□) catalyst. The experiments were carried out in the absence (●,○) and presence of 3.4 kPa DBT (■,□).

The yields of the individual products as a function of the space time are presented in Figs. 16 and 17 for the detailed analysis of how the DBT affect the HDN product distribution. Fig. 16 (B) shows that the hydrogenation rate of the benzoic ring in quinoline, leading to the 58THQ formation, was higher on NiMoS/ γ -Al₂O₃ than on MoS₂/ γ -Al₂O₃ catalyst, two times in the absence of DBT and three times in the presence of DBT. The hydrogenation rate of the benzoic ring in 14THQ, leading to DHQ formation, was three times higher on NiMoS/ γ -Al₂O₃ than on MoS₂/ γ -Al₂O₃ catalyst in the absence and the presence of DBT. DBT only promoted further DHQ conversion in the case of NiMoS/ γ -Al₂O₃ catalyst (DHQ yield exhibits maximum of 30% at the space time of 230 h·g_{cat}/mol).

The rate of the ring opening in 14THQ via the C(sp³)-N bond cleavage, leading to OPA formation, was twice higher on NiMoS/ γ -Al₂O₃ comparing to MoS₂/ γ -Al₂O₃ catalyst only in the presence of DBT, Fig. 16 (D). PCHA, the product of the C(sp³)-N bond cleavage in DHQ, was observed only when the reaction was carried out on the promoted NiMoS/ γ -Al₂O₃ catalyst in the presence of DBT. The formation rate of all nitrogen-free products was higher on the Ni promoted catalyst, especially in the presence of DBT, Fig. 17. Indeed, the rate of formation of these products was affected by the presence of DBT only on the promoted catalysts.

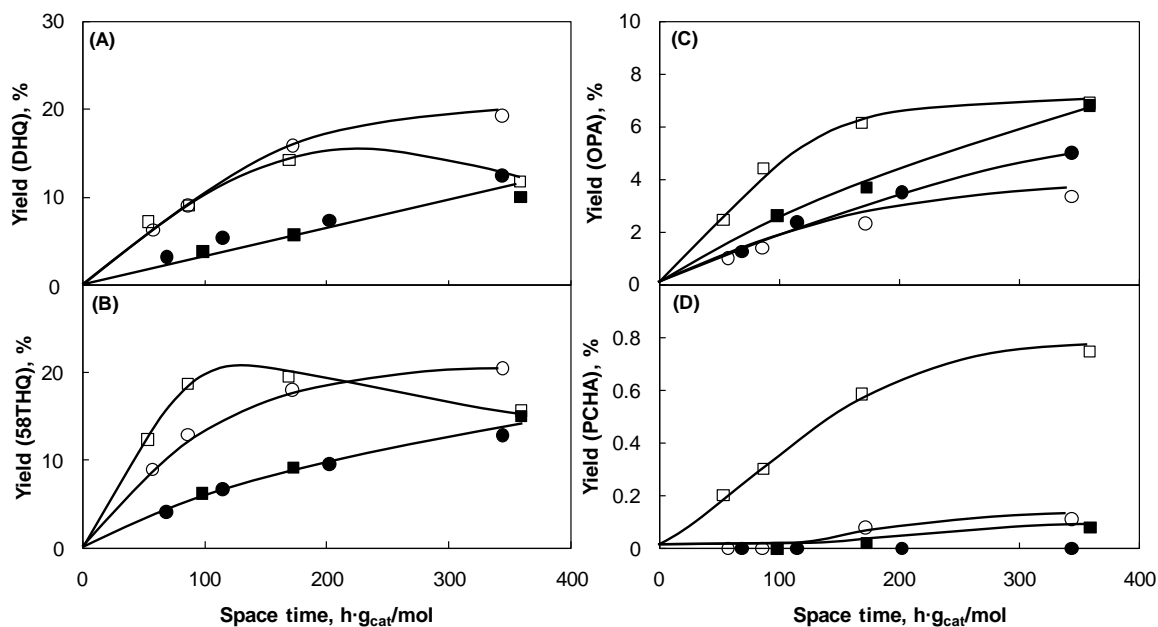


Figure 16. Yield of decahydroquinoline (A), 5,6,7,8-tetrahydroquinoline (B), o-propylaniline (C), and propylcyclohexylamine (D) as a function of space time in quinoline HDN carried out on MoS₂/ γ -Al₂O₃ (●,■) and NiMoS/ γ -Al₂O₃ (○,□) catalyst. The experiments were carried out in the absence (●,○) and presence of 3.4 kPa DBT (■,□).

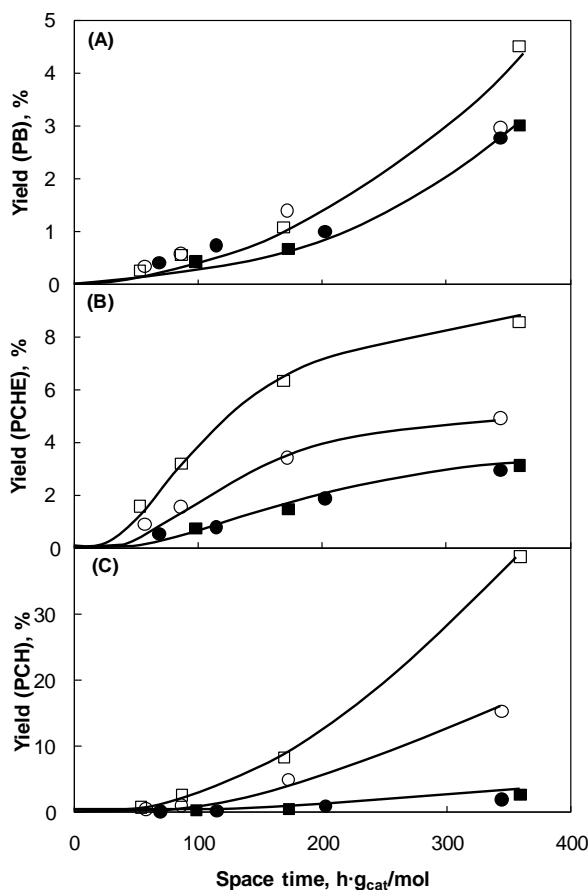


Figure 17. Yield of propylbenzene (A), propylcyclohexene (B), and propylcyclohexane (C) as a function of space time in quinoline HDN carried out on MoS₂/γ-Al₂O₃ (●,■) and NiMoS/γ-Al₂O₃ (○,□) catalyst. The experiments were carried out in the absence (●,○) and presence of 3.4 kPa DBT (■,□).

4. Discussion

4.1. Reaction pathway of quinoline and DHQ HDN

During HDN experiments using either quinoline or DHQ as starting reactants, the equilibrium between quinoline and 14THQ is rapidly established (82 mol% 14THQ : 18 mol% quinoline). The HDN conversion of DHQ is the first order reaction, as shown in Fig 18. In the case of quinoline, the HDN conversion is at first negligible, due to the inhibition by the partially hydrogenated intermediate, 14THQ, because it is adsorbed stronger on the catalyst surface than quinoline [28]. When significant amount of 14THQ have been converted to DHQ, at about 100 h·g_{cat}/mol the quinoline HDN rate increases. In principle, after establishing the quinoline-14THQ equilibrium two pathways are possible, i.e., the ring opening to form OPA and the hydrogenation to form DHQ, Fig. 19.

The lower concentration of OPA than DHQ, over the whole space time, indicates that the ring opening of 14THQ via C(sp³)-N bond cleavage has a lower reaction rate compared to the parallel hydrogenation of the benzoic ring to form DHQ. It is important to note that the

low concentration of OPA cannot be attributed to the fast transformation to PCHA, as long as quinoline, 14THQ, 58THQ and DHQ are present, because their strong adsorption would limit the access of OPA [15,29]. Therefore, the hydrogenation of the phenyl ring in OPA is considered to be the rate determining step in the sequence quinoline → 14THQ → OPA → PCHA. Further conversion of OPA can also proceed via the DDN route, leading to PB formation. However, the DDN of OPA was found to be suppressed by the Ni addition and the presence of DBT [14]. Thus, the positive effect of Ni and DBT on the yield of PB found in this work must be attributed to the enhancement of the PCHE dehydrogenation. Having established that the further 14THQ conversion via OPA is very slow, the main pathway for the nitrogen removal from quinoline, thus, will proceed via DHQ intermediate and subsequent ring opening and denitrogenation.

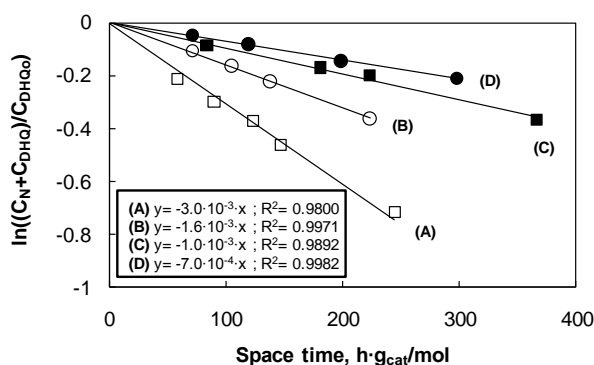


Figure 18. The first order kinetic for the nitrogen removal from DHQ, where C_N is the concentration of all nitrogen containing compounds at the given space time, C_{DHQ} is the concentration of DHQ at the given space time, and C_{DHQ0} is the initial concentration of DHQ.

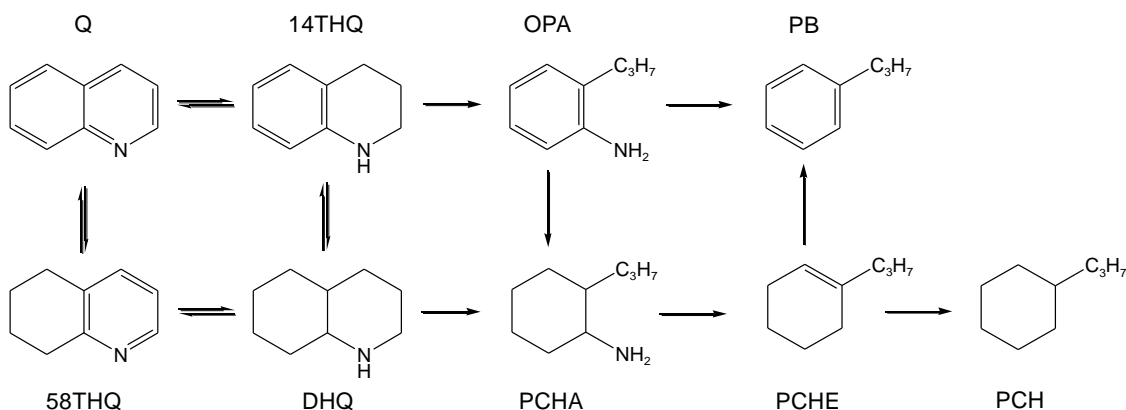


Figure 19. HDN reaction network of quinoline (Q), where following abbreviations are defined as follows:
 14THQ - 1,2,3,4-tetrahydroquinoline PCHA - propylcyclohexylamine
 58THQ - 5,6,7,8-tetrahydroquinoline PB - propylbenzene
 DHQ - decahydroquinoline PCHE - propylcyclohexene
 OPA - o-propylaniline PCH - propylcyclohexane.

The HDN of DHQ and quinoline occurs through parallel dehydrogenation and hydrogenation, respectively and ring opening reactions, under all studied conditions on $MoS_2/\gamma-Al_2O_3$ and

NiMoS/ γ -Al₂O₃ catalysts as shown in, Figure 19. Starting from DHQ, the dehydrogenation of the carbocyclic ring in DHQ leads to the fast formation of 58THQ and the dehydrogenation of the nitrogen-containing ring leads to a very slow formation of 14THQ which is immediately equilibrated with quinoline. The relative reaction rates can be deduced from the corresponding yields, Figure 10 A and B. In parallel, the HDN of DHQ proceeds via the sequence DHQ → PCHA (via ring opening) → PCHE (via denitrogenation) → PCH (via hydrogenation). Starting from quinoline, the quinoline-14THQ equilibrium is followed by hydrogenation to 58THQ and DHQ or ring opening to OPA. The later step is the least favored.

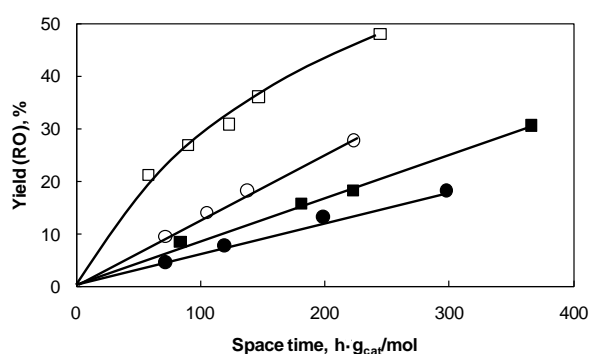


Figure 20. The yield of the ring opening (RO) route (PCHA + PCHE + PCH) in the DHQ HDN carried out on MoS₂/γ-Al₂O₃ (●,■) and NiMoS/γ-Al₂O₃ (○,□) catalyst in absence of DBT (●,○) and in presence of 3.4 kPa DBT (■,□).

DBT promotes the rate of PCHE and PCH formation on both catalysts in the DHQ ring opening sequence (50% on MoS₂/γ-Al₂O₃ and 2.5 times on NiMoS/γ-Al₂O₃, see Fig. 20). This is in contrast with a previous study on the HDN of OPA showing that DBT did not influence the hydrogenation of the OPA phenyl ring and the further C(sp³)-N bond cleavage to PCHE on MoS₂/γ-Al₂O₃, but promoted the same steps on the NiMoS/γ-Al₂O₃ [14]. Therefore, the increase of PCHE and PCH (by further PCHE hydrogenation) yield is a direct consequence of the DBT promotion on the DHQ ring opening via C(sp³)-N bond cleavage. The rate of PCHA formation (detected only in very low concentrations) is lower than the further conversion to PCHE, see Figs. 16 (D) and 17 (B). Hence, the C(sp³)-N bond cleavage in the primary amine (PCHA) is concluded to be fast and the rate of the C(sp³)-N bond cleavage in DHQ is the rate limiting step [30].

4.2. The active sites and mechanism for the ring opening via C(sp³)-N bond cleavage

While the HDN of quinoline on MoS₂-based catalysts has been studied for decades, surprisingly there is not a general agreement about the interaction between the reactants and the potential active sites in the surface of the catalyst. It is widely accepted that the

active sites for the removal of heteroatoms are coordinatively unsaturated sites [19,31], i.e., Mo atoms with an incomplete coordination at the perimeter of the MoS₂ slabs. Recent scanning tunneling microscopy (STM) studies showed the presence of an electron-rich region on the fully sulfide edge of the MoS₂ slabs [20,21]. The interaction of this electron-rich region with nitrogen-containing compounds explains several experimental observations regarding the competitive HDS and HDN reactions. The SH groups, formed after the activation of H₂ or H₂S, are proposed as hydrogen providing sites, but rarely as sorption sites for the reactants. Let us now discuss the elementary steps of the HDN of quinoline with all the above features of the sulfide surface.

The first issue that must be addressed is whether the C(sp³)-N bond cleavage occurs via S_N2 nucleophilic substitution of one bond in the -NH- bridge by an -SH group followed by the further C(sp³)-S bond cleavage, or directly via Hofmann-type elimination. The S_N2 substitution, with the consequent formation of thiols has been confirmed in the HDN of n-hexylamines carried out at relatively low temperatures (270-320 °C) and pressure (3 MPa) and with high H₂S partial pressure (10-100 kPa) [32-37]. The Hofmann-type elimination has been considered as the main mechanism in the HDN of cyclohexylamine and aniline-type compounds, carried out at high temperature (350-370 °C) and pressure (3-5 MPa) and with H₂S partial pressure up to 17.5 kPa [38-41]. Relatively high reaction temperature and pressure (370 °C, 5 MPa) and low DBT concentration at which the HDN was carried out in this study and the notable absence of thiols allow us to conclude that the ring opening in 14THQ and DHQ follows a Hofmann-type elimination of the aliphatic C(sp³)-N bond under the chosen operating conditions.

The Hofmann-type elimination mechanism requires that the leaving nitrogen is quaternized before the C(sp³)-N bond is cleaved by the removal of a β-H atom. Thus, a site with an acidic and a basic functionality is required. The polar surface of the MoS₂-based catalysts offers several possibilities of such sites. However, the detailed analysis of the effect of Ni on the ring opening reactions in presence and absence of DBT can be used to elucidate the acid and base sites that are taking part in the Hofmann-type elimination.

If the CUS, as electron withdrawing sites, are active for the ring opening of DHQ, one would expect 25 % increase in the rate by addition of nickel, which corresponds to the increase in the concentration of exposed cations, determined by NO adsorption. Instead, the rate of C(sp³)-N bond cleavage in DHQ was much higher on NiMoS/γ-Al₂O₃ than on MoS₂/γ-Al₂O₃, twice in the absence and 3.5 times in the presence of DBT, Figure 20. One may argue that the intrinsic activity of CUS increases as well with promotion. However, if one assumes that CUS are the active sites for the C(sp³)-N bond cleavage, a negative effect of the presence of

DBT may be anticipated instead of the promoting effect, which is experimentally observed. Recall that DBT is mainly converted to biphenyl (DDS route) via σ -adsorption on the CUS [17], which has to lead to a decrease in concentration of the available CUS during reaction due to their replacement by sulfur removed from DBT.

A promoting effect by DBT was observed as well in the 14THQ ring opening, i.e., the rate was slightly enhanced on MoS₂/ γ -Al₂O₃, while a much more pronounced effect was observed on with NiMoS/ γ -Al₂O₃. Therefore, we conclude that CUS are not the active sites for the C(sp³)-N bond cleavage in the ring opening reactions.

Furthermore, the increase of the ring opening rate by adding DBT implies that the active sites are created either by the presence of DBT or the products of the HDS of DBT. Note for instance, that much higher rate of C(sp³)-N bond cleavage on NiMoS/ γ -Al₂O₃ than on MoS₂/ γ -Al₂O₃ in the presence of DBT can be related to the much more efficient sulfur removal on the first catalyst. Thus we propose that the direct desulfurization of DBT stabilizes the sulfide surface converting the inactive CUS into S²⁻ ions with a key activity in the ring opening reaction.

Evidently, the S²⁻ ions can act as basic sites; furthermore, they are precursors for the sites with acid character that complement the dual sites needed for the ring opening via the Hofmann type elimination mechanism. We postulate that these sites are -SH groups where the nitrogen of 14THQ or DHQ is quaternized. The -SH groups are formed on the edges of the MoS₂ or NiMoS slabs nearby the brim sites after the reaction of hydrogen with S²⁻ ions [42]. Additional indication that basic nitrogen-containing compounds, e.g. acridine, quinoline, pyridine, aniline, adsorb on Brønsted sites rather than on Lewis acid sites is the linear correlation observed between the adsorption constant and the proton affinity [43]. Nickel eases the hydrogen dissociation that transfer via spillover to the sulfide edges and increase the concentration of -SH groups. Furthermore, nickel increases the sulfur electron density hence the basicity of the S²⁻ ions [22]. These facts explain satisfactorily the synergetic effect of Ni and DBT in the rate of ring opening reactions.

The overall mechanism for the Hofmann type elimination is shown in Fig. 21. The fully sulfided edge of the MoS₂ or NiMoS slabs react with hydrogen to form -SH groups or CUS. The proton of the -SH group can adsorb the DHQ molecule via the quaternization of the nitrogen atom. Then the β -hydrogen abstraction by the S²⁻ ion starts the concerted E2 mechanism that leads to the C(sp³)-N bond cleavage and the desorption of a molecule with an amino group. The role of DBT is to donate sulfur to the CUS via DDS increasing the concentration of S²⁻ ions.

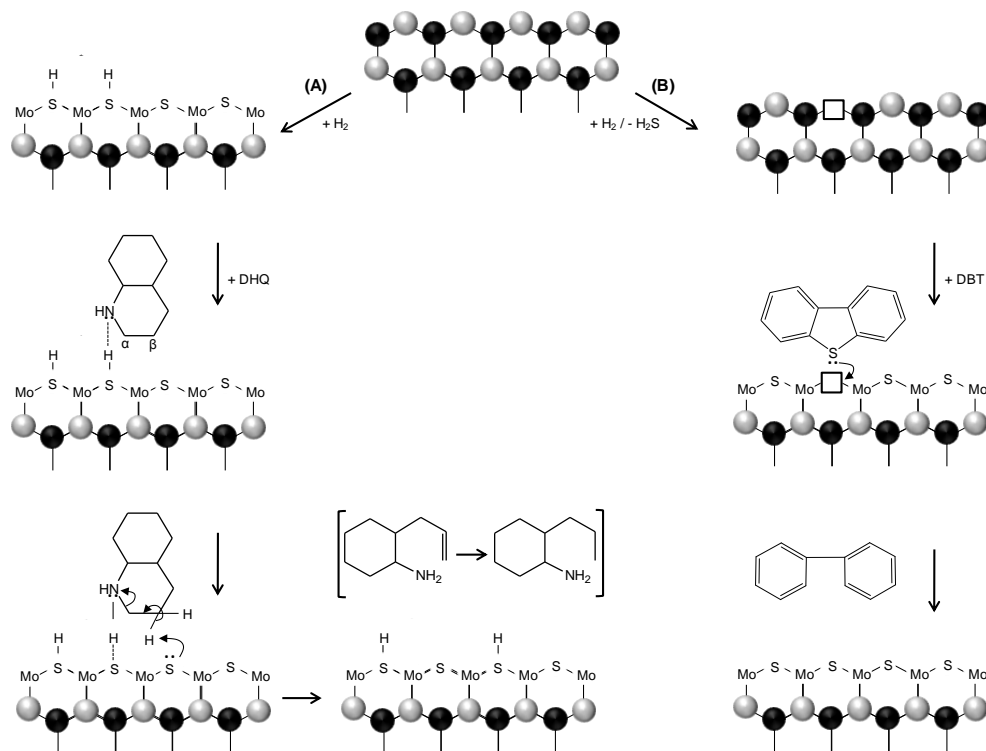


Figure 21. (A) The Hofmann elimination type mechanism proposed for the C(sp³)-N bond cleavage in the ring opening of DHQ. Illustrative presentation is given for the Brønsted acidic -SH groups, necessary for the adsorption and protonation, and basic S²⁻ groups, necessary for the β-H elimination. (B) Generation of the CUS via surface reduction with H₂ and formation of stable sulfur ions at the edges of the sulfide slabs by DBT conversion.

Several theoretical and experimental studies have postulated that molecular hydrogen dissociates on (S-S)²⁻ dimers leading to the formation of -SH groups. The dual sites formed by CUS and S²⁻ ions would also be active for the homolytic dissociation of H₂ to form a hydride and an -SH group. The H₂S can also dissociate into two -SH groups on the CUS and S²⁻ sites [44-48]. The presence of -SH groups in the MoS₂/Al₂O₃ and NiMoS/Al₂O₃ catalyst cannot be directly evidenced, but inferred. For instance, the TPD results shown in Fig. 1 indicate that the sulfided catalysts release not only physisorbed H₂S, but also H₂S product of the -SH groups recombination on the surface. Surprisingly, Ni did not exert the marked effect on the H₂S desorption though one may have expected that Ni weakens the metal-sulfur bond strength [18,49,50]. In contrast, Ni has an important effect on the H₂ desorption as shown in Fig. 2. Note that the intensity of the hydrogen release signal below 300 °C decreases with the addition of Ni, while the intensity of the peak at higher temperature increases. Accepting that hydrogen is adsorbed on the surface forming -SH groups, the H₂ desorption in that wide temperature range suggests the presence of -SH groups with different reactivity. Some authors have suggested that the -SH groups at the edges are more reactive, thus, the release of H₂ at low temperature is assigned to the recombination of H₂ at the edges of the slabs, whereas the high temperature H₂ release is attributed to the

recombination of H₂ on the basal plane [51]. This is well in line with the idea of a hydrogen spillover from the edge sites to the basal planes of MoS₂. Easier dissociation at the edges is observed in presence of Ni [46].

Although studying the origin of the impact of Ni on the TPD results is not in the scope of this work, we postulate that the presence of a promoter increases the H₂ mobility. On the other hand, the S-metal bond weakening is evident only in the presence of H₂, as driving force for the sulfur removal, as shown by the shift to low temperatures in the H₂S peak (Fig. 3) attributed to the reduction of the sulfide surface. However, this shift can also be associated to more efficient hydrogen dissociation in presence of Ni.

As a final note concerning the reaction mechanism postulated in Fig. 21, we attribute the lower rate of ring opening in 14THQ than in DHQ to the presence of the aromatic ring. The interaction of the free electron pair of the nitrogen in 14THQ with the benzoic ring increases the stability of the molecule. Conversely, the free electron pair of the nitrogen in DHQ is more able to interact with the proton from -SH groups to form quaternized nitrogen atoms.

Turning now to the rest of the HDN reaction steps, it has been observed that the PCHE hydrogenation to PCH was promoted by Ni. Furthermore, DBT did not affect the rate of this step on the unpromoted MoS₂/γ-Al₂O₃, while on the NiMoS/γ-Al₂O₃ catalyst the presence of DBT increased the rate of PCHE hydrogenation significantly. This faster rate is related to the presence of Ni, which facilitates the dissociative hydrogen adsorption, and a higher electron density at the brim sites that increases the rate of hydrogenation. The presence of sulfur-containing molecules (DBT or H₂S), which act as electron pair donors, increases the electron density or extends the electron rich metallic-like zone in the sulfide catalysts. This conclusion agrees well with the previous study of OPA HDN, in which it was proposed that the hydrogenation occurs on the brim sites [14]. Also note that the OPA conversion via phenyl ring hydrogenation was ruled out in the presence of quinoline 14THQ, 58THQ and DHQ, implying that these molecules adsorb competitively on the brim sites. However, the conversion of OPA occurred via the direct denitrogenation (DDN) by σ-bonding of the amine nitrogen on the accessible Mo cations as indicated by the negative effect of DBT (that also adsorbs on CUS) on the formation of PB on MoS₂/γ-Al₂O₃.

5. Conclusion

The parallel study of quinoline and DHQ HDN allows to establish the C(sp³)-N bond cleavage in the ring opening reactions as one of the crucial steps in the overall HDN mechanism. The two main routes examined, i.e., DHQ → PCHA → PCHE → PCH and quinoline → 14THQ → OPA → PCHA and PB, showed two different limiting steps in the

overall HDN reaction. In the first route the rate limiting step is the ring opening via C(sp³)-N bond cleavage, while in the later the rate limiting step is the hydrogenation of OPA. Comparing the ring opening reaction of 14THQ and DHQ, it is concluded that the intrinsic rate is lower for the 14THQ than for the DHQ, because of the stabilization of the nitrogen free electron pair with the electrons of the benzoic ring of 14THQ. The nitrogen free electron pair in DHQ facilitates the formation of the quaternized nitrogen atom, which is the leaving group in the Hofmann type mechanism, proposed for the C(sp³)-N bond cleavage.

The dual site, needed for the Hofmann type elimination mechanism, comprises of -SH groups with acidic character close to the brim sites of the MoS₂ or NiMoS slabs (formed on S²⁻ dimers by reacting with hydrogen), and basic S²⁻ ions. DHQ and 14THQ adsorption involves the interaction of the -NH- fragment with -SH groups. It is proposed that DBT stabilizes the sulfide surface converting the CUS (inactive for the ring opening) into the basic S²⁻ ions active for the formation of the -SH groups. Nickel as a promoter facilitates H₂ dissociation and its mobility on the sulfide surface, providing more active -SH groups. On the other hand nickel increases the basicity of the S²⁻ ions, increasing the sulfur electron density and hence facilitates the β-H atom removal.

6. Acknowledgements

This work was supported by Chevron Energy Technology Company. The authors would like to thank Dr. Alexander Kuperman and Dr. Axel Brait for fruitful discussions.

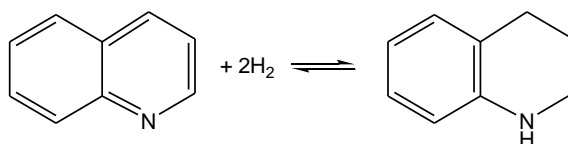
7. Supplementary material

7.1. Calculation of equilibrium constants at T= 370 °C and p= 5 MPa

Reaction	log ₁₀ K _p at T [°C]	
	300	400
Quinoline + 2H ₂ ↔ 1,2,3,4-Tetrahydroquinoline	-1.4	-3.2
Quinoline + 2H ₂ ↔ 5,6,7,8-Tetrahydroquinoline	-0.7	-3.0
1,2,3,4-Tetrahydroquinoline + 3H ₂ ↔ Decahydroquinoline	-2.8	-5.4
5,6,7,8-Tetrahydroquinoline + 3H ₂ ↔ Decahydroquinoline	-3.5	-5.6

Table 1. Equilibrium constants for HDN reactions [52].

7.1.1. Quinoline and 1,2,3,4-Tetrahydroquinoline (14THQ)

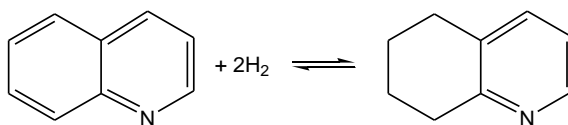


$$\log K_p(370^\circ\text{C}) = -2.7$$

$$K_p = 2 \cdot 10^{-3}$$

$$K_p = \frac{[14\text{THQ}]}{[\text{Q}] \cdot p_{\text{H}_2}^2} \quad \rightarrow \quad K'_{5.0} = \frac{[14\text{THQ}]}{[\text{Q}]} = K_p \cdot 50^2 = 5$$

7.1.2. Quinoline and 5,6,7,8-Tetrahydroquinoline (58THQ)

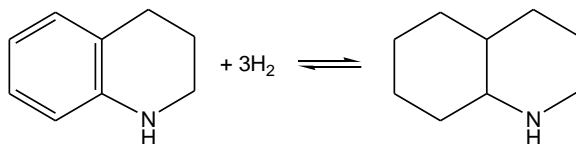


$$\log K_p(370^\circ\text{C}) = -2.3$$

$$K_p = 5 \cdot 10^{-3}$$

$$K_p = \frac{[58\text{THQ}]}{[\text{Q}] \cdot p_{\text{H}_2}^2} \quad \rightarrow \quad K'_{5.0} = \frac{[58\text{THQ}]}{[\text{Q}]} = K_p \cdot 50^2 = 12$$

7.1.3. 1,2,3,4-Tetrahydroquinoline (14THQ) and Decahydroquinoline (DHQ)

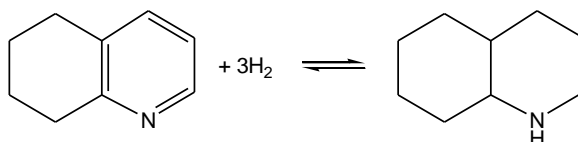


$$\log K_p(370^\circ\text{C}) = -4.6$$

$$K_p = 2.5 \cdot 10^{-5}$$

$$K_p = \frac{[\text{DHQ}]}{[\text{14THQ}] \cdot p_{\text{H}_2}^3} \rightarrow K'_{5.0} = \frac{[\text{DHQ}]}{[\text{14THQ}]} = K_p \cdot 50^3 = 3.1$$

7.1.4. 5,6,7,8-Tetrahydroquinoline (58THQ) and Decahydroquinoline (DHQ)



$$\log K_p(370^\circ\text{C}) = -5$$

$$K_p = 1 \cdot 10^{-5}$$

$$K_p = \frac{[\text{DHQ}]}{[\text{58THQ}] \cdot p_{\text{H}_2}^3} \rightarrow K'_{5.0} = \frac{[\text{DHQ}]}{[\text{58THQ}]} = K_p \cdot 50^3 = 1.2$$

8. References

- [1] H. Topsøe, B.S. Clausen, F.E. Massoth, *Hydrotreating Catalysis, Science and Technology*, Springer, New York, (1991).
- [2] R. Prins, in "Handbook of Heterogeneous Catalysis" (G. Ertl, H. Knözinger, and J. Weitkamp, Eds.), Vol. 4, VCH, Berlin, 1997.
- [3] T.C. Ho, *Catal. Rev. Sci. Eng.* 30 (1988) 117.
- [4] S.H. Yang, C.N. Satterfield, *J. Catal.* 81 (1983) 168.
- [5] H.A. Rangwala, I.G. Dalla Lana, F.D. Otto, H. Yeniova, K. Al-Nuaimi, *Energ. Fuel.* 4 (1990) 599.
- [6] S. Eijsbouts, C. Sudhakar, V.H.J. de Beer, R. Prins, *J. Catal.* 127 (1991) 605.
- [7] S. Eijsbouts, V.H.J. de Beer, R. Prins, *J. Catal.* 127 (1991) 619.
- [8] R. Prins, M. Jian, M. Flechsenhar, *Polyhedron* 16 (1997) 3235.
- [9] R.Z. Lee, M. Zhang, F.T.T. Ng, *Top. Catal.* 37 (2006) 121.
- [10] J. Ancheyta, J.G. Speight, *Hydroprocessing of Heavy Oils and Residua*, Taylor & Francis, (2007).
- [11] J.F. Cocchetto, C.N. Satterfield, *Ind. Eng. Chem. Process Des. Dev.* 20 (1981) 49.
- [12] C.N. Satterfield, S. Gultekin, *Ind. Eng. Chem. Process Des. Dev.* 20 (1981) 62.
- [13] S.H. Yang, C.N. Satterfield, *Ind. Eng. Chem. Process Des. Dev.* 23 (1984) 20.
- [14] M. Jian, R. Prins, *Catal. Lett.* 50 (1998) 9.
- [15] P. Afanasiev, *J. Catal.* 269 (2010) 269.
- [16] A. Hrabar, J. Hein, O.Y. Gutiérrez, J.A. Lercher, *J. Catal.* In Press, Available online 17 June 2011.
- [17] F. Besenbacher, M. Brorson, B.S. Clausen, S. Helveg, B. Hinnemann, J. Kibsgaard, J.V. Lauritsen, P.G. Moses, J.K. Nørskov, H. Topsøe, *Catal. Today* 130 (2008) 86.
- [18] L.S. Byskov, J.K. Nørskov, B.S. Clausen, H. Topsøe, Sulphur bonding in transition metal sulphides and MoS₂ based structures, in T. Weber, R. Prins, R.A. van Santen (eds.), *Transition Metal Sulphides - Chemistry and Catalysis*, Kluwer Academic Publishers, (1998).
- [19] M. Sun, J. Adjaye, A.E. Nelson, *Appl. Catal. A* 263 (2004) 131.
- [20] H. Topsøe, *Appl. Catal. A* 322 (2007) 8.
- [21] J. Kibsgaard, A. Tuxen, K.G. Knudsen, M. Brorson, H. Topsøe, E. Laegsgaard, J.V. Lauritsen, F. Besenbacher, *J. Catal.* 272 (2010) 195.
- [22] T.C. Ho, L. Qiao, *J. Catal.* 269 (2010) 291.
- [23] I.E Wachs, *Catal. Today* 27 (1996) 437.
- [24] N.-Y. Topsøe, H. Topsøe, *Bull. Soc. Chim. Belg.* 90 (1981) 1311.
- [25] N.-Y. Topsøe, H. Topsøe, *J. Catal.* 75 (1982) 354.

- [26] F. Mauge, J. Lamotte, N.S. Nesterenko, O. Manoilova, A.A. Tsyganenko, *Catal. Today* 70 (2001) 271.
- [27] L.P. Nielsen, S.V. Christensen, H. Topsøe, B.S. Clausen, *Catal. Lett.* 67 (2000) 81.
- [28] T. Ho, *Appl. Catal. A* 378 (2010) 52.
- [29] G. Perot, *Catal. Today* 10 (1991) 447.
- [30] M. Jian, R. Prins, *Ind. Eng. Chem. Res.* 37 (1998) 834.
- [31] C. Moreau, J. Joffre, C. Saenz, P. Geneste, *J. Catal.* 122 (1990) 448.
- [32] F. Rota, R. Prins, *Top. Catal.* 11/12 (2000) 327.
- [33] L. Qu, R. Prins, *Appl. Catal. A* 250 (2003) 105.
- [34] Y. Zhao, P. Kukula, R. Prins, *J. Catal.* 221 (2004) 441.
- [35] Y. Zhao, R. Prins, *J. Catal.* 229 (2005) 213.
- [36] R. Prins, Y. Zhao, N. Sivasankar, P. Kukula, *J. Catal.* 234 (2005) 509.
- [37] R. Prins, M. Egorova, A. Röthlisberger, Y. Zhao, N. Sivasankar, P. Kukula, *Catal. Today* 111 (2006) 84.
- [38] M. Sun, R. Prins, *J. Catal.* 201 (2001) 138.
- [39] L. Qu, R. Prins, *J. Catal.* 210 (2002) 183.
- [40] P. Clark, X. Wang, P. Deck, S.T. Oyama, *J. Catal.* 210 (2002) 116.
- [41] L. Qu, M. Flechsenhar, R. Prins, *J. Catal.* 217 (2003) 284.
- [42] J.V. Lauritsen, M. Nyberg, J.K. Nørskov, B.S. Clausen, H. Topsøe, E. Laegsgaard, F. Besenbacher, *J. Catal.* 224 (2004) 94.
- [43] M. Nagai, T. Sato, A. Aiba, *J. Catal.* 97 (1986) 52.
- [44] M. Breyse, E. Furimsky, S. Kasztelan, M. Lacroix, G. Perot, *Catal. Rev.* 44 (2002) 651.
- [45] J. Polz, H. Zeilinger, B. Muller, H. Knozinger, *J. Catal.* 120 (1989) 22.
- [46] A.B. Anderson, Z.Y. Al-Saigh, W.K. Hall, *J. Phys. Chem.* 92 (1988) 803.
- [47] P. Raybaud, J. Hafner, G. Kresse, S. Kasztelan, H. Toulhoat, *J. Catal.* 190 (2000) 128.
- [48] M. Sun, A.E. Nelson, J. Adjaye, *Catal. Today* 105 (2005) 36.
- [49] L.S. Byskov, B. Hammer, J.K. Nørskov, B.S. Clausen, H. Topsøe, *Catal. Lett.* 47 (1997) 177.
- [50] L.S. Byskov, J.K. Nørskov, B.S. Clausen, H. Topsøe, *J. Catal.* 187 (1999) 109.
- [51] X.S. Li, Q. Xin, X.X. Guo, P. Grange, B. Delmon, *J. Catal.* 137 (1992) 385.
- [52] J. Ancheyta, J.G. Speight, *Hydroprocessing of Heavy Oils and Residua*, Taylor & Francis, (2007), p 64.

Chapter 4

Characterization and performance of γ -Al₂O₃ supported Mo and NiMo and novel unsupported NiMo catalysts in the HDN of quinoline

A series of catalyst, i.e., supported Mo/ γ -Al₂O₃, NiMo/ γ -Al₂O₃ and unsupported NiMo, were synthesized and tested in the quinoline hydrodenitrogenation (HDN). The oxide precursors and the corresponding sulfide catalysts were extensively characterized by X-ray diffraction, NO-adsorption, transmission electron microscopy, temperature programmed sulfidation and X-ray absorption, Raman and DR-UV-vis spectroscopy. The supported oxide catalyst precursors exhibited well dispersed amorphous polymolybdate structure that led to a formation of high dispersed sulfide phase with the average MoS₂ stacking degree of two and slabs length below 10 nm. On the contrary, NiMo/unsupported precursor exhibited a mixture of nickel molybdate and an ammonium nickel molybdate crystalline phase that formed multi-stacked sulfide slabs. The main route for the nitrogen removal in the quinoline HDN is: quinoline → 1,2,3,4-tetrahydroquinoline → decahydroquinoline → propylcyclohexylamine → propylcyclohexene → propylcyclohexane. The HDN activity increased in the following order: MoS₂/ γ -Al₂O₃ < NiMoS/unsupported < NiMoS/ γ -Al₂O₃. Multi-stacked NiMoS/unsupported catalyst exhibited lower hydrogenation and ring opening rate than the supported NiMoS/ γ -Al₂O₃ counterpart. Higher catalyst dispersion, i.e., lower stacking degree was concluded to be the key factor responsible for the high HDN activity.

1. Introduction

There is a continuously increasing need for improving the efficiency of the crude oil utilization. This has imposed further studying of sulfide-based catalysts used for hydrotreating processes such as hydrodesulfurization (HDS), hydrodenitrogenation (HDN), hydrodemetallation (HDM) and hydrodeoxygenation (HDO). These hydrotreating processes are applied for the removal of heteroatoms and metals from crude oil in order to reach environmentally acceptable products and to improve their quality.

Typically used materials in hydrotreating reactions are based on nickel- or cobalt-promoted transition metal sulfides (TMS), e.g., MoS_2 unsupported or supported, usually on a high surface $\gamma\text{-Al}_2\text{O}_3$, because of its good textural and mechanical properties [1,2]. Molybdenum in MoS_2 is coordinated to trigonal sulfur prisms, which are two-dimensionally bound, forming S-Mo-S sandwiched structures exhibiting two different active edges, so-called Mo-edge and S-edge. These S-Mo-S layers are weakly held together by van-der Waals interactions along the c-axis. The stacking degree depends on the synthesis conditions, metal loading or surface area of used support material.

The sulfide surface exhibits a series of potential active sites for hydrotreating processes. The coordinatively unsaturated sites (CUS) are exposed Mo cations that act as electron acceptors, thus as adsorption sites for Lewis acids as S and N atoms. On the other hand, the SH groups, formed after H_2 dissociation exhibit an acidic character and provide hydrogen for hydrogenolysis and hydrogenation reactions. Furthermore, Topsøe et al. proposed existence of the electron rich brim sites, located nearby the edge of the basal top plane [3]. The brim sites have the ability to donate as well as to accept the electrons; therefore, they catalytically act as an ordinary metal surface active in hydrogenation [4].

Numerous studies have been carried out to correlate the catalyst structure and the activity in the HDS reactions. The “rim-edge” model was first proposed by Daage and Chianelli to describe the differences in the HDS activity of S-Mo-S layers (stacks) depending on their position in the sulfide slab. The top and bottom S-Mo-S layers are so-called “rim sites” while the others between them are so-called “edge sites”, therefore the relative concentration of types of sites is stacking dependent. A “rim-edge” model is used to correlate the catalyst selectivity for hydrogenation (HYD) versus direct desulfurization (DDS) in HDS reactions. It was found that the rim sites are mainly responsible for the HYD route, while the edge sites catalyze the DDS route via C-S hydrogenolysis [5]. On the contrary attempts to correlate catalyst structure and activity have not been made for the HDN reactions. Therefore this study is systematically performed to bring more insight on the physicochemical properties and molecular structure of a series of supported $\text{Mo}/\gamma\text{-Al}_2\text{O}_3$, $\text{NiMo}/\gamma\text{-Al}_2\text{O}_3$, and novel

unsupported NiMo catalysts. Correlation is made to the catalyst activity and selectivity in quinoline HDN carried out in the presence of dibenzothiophene (DBT).

In the present study it has been shown that the multi-stacked unsupported NiMo catalyst exhibited lower hydrogenation and ring opening rate than the well dispersed supported counterparts. Higher catalyst dispersion, i.e., lower stacking degree was concluded to be the key factor responsible for the higher HDN activity. On the other hand HDS activity was influenced by a combination of factors, i.e., concentration of coordinatively unsaturated sites (CUS), and regeneration of the sites.

2. Experimental

2.1. Catalyst preparation

The supported Mo and NiMo oxide catalyst precursors were prepared by two steps incipient wetness impregnation of γ -Al₂O₃ (Chevron) with the specific surface area of 237 m²/g. Prior to impregnation, the support was dried at 120 °C in static air atmosphere and then calcined at 560 °C for 2 hours in synthetic air flow. In the first step molybdenum was impregnated using an aqueous solution of ammonium heptamolybdate, (NH₄)₆Mo₇O₂₄·4H₂O (Aldrich). After impregnation, the catalyst was dried overnight at 120 °C in static air atmosphere and then calcined at 500 °C for 4 hours (heating rate 1 °C/min) in synthetic air flow [6]. One part of the prepared sample was preserved as Mo oxidic catalyst precursor and the other was used as a support for further nickel impregnation. The molybdenum concentration in both prepared samples was constant, 8.6 wt.% (2.5 atom/nm²). As a promoter, 3.6 wt.% of nickel was impregnated using an aqueous solution of nickel nitrate, Ni(NO₃)₂·6H₂O (Aldrich) [7]. After impregnation, the NiMo/ γ -Al₂O₃ catalyst was thermally treated as in the case of Mo/ γ -Al₂O₃ catalyst, described previously.

The unsupported NiMo oxide catalyst precursor was prepared by coprecipitation [8]. Ammonium heptamolybdate (NH₄)₆Mo₇O₂₄·4H₂O (Aldrich) was dissolved in bidistilled water at room temperature in a three neck flask with condenser (pH= 5.5). With continuous stirring, NH₄OH (28-30%) was added until the pH value increased to 9.5. The resulting molybdenum solution was heated to 90 °C. In parallel, aqueous solution of nickel nitrate Ni(NO₃)₂·6H₂O (Aldrich) was heated to 60 °C (pH= 6) and then added dropwise to the hot molybdenum solution. The light green precipitate, formed at pH= 7 was further stirred and then filtered. Subsequently, the filter cake was dispersed into maleic acid solution (0.05 mol/l, pH= 1.5) to form a slurry (pH= 6). After the filtration, collected precipitate was vacuum dried overnight at room temperature. Finally, the catalyst precursor was further dried at 120 °C for 12 h (heating rate of 1 °C/min) in synthetic air flow. The product was a fine green powder.

Hereafter, the oxidic precursors are referred as: Mo/ γ -Al₂O₃, NiMo/ γ -Al₂O₃ and NiMo/unsupported, whereas the sulfide catalysts are denoted as: MoS₂/ γ -Al₂O₃, NiMoS/ γ -Al₂O₃ and NiMoS/unsupported.

2.2. Catalyst characterization

Physicochemical properties of the catalyst. The BET surface area and pore size distribution were determined by N₂ adsorption-desorption at -196 °C using a PMI Automated BET Sorptomatic 1900 Series instrument. Prior to the adsorption, the samples were evacuated at 250 °C for 2 h. Elemental analysis was carried out by the Microanalytical Laboratory at the TU München.

NO adsorption. NO adsorption was performed as a flow pulse experiment at room temperature to probe the number of active sites and average edge dispersion in studied metal sulfide catalysts. A detailed description of the experiment can be found elsewhere [9].

X-ray diffraction (XRD). The crystal structure of the catalysts was determined by powder X-ray diffraction. XRD patterns were collected with a Philips X'Pert System (Cu-K α radiation, 0.1542 nm), using a nickel K β -filter and a solid state detector (X'Celerator). The operating conditions were 45 kV/40 mA. The measurements were carried out in the range from 5° to 70° 2 θ . The prepared catalysts were measured with step size of 0.017° and scan time of 115 s per step. Reference materials were measured 5 min with step size of 0.017° and scan time of 10 s per step.

The Scherrer equation was used to determine the stacking degree of sulfide slabs in the unsupported catalyst, knowing that the diffraction at 14° 2 θ corresponds to the (002) plane with interplanar distance of 6.1 Å (distance from one to another molybdenum layer in MoS₂ slab):

$$L = \frac{K \cdot \lambda}{\Delta(2\theta) \cdot \cos\theta}$$

where L is the mean size of ordered (crystalline) domain, K is a Scherrer shape factor (0.9), λ is the used X-ray wavelength, θ is a Bragg angle, and $\Delta(2\theta)$ is a line broadening at half maximum intensity (FWHM) in radians. To calculate the line broadening at FWHM following equation was used:

$$\Delta(2\theta) = \text{FWHM} - 0.1$$

where FWHM is the full width at the half maximum in radians, and 0.1 is characteristic of the instrument.

Transmission electron microscopy - selective area diffraction (TEM-SAD). Catalysts were ground, suspended in ethanol and ultrasonically dispersed. Dispersion drops were applied on a copper-carbon grid. Measurements were carried out on a transmission electron microscope device JEOL JEM-2011 with an accelerating voltage of 120 keV.

Raman spectroscopy. Raman spectra were obtained with a Renishaw Raman Spectrometer (Type 1000) equipped with CCD detector and a Leica microscope DM LM using 514 nm Ar laser. Prior to the measurements, calibration was done with Si (111) crystal. The wavenumber accuracy was within 1 cm^{-1} . Oxidic catalyst precursors and the reference materials were analyzed under ambient conditions and the samples were pressed into self-supported wafers and placed onto a quartz sample holder. In situ measurements were applied to follow the catalyst activation. The samples were placed into the quartz cell which was attached to a heating wire and connected to a flow system. Sulfidation was performed in 10% H_2S in H_2 at 400 °C for 1 hour and spectra were taken during heating, at every 100 °C. To avoid possible temperature influence, the sample was cooled to the room temperature in sulfiding agent and the flow was switched to N_2 for measuring the last spectrum.

Diffuse reflectance UV-vis spectroscopy. The diffuse reflectance technique was applied to collect the ultraviolet-visible-near infrared spectra using Avantes AvaSpec-2048 fiber optic spectrometer equipped with CCD detector array. Combined deuterium and halogen light, Ava Light-DH-S-BAL, was applied as a source in a combination with a fiber optic cable FCR-7UV400-2-SR-HT. Spectra of oxidic catalyst precursors and reference materials were recorded under ambient conditions. The samples were placed as powder in a Teflon sample holder which provided 1 mm sample thickness.

X-ray absorption spectroscopy (XAS). The structural properties of the oxidic catalyst precursors and the sulfide catalysts as well as the catalyst activation were studied by X-ray absorption spectroscopy, measured on X1 beamline at Hasylab, DESY (Hamburg, Germany). The spectra were recorded in a transmission mode at the Mo K-edge (20 000 eV) using a Si (311) crystal. The higher harmonics contributions were eliminated by detuning the monochromator to 60% of the maximum intensity. The spectra of corresponding metal foils were measured simultaneously for the monochromator energy calibration. Catalysts were pressed into self-supporting wafers while the reference compounds were mixed with cellulose to achieve an absorption of $\mu x = 1.5$. All X-ray absorption spectra used for EXAFS analysis were carried out in He flow and at liquid N_2 temperature (LNT) to minimize thermal vibrations. The catalyst wafers were placed into a stainless steel in situ flow cell and prior to

activation EXAFS of oxide precursors was recorded. Quick XAFS measurements were carried out during catalyst activation in 10% H₂S in H₂ with a heating rate of 5 °C/min. At 400 °C the temperature was held isothermally for 1 h. The catalysts were then cooled to room temperature in the sulfiding agent and further cooled to the liquid N₂ temperature in He flow in order to record EXAFS of the sulfided phase. Quick XAFS and XANES data were processed with Xanda program while EXAFS data were processed with VIPER. After background correction using polynomial function and weighting with k^2 , the local environment was determined by EXAFS analysis in k-space applying the single and multiple Mo-O, Mo-Mo and Mo-S scattering phase shifts and amplitudes, calculated with FEFF (version 8.4) [10]. The K range used for the oxide precursor was 2.8-17 1/Å and for the sulfided catalyst 3-17 1/Å.

Temperature-programmed sulfidation (TPS). The catalyst activation was performed by temperature-programmed reaction/sulfidation (TPS) to study the influence of nickel as a promoter on the sulfidation mechanism. The oxide precursor (0.1 g) was placed in the flow reactor equipped with a ceramic oven (Horst GmbH). The activation was performed in 10% H₂S in H₂ with a heating rate of 5 °C/min. At 400 °C the temperature was held isothermally for 1 h. Evolved gasses were detected by a mass spectrometer (Balzers QME 200).

2.3. Catalyst performance

The HDN of quinoline (22 kPa) was studied in the presence of dibenzothiophene (3.4 kPa) and the reaction was carried out in a continuous flow fixed-bed reactor system. The reactor was loaded with 0.05 g of catalyst for each run and the reaction was performed at a constant pressure and feed composition. Gas and liquid feed were introduced to the reactor via high pressure mass flow meters (Bronkhorst) and a HPLC pump (Shimadzu LC-20AD) respectively. After separation of liquid and gas phase, the liquid was collected and analyzed by off line gas chromatography using a HP 6890 GC instrument equipped with a flame ionization detector (FID) and 60 m long DB-17 capillary column.

Prior to the kinetic experiments, the catalysts were activated in situ in 10% H₂S in H₂ flow at 400 °C and 1.8 MPa for 8 h. After cooling to room temperature in the sulfiding agent, the catalysts were flushed with hydrogen and the liquid feed flow and reaction temperature were set and a total pressure of 5.0 MPa. Steady state was reached after 16 h time on stream. Kinetic studies were carried out at 370 °C as a function of space time, based on quinoline feed rate only ($h \cdot g_{cat}/mol$ of quinoline), and as a function of temperature at the constant space time of 350 $h \cdot g_{cat}/mol$. Temperatures studied were: 290, 330, 370, and 400 °C. The

conversion of quinoline to nitrogen-free products is referred to as HDN conversion. All reactions were performed in great excess of hydrogen, with the constant hydrogen to hydrocarbon ratio of 330 Ndm³/dm³, whereas the hydrogen to N-containing compound molar ratio is approximately 220.

3. Results

3.1. Physicochemical properties

An overview of the physicochemical characteristics of the oxidic catalyst precursors is given in Table 1.

Catalyst	Metal concentration [wt.%]		Ni molar fraction	NO adsorption [$\mu\text{mol/g}$]	Surface area [m^2/g]	Pore volume [cm^3/g]	Pore diameter [nm]
	Mo	Ni					
Mo/ $\gamma\text{-Al}_2\text{O}_3$	8.6	-	-	130	220	0.62	8.5
NiMo/ $\gamma\text{-Al}_2\text{O}_3$	8.6	3.6	0.4	160	206	0.60	8.5
NiMo/unsupported	38.2	25.1	0.5	66	26	0.06	2.6

Table 1. Physicochemical properties of the supported Mo/ $\gamma\text{-Al}_2\text{O}_3$, NiMo/ $\gamma\text{-Al}_2\text{O}_3$ and NiMo/unsupported oxide catalyst precursors, where Ni molar fraction is calculated according to: $r = \text{Ni}/(\text{Ni}+\text{Mo})$.

The specific surface area of the supported oxidic catalyst precursors did not differ from the used alumina support. The determined Mo concentration was 8.6 wt.%, which corresponds to 2.5 Mo atoms/nm² and the Ni concentration was 3.6 wt.% Ni, leading to a molar fraction of 0.4 Ni in the mixed supported catalyst. The specific surface area of the NiMo/unsupported oxide precursor was 26 m²/g. Determined Mo and Ni concentration was 38.2 and 25.1 wt.%, respectively, leading to Ni molar fraction of 0.5 in the unsupported catalyst.

The total NO uptake during the adsorption at room temperature was 130, 160, and 66 $\mu\text{mol/g}_{\text{cat}}$ for MoS₂/ $\gamma\text{-Al}_2\text{O}_3$, NiMoS/ $\gamma\text{-Al}_2\text{O}_3$, and NiMoS/unsupported catalyst, respectively. Considering that NO adsorbs as dinitrosyl species on metal cations [11], the concentration of the active sites was thus 65 $\mu\text{mol/g}_{\text{cat}}$ for MoS₂/ $\gamma\text{-Al}_2\text{O}_3$, 80 $\mu\text{mol/g}_{\text{cat}}$ for NiMoS/ $\gamma\text{-Al}_2\text{O}_3$, and 33 $\mu\text{mol/g}_{\text{cat}}$ for NiMoS/unsupported catalyst.

3.2. X-ray diffraction (XRD)

3.2.1. Oxide catalyst precursors

The XRD patterns of oxidic catalyst precursors and reference materials are shown in Fig. 1. Supported Mo and NiMo/ $\gamma\text{-Al}_2\text{O}_3$ catalysts did not show any additional diffraction reflections except the ones characteristic for the support material (37, 39, 46, 61, and 67° 2 θ). Thus,

after molybdenum and nickel impregnation, a new crystalline phase was not observed. NiMo/unsupported oxidic catalyst precursor exhibited well defined diffraction reflections at: 11, 26.8, 27.2, 29.8, 40.5, 50.5, 58, and 62° 2θ corresponding to nickel molybdate, NiMoO₄, and 12, 17.6, 18.9, 23.8, 29.8, 32.2, 34.8, 37.2, 39, 40.5, 46.5, 49.2, 55.2, and 58.6° 2θ corresponding to an ammonium nickel molybdate, (NH₄)H₂Ni₂(OH)₂(MoO₄)₂ [12].

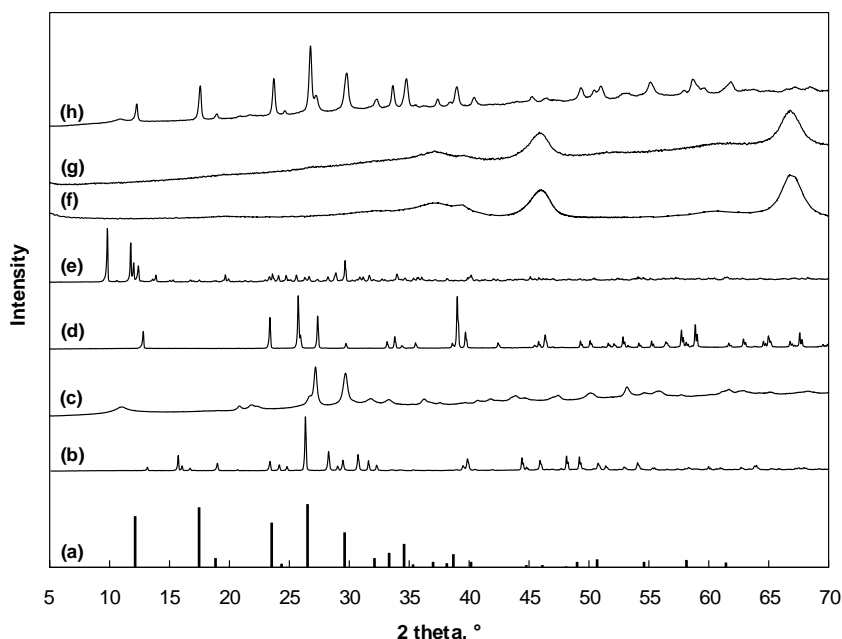


Figure 1. X-ray diffraction patterns of: (a) (NH₄)H₂Ni₂(OH)₂(MoO₄)₂ [[12]], (b) K₂MoO₄, (c) NiMoO₄, (d) MoO₃, (e) (NH₄)₆Mo₇O₂₄, (f) γ-Al₂O₃ support, (g) NiMo/γ-Al₂O₃, and (h) NiMo/unsupported precursor.

3.2.2. Sulfide catalysts

The XRD patterns of sulfided catalysts and reference sulfide materials are given in Fig. 2. Supported MoS₂/γ-Al₂O₃ and NiMoS/γ-Al₂O₃ catalysts exhibited two diffraction peaks at around 33 and 59° 2θ characteristic for the MoS₂ crystalline structure with interplanar distances of 2.7 and 1.5 Å. The diffraction peak at 14° 2θ, characteristic for the (002) plane with interplanar distance of 6.1 Å [13], was not observed probably due to the low degree of stacking in the formed MoS₂ and NiMoS particles.

The XRD pattern of the NiMoS/unsupported catalyst exhibited well defined peaks at: 14, 33, 40, 50, and 59° 2θ corresponding to MoS₂ and 31, 33, 51, and 56° 2θ corresponding to Ni₃S₂ crystalline structure. The relatively high intensity of the peak at 14° 2θ indicated much higher stacking degree in the NiMoS/unsupported than in the supported MoS₂/γ-Al₂O₃ and NiMoS/γ-Al₂O₃ catalysts. FWHM at 14° 2θ was 2.1°, therefore using the Scherrer equation the size of crystalline domain was determined to be around 40 Å. Knowing that the interplanar distance for the (002) plane is 6.1 Å, the stacking degree in the unsupported catalyst was calculated to be 7.

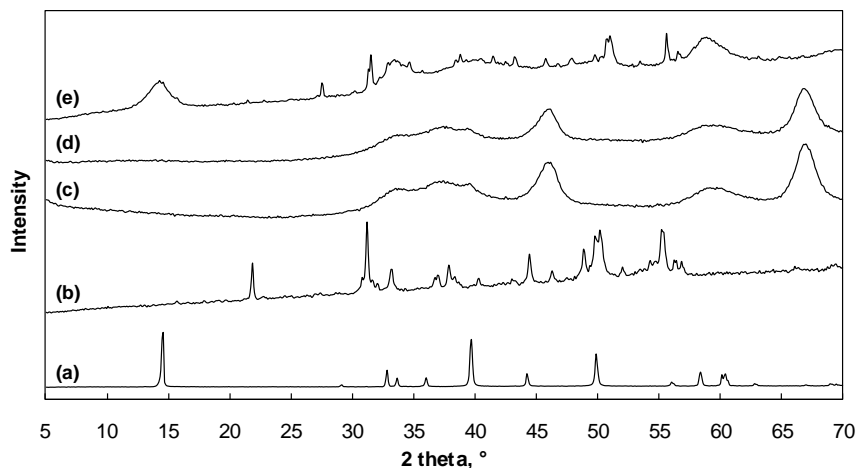


Figure 2. X-ray diffraction patterns of: (a) MoS_2 , (b) Ni_3S_2 , (c) $\text{MoS}_2/\gamma\text{-Al}_2\text{O}_3$, (d) $\text{NiMoS}/\gamma\text{-Al}_2\text{O}_3$, and (e) $\text{NiMoS}/\text{unsupported}$.

3.3. Transmission electron microscopy – selective area diffraction (TEM-SAD)

3.3.1. Supported sulfide catalysts

The TEM micrographs of the supported sulfided catalysts are presented in Fig. 2 of Chapter 2. The catalysts revealed the presence of typical layer like MoS_2 phase. The observed stacking did not exceed three layers confirming a good dispersion of the sulfided slabs on the $\gamma\text{-Al}_2\text{O}_3$ support as suggested by XRD.

3.3.2. NiMo unsupported oxide catalyst precursor

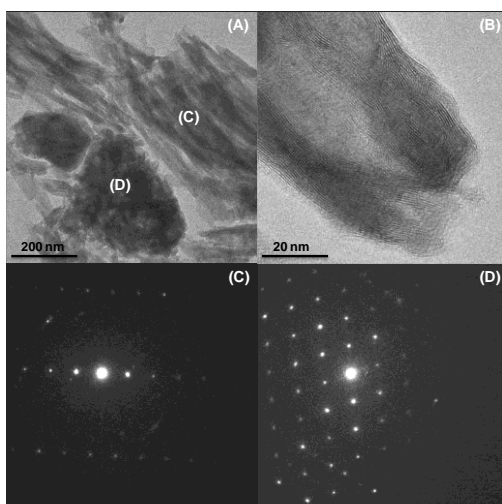


Figure 3. Transition electron microscopy picture of $\text{NiMo}/\text{unsupported}$ oxidic precursor (A) and $\text{NiMoS}/\text{unsupported}$ catalyst (B). Selective area diffractograms of $\text{NiMo}/\text{unsupported}$ oxidic precursor, taken at different positions: rod-like structure (C) and bulk structure (D).

$\text{NiMo}/\text{unsupported}$ oxidic catalyst precursor exhibited domains with rod-like and bulk structure, as seen in Fig. 3 (A). Selective area diffraction was used to determine the

corresponding crystalline phase patterns, shown in Fig. 3 (C) and (D), respectively. Calculated interplanar distances (d , Å) and the corresponding XRD reflections (2θ °) are given in Table 2. Rod-like structure was related to nickel molybdate, NiMoO_4 , and the bulk to an ammonium nickel molybdate, $(\text{NH}_4)\text{HfNi}_2(\text{OH})_2(\text{MoO}_4)_2$.

NiMoO_4 (Rod structure; Fig.3. (C))		$(\text{NH}_4)\text{HfNi}_2(\text{OH})_2(\text{MoO}_4)_2$ (Bulk structure; Fig. 4. (D))	
d , Å	2θ , °	d , Å	2θ , °
5.1	17.5	4.7	18.9
3.2	27.6	3.8	23.4
2.6	34.7	3.0	29.8
1.7	53.2	2.3	38.3
1.6	58.6	1.9	47.9
1.4	65.0	1.6	57.1
1.3	71.6	1.5	62.6
		1.3	73.3
		1.0	97.6

Table 2. Interplanar distances (Å) obtained by TEM-SAD of NiMo/unsupported oxidic precursor, and corresponding reflection angles for the two identified phases, NiMoO_4 and $(\text{NH}_4)\text{HfNi}_2(\text{OH})_2(\text{MoO}_4)_2$.

3.3.3. NiMo unsupported sulfide catalysts

The TEM micrographs show the existence of typical highly stacked MoS_2 -like clusters which are bent on a longer scale. The characteristic curvature is a consequence of a rapid growth along the basal plane and a very slow growth along the c -axis [14]. The interplanar distance between the two molybdenum layers in a (002) direction was measured at about 6 Å and an average stacking degree was determined to be approximately seven.

3.4. Raman spectroscopy

3.4.1. Oxide catalyst precursors

The Raman spectra of the oxidic catalyst precursors and different oxidic reference compounds are shown in Fig. 4 and the overview of the observed bands is given in Table 3. Obtained frequencies are related to the vibration modes according to the review published by Mestl et al. [15].

The Raman spectrum of $\text{Mo}/\gamma\text{-Al}_2\text{O}_3$ catalyst exhibits bands at 961, 860, 350, and 224 cm^{-1} . Vibrations are assigned to the stretching of terminal $\text{Mo}=\text{O}$, asymmetric and symmetric stretching of bridging $\text{Mo}-\text{O}-\text{Mo}$, bending of terminal $\text{Mo}=\text{O}$ and deformation of bridging $\text{Mo}-\text{O}-\text{Mo}$ bonds, respectively. Due to the position of the highest frequency vibration and the presence of the characteristic bridging $\text{Mo}-\text{O}-\text{Mo}$ bond vibration, it is proposed that the surface molybdenum species are present as polymolybdates [16]. Shift to higher

frequencies, comparing to the ammonium heptamolybdate (AHM) reference spectrum is expected due to the strong interaction of molybdenum species with the γ - Al_2O_3 support. After nickel impregnation, the Raman band corresponding to the terminal Mo=O symmetric stretching vibration was shifted downwards from 961 to 947 cm^{-1} . The shoulder at 860 cm^{-1} assigned to the asymmetric stretching vibration of Mo-O-Mo bridging bond became more intense.

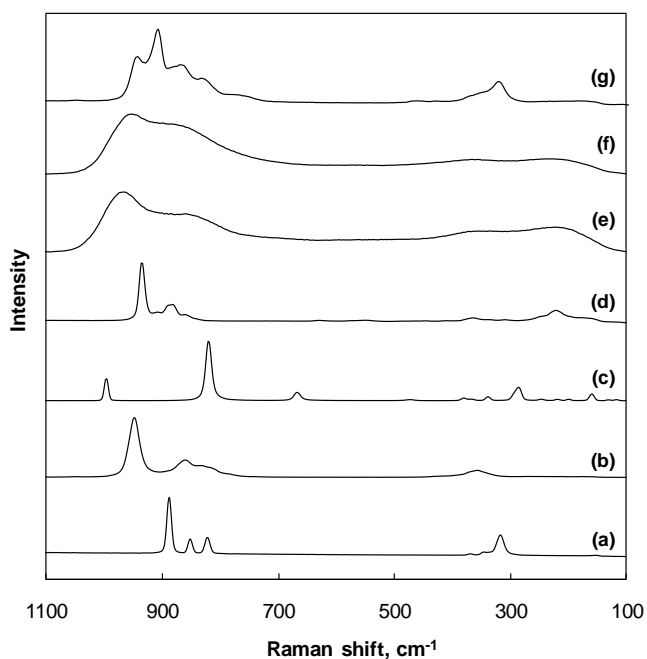


Figure 4. Raman spectra of references and oxidic catalyst precursors: (a) K_2MoO_4 , (b) NiMoO_4 , (c) MoO_3 , (d) $(\text{NH}_4)_6\text{Mo}_7\text{O}_{24}$, (e) $\text{Mo}/\gamma\text{-Al}_2\text{O}_3$, (f) $\text{NiMo}/\gamma\text{-Al}_2\text{O}_3$, and (g) $\text{NiMo}/\text{unsupported}$.

	ν M=O	ν_{as} M-O-M	ν_{s} M-O-M	δ M=O	δ M-O-M
$\text{Mo}/\gamma\text{-Al}_2\text{O}_3$	961	860	-	360	224
$\text{NiMo}/\gamma\text{-Al}_2\text{O}_3$	947	860	-	360	224
$\text{NiMo}/\text{unsupported}$	944	869	831	354	-
				321	
K_2MoO_4	888	852	-	347	-
		821		316	
NiMoO_4	950	860	834	357	-
MoO_3	996	821	667	472	159
				377	
				339	
				285	
$(\text{NH}_4)_6\text{Mo}_7\text{O}_{24}$	934	-	-	364	221
	883				

Table 3. Raman bands (cm^{-1}) characteristic for the oxide catalyst precursors and reference materials.

The Raman spectrum of the $\text{NiMo}/\text{unsupported}$ oxide catalyst reveals much more defined Raman bands than the corresponding $\text{NiMo}/\gamma\text{-Al}_2\text{O}_3$ catalyst. The bands are found at around

944, 909, 869, 831, 354, and 321 cm^{-1} and they are assigned to the stretching of the terminal Mo=O, asymmetric and symmetric stretching of bridging Mo-O-Mo and bending of terminal Mo=O, respectively. The spectrum reveals a combination of the bond vibrations found in nickel molybdate (944, 869, 831, and 354 cm^{-1}), and an ammonium nickel molybdate (909 and 321 cm^{-1}) [17].

3.4.2. Sulfide catalysts

In situ Raman spectroscopy was used to follow the sulfidation of the precursor and oxidation of the activated sulfide catalysts. Only spectra for the Mo/ γ -Al₂O₃ catalyst are shown in Fig. 5, since it was not possible to observe any differences in the activation behavior of the promoted NiMo/ γ -Al₂O₃ catalyst.

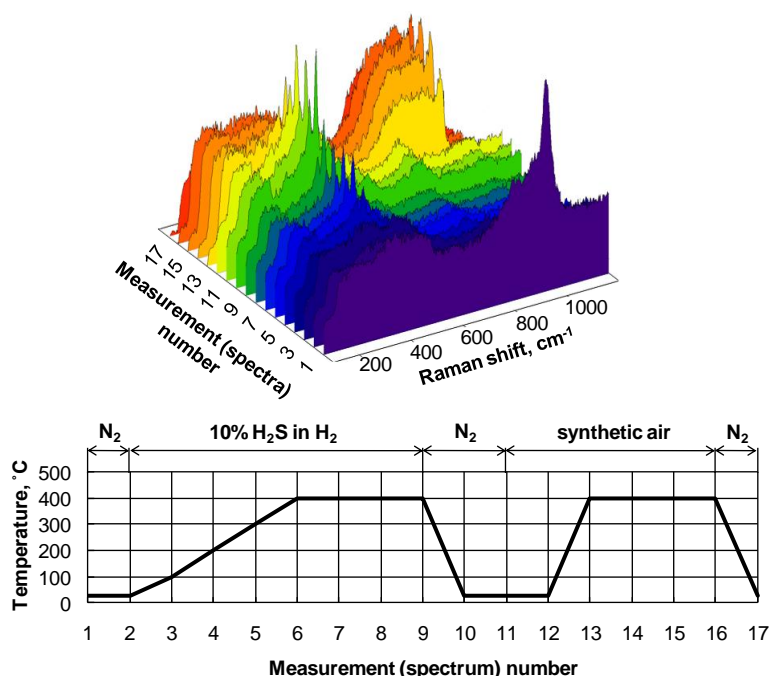


Figure 5. Raman spectra collected during the sulfidation of the Mo/ γ -Al₂O₃ catalyst and further oxidation of the formed sulfide. On the bottom graph, the corresponding profile of the temperature program and used gases is given.

The color change and disappearance of the Mo-O vibration bands indicated that the oxide catalyst precursors are partially sulfided already at room temperature. Bands corresponding to the MoS₂ phase were first observed at 300 °C and the color of the samples turned completely black. After catalyst activation at 400 °C, synthetic air was applied at room temperature and sulfide samples were stable. Bands of MoS₂ phase disappeared in synthetic air at 400 °C and new bands appeared at 985 cm^{-1} corresponding to the Mo-O asymmetric vibrations. Regenerated oxide species were not the same as the original oxide precursor. Representative Raman spectra of the MoS₂/ γ -Al₂O₃, NiMoS/ γ -Al₂O₃, and NiMoS/unsupported catalysts are given in Fig. 6. The bands related to the MoS₂ phase are

found in all three samples: 287, 383, and 409 cm^{-1} , corresponding to S-Mo-S vibration along the basal plane, Mo-S vibration along the basal plane, and S-Mo-S vibration along the c-axis, respectively [18,19]. The presence of Ni_3S_2 could not be seen in the sulfided catalysts containing nickel.

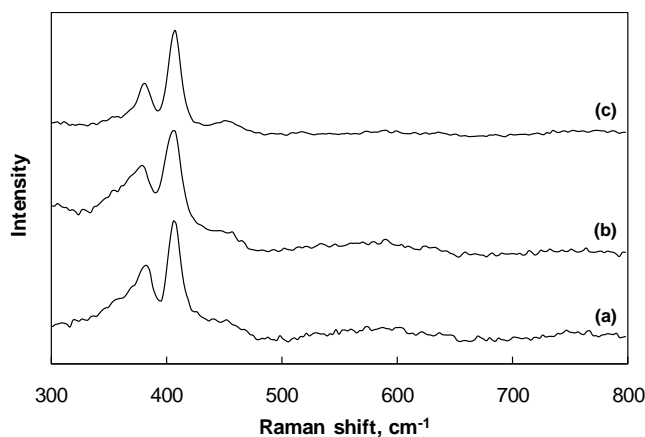


Figure 6. Raman spectra of the sulfided catalysts: (a) $\text{MoS}_2/\gamma\text{-Al}_2\text{O}_3$ and (b) $\text{NiMoS}/\gamma\text{-Al}_2\text{O}_3$, and (c) $\text{NiMoS}/\text{unsupported}$.

3.5. Diffuse reflectance UV-vis spectroscopy

The diffuse reflectance UV-vis spectra of supported and unsupported oxide catalyst precursors and the oxide reference materials are shown in Fig. 7. The edge absorptions and the corresponding band gaps (E_g , eV) are summarized in Table 4.

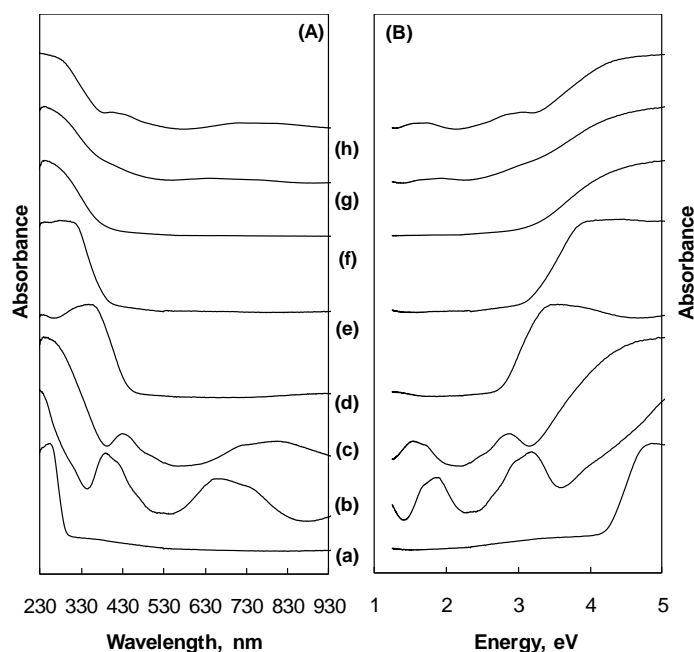


Figure 7. Diffuse reflectance UV-vis spectra of the oxidic catalyst precursors presented in wavelength (A) and energy scale (B): (a) K_2MoO_4 , (b) $\text{Ni}(\text{OH})_2$, (c) NiMoO_4 , (d) MoO_3 , (e) $(\text{NH}_4)_6\text{Mo}_7\text{O}_{24}$, (f) $\text{Mo}/\gamma\text{-Al}_2\text{O}_3$, (g) $\text{NiMo}/\gamma\text{-Al}_2\text{O}_3$, and (h) $\text{NiMo}/\text{unsupported}$.

	Absorption edge, [nm]	Band gap, E_g [eV]	Number of the next nearest Mo neighbors
Oxidic catalyst precursors:			
Mo/ γ -Al ₂ O ₃	351	3.5	2.7
NiMo/ γ -Al ₂ O ₃	360	3.4	3.1
NiMo/unsupported	352	3.5	2.8
Reference materials:			
K ₂ MoO ₄	285	4.4	0
Ni(OH) ₂	293	4.2	-
NiMoO ₄	354	3.5	2.7
MoO ₃	422	2.9	5.0
(NH ₄) ₆ Mo ₇ O ₂₄	366	3.4	3.1

Table 4. Absorption edge and the band gap determined from UV-vis spectra by making the linear regression of the least-squares fit of a line through the low energy edge of the transformed spectra.

Supported Mo/ γ -Al₂O₃ and NiMo/ γ -Al₂O₃ catalyst precursors exhibited the absorption edge at 350 and 360 nm, respectively while the NiMo/unsupported at 350 nm. NiMo/ γ -Al₂O₃ catalyst additionally revealed one shoulder at around 430 nm (Ni²⁺ in octahedral coordination) and an additional absorption band at 640 nm (Ni²⁺ in octahedral coordination), similarly to NiMoO₄ reference material. NiMo/unsupported catalyst additionally showed three bands at 430, 700, and 820 nm, assigned to octahedral Ni²⁺ species [20,21]. The UV-vis spectra was transformed, i.e., (Abs·h ν)² vs. h ν was plotted, in order to estimate the domain size in the catalyst precursors determining the band gap from the intercept from a fitted straight line [22]. It has been found that all precursors exhibit the band gap between 3.4 and 3.5 eV, which was in line with NiMoO₄ and (NH₄)₆Mo₇O₂₄ references. The band gap was correlated with the number of the next nearest molybdenum neighbors, using the Webber model ($N_{Mo} = 16 - 3.8 \cdot E_g$) and it was inferred that large MoO₃-like domains were not formed. The catalyst structure exhibited around three next nearest molybdenum neighbors in all precursors which is comparable with NiMoO₄ and (NH₄)₆Mo₇O₂₄ references.

3.6. X-ray absorption spectroscopy (XAS)

In order to reveal the local structure of the molybdenum in the oxide and sulfide catalysts, Mo K-edge XAS measurements were performed. XANES was used as a “fingerprint”, to determine Mo oxidation state and the local environment while EXAFS provided a detailed picture of the catalyst structure.

3.6.1. Oxide catalyst precursors

XANES of the catalyst precursors and reference materials on the Mo K-edge are shown in Fig. 8 (A). The XANES of all three catalyst precursors exhibited a characteristic pre-edge peak at 19995 eV, due to the electronic 1s→4d transition [23]. This transition is only allowed

in tetrahedral or distorted octahedral coordinations of Mo^{6+} . As seen from the XANES of the reference compounds the tetrahedral Mo^{6+} , in K_2MoO_4 , exhibits the highest intensity of the pre-edge peak while the distorted octahedral Mo^{6+} , in MoO_3 , exhibits a very weak pre-edge peak. Mo^{4+} and Mo^0 do not show the pre-edge peak, since it is characteristic only for Mo^{6+} .

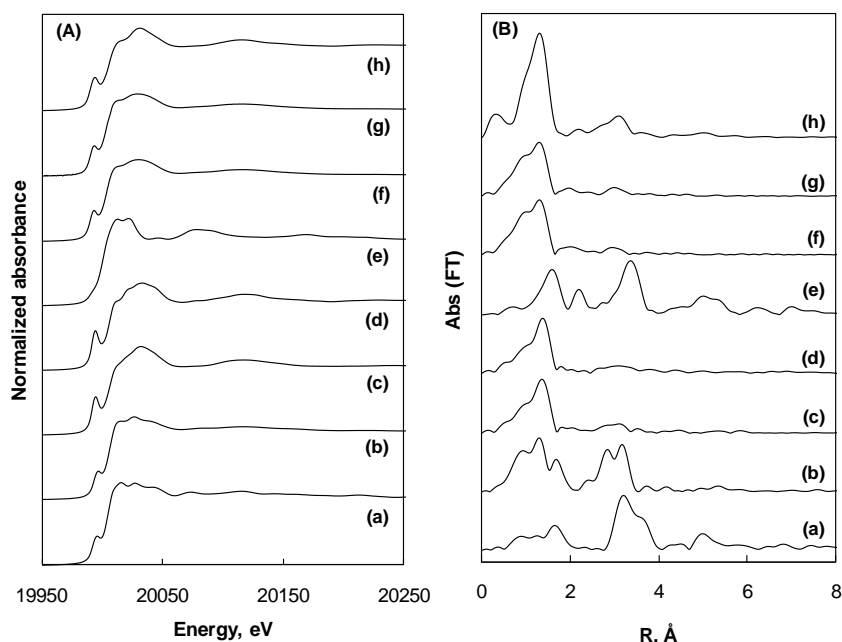


Figure 8. Mo K-edge XANES (A) and EXAFS (B) of the oxidic catalyst precursors: (a) MoO_3 , (b) $(\text{NH}_4)_6\text{Mo}_7\text{O}_{24}$, (c) NiMoO_4 , (d) K_2MoO_4 , (e) MoO_2 , (f) $\text{Mo}/\gamma\text{-Al}_2\text{O}_3$, (g) $\text{NiMo}/\gamma\text{-Al}_2\text{O}_3$, and (h) $\text{NiMo}/\text{unsupported}$.

Catalyst	Shell	r , Å	N	σ^2 , Å ²	E_0 , eV
$\text{Mo}/\gamma\text{-Al}_2\text{O}_3$	Mo-O	1.72	4.1	0.0095	-17.27
	Mo-O	2.12	2.3	0.0650	37.54
	Mo-O	2.40	0.3	0.0027	-15.49
	Mo-Mo	3.27	1.2	0.0119	-15.29
	Mo-O	2.86	5.3	0.0270	-1.87
	Mo-O	4.00	0.3	0.0070	13.71
$\text{NiMo}/\gamma\text{-Al}_2\text{O}_3$	Mo-O	1.72	4.1	0.0094	-18.07
	Mo-O	1.98	2.0	0.0914	18.01
	Mo-O	2.42	0.6	0.0068	6.55
	Mo-Mo	3.38	1.5	0.0130	-7.14
	Mo-Ni	3.41	1.3	0.0086	-5.46
$\text{NiMo}/\text{unsupported}$	Mo-O	1.79	4.1	0.0041	-5.70
	Mo-O	2.25	1.9	0.0149	-32.43
	Mo-O	3.07	3.0	0.0205	3.53
	Mo-Mo	3.15	1.3	0.0234	-1.40
	Mo-O	3.51	2.6	0.0025	-3.90
	Mo-Ni	3.56	2.1	0.0250	1.34
	Mo-Mo	3.69	4.1	0.0160	-11.93

Table 5. Fitting results for FT of Mo K-edge $k^2 \chi(k)$ of the oxide catalyst precursors. N: coordination number, r : distance, E_0 : inner potential, and σ^2 : Debye-Waller factor.

Fourier transformed EXAFS on the Mo K-edge of the catalyst precursors and reference materials are shown in Fig. 8 (B). The catalyst precursors exhibited maximum of the Mo-O contribution at 1.4 Å (not phase corrected). All distances from the radial distribution function are shifted to lower values due to the phase shift and the correct distances are observed by fitting the oscillations.

The EXAFS analysis of the catalyst precursors showed the presence of four short Mo-O bonds (1.72 Å for supported and 1.79 Å for the unsupported catalyst) and two longer, bridging, Mo-O bonds (at around 2.1 Å), indicating that Mo⁶⁺ is in the distorted octahedral coordination. Due to the mixture of the two phases found in NiMo/unsupported catalyst, it was difficult to interpret the EXAFS in terms of the coordination numbers and next nearest neighbors. The fitting results are presented in Table 5 and Fig. 9.

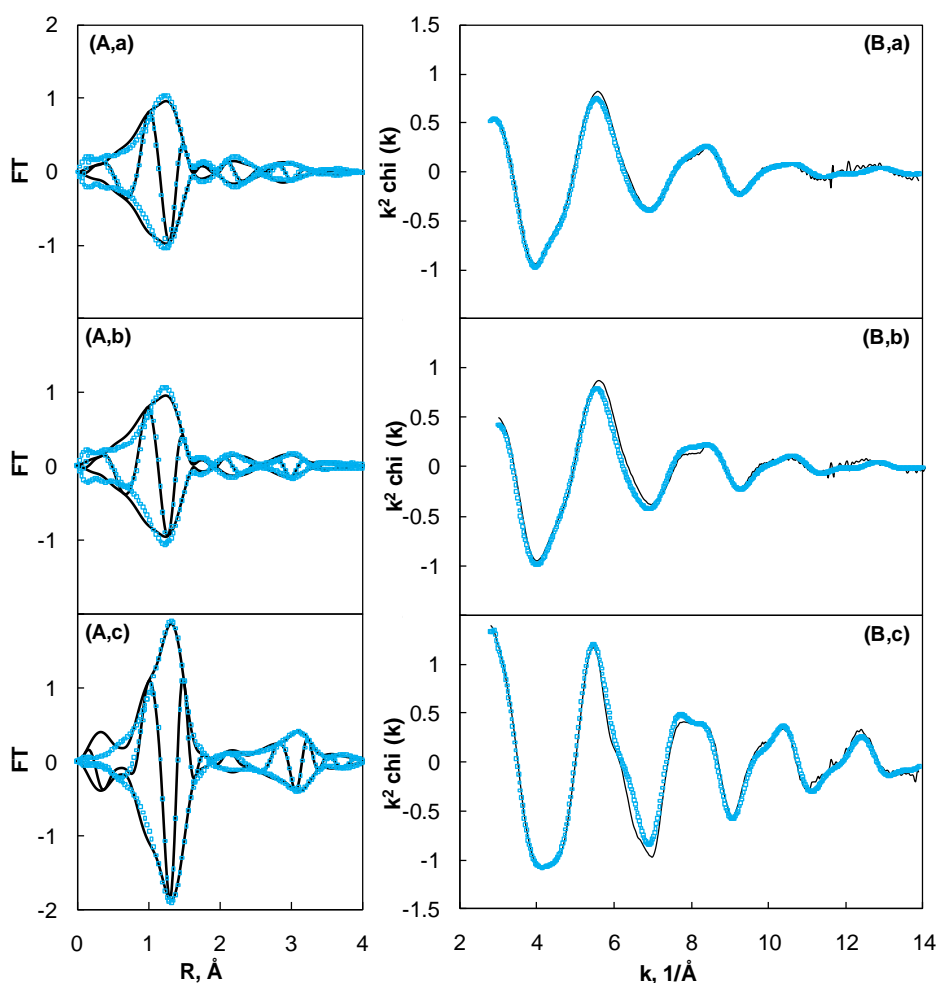


Figure 9. Results and fitted data (squares) for the Mo K-edge data of (a) Mo/ γ -Al₂O₃, (b) NiMo/ γ -Al₂O₃, and (c) NiMo/unsupported oxide catalyst precursor; (A) k^2 weighted Fourier transform and (B) EXAFS.

3.6.2. Transition from oxide precursors to sulfide catalysts

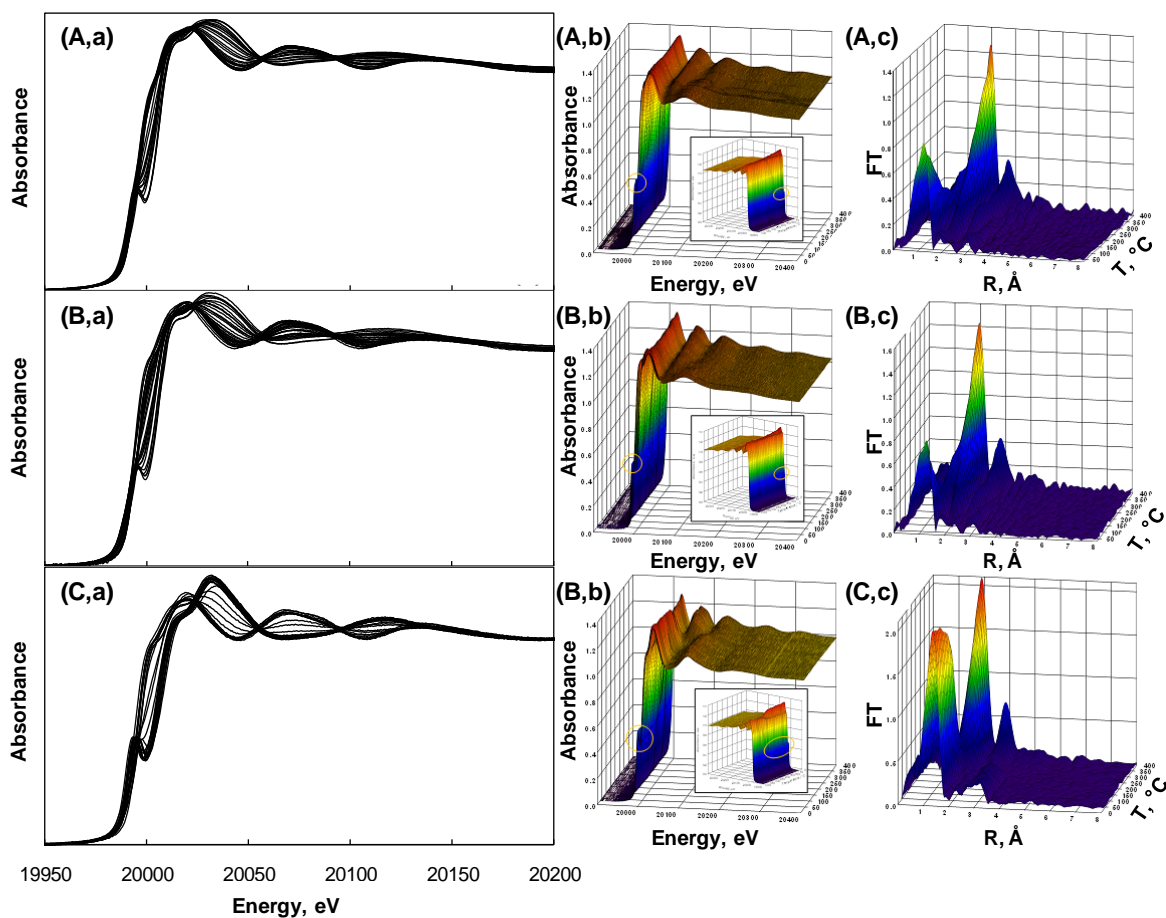


Figure 10. Results for the Mo K-edge data during sulfidation (10% H₂S in H₂) of (A) MoS₂/γ-Al₂O₃, (B) NiMoS/γ-Al₂O₃, and (C) NiMoS/unsupported catalysts: (a) Quick EXAFS, (b) Quick EXAFS as a function of the temperature, and (c) Fourier transform as a function of the temperature.

Quick EXAFS on the Mo K-edge, measured during the catalyst sulfidation, is presented in Fig. 10 for all three catalysts. Fig. 10 (a) illustrates the existence of the two isosbestic points at which the total absorbance does not change during the sulfidation in the studied temperature range. The transformation from the oxide precursor to the sulfide catalyst indicated that secondary reaction did not occur. At first an exchange of oxygen for sulfur occurs on the Mo⁶⁺, observed by decrease of the Mo-O contribution and later formation of new Mo-S contribution at around 2.1 Å (not phase corrected). Therefore the catalyst was present in the oxosulfidic form. Then the molybdenum reduction occurs which can be seen by the disappearance of the molybdenum pre-edge feature and the energy of the absorption edge is moving towards lower values. At the same time the EXAFS show the disappearance of the Mo-Mo contribution at 3 Å (not phase corrected) which indicates that Mo-O-Mo bridges are not present anymore. At last, further oxygen for sulfur exchange on the Mo⁴⁺ occurs. The intensity of the Mo-S shell at around 2 Å and Mo-Mo shell at 2.8 Å (not phase

corrected) was further increased [24]. The measurements are also presented in 3-D graph as a function of the sulfidation temperature, Fig. 10 (b) and (c).

The overall sulfidation mechanism was common for all catalysts studied. Nevertheless, the temperatures at which reduction of Mo^{6+} occurs, indicated by disappearance of the pre-edge feature, were different, Fig. 11. Introduction of Ni into the supported catalyst shifted the reduction towards lower temperature. The pre-edge disappearance in $\text{Mo}/\gamma\text{-Al}_2\text{O}_3$ catalyst is observed between 217 °C and 234 °C, and in $\text{NiMo}/\gamma\text{-Al}_2\text{O}_3$ catalyst between 189 °C and 205 °C. More precise determination of the reduction temperatures was done by temperature-programmed sulfidation (TPS). Parallel consumption of H_2 and production of H_2S indicated the reduction temperature at 220 °C in $\text{Mo}/\gamma\text{-Al}_2\text{O}_3$ and at 205 °C in $\text{NiMo}/\gamma\text{-Al}_2\text{O}_3$ catalyst. Detailed experiment is described elsewhere [9]. The reduction temperature in the unsupported catalyst was found to be higher, at around 280 °C.

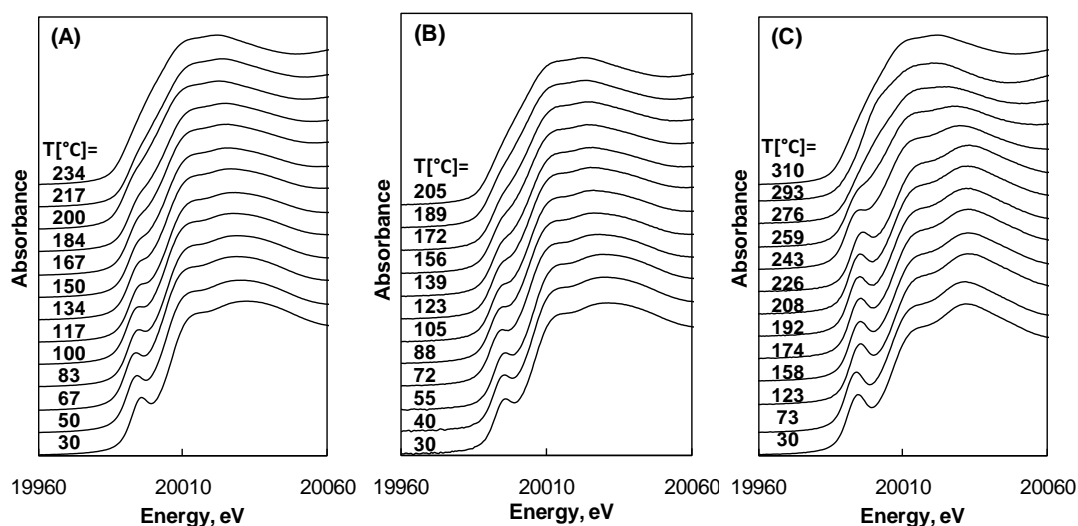


Figure 11. Results for the Mo K-edge data; Reduction of Mo^{6+} to Mo^{4+} in (A) $\text{Mo}/\gamma\text{-Al}_2\text{O}_3$ at $T = 220^\circ\text{C}$, (B) $\text{NiMo}/\gamma\text{-Al}_2\text{O}_3$ at $T = 205^\circ\text{C}$, and (C) $\text{NiMo}/\text{unsupported catalyst}$ at $T = 280^\circ\text{C}$.

3.6.3. Sulfide catalysts

Fourier transforms on the Mo K-edge are presented in Fig. 12 for the sulfided supported and unsupported catalysts. The features observed were identical to the ones found in the reference material MoS_2 , Fig. 12 (d). This indicated that the catalysts exhibited MoS_2 -like structure.

After the EXAFS analysis, structural parameters were obtained and the best fit for the Mo-S, Mo-Mo and Mo-Ni contributions is presented in Table 6. Lower coordination numbers, $N_{\text{Mo-S}} = 4.2$ (at 2.41 Å) and $N_{\text{Mo-Mo}} = 3.2$ (at 3.16 Å), were found in the $\text{MoS}_2/\gamma\text{-Al}_2\text{O}_3$ catalyst comparing to the bulk MoS_2 , where $N_{\text{Mo-S}} = 6$ (at 2.41 Å) and $N_{\text{Mo-Mo}} = 6$ (at 3.16 Å). In the

nickel promoted catalysts the coordination numbers were $N_{\text{Mo-S}} = 5.7$ and $N_{\text{Mo-Mo}} = 4.7$ for NiMoS/ $\gamma\text{-Al}_2\text{O}_3$ and $N_{\text{Mo-S}} = 5.5$ and $N_{\text{Mo-Mo}} = 5.2$ for NiMoS/unsupported. Moreover, the new Mo-Ni contribution was found with the coordination number of $N_{\text{Mo-Ni}} = 0.4$ (at 3.0 Å) and 0.8 (at 3.17 Å) in the supported and unsupported catalysts, respectively. The Mo-Ni contribution is overlapping the Mo-Mo contribution therefore it is not directly observable in Fourier transforms.

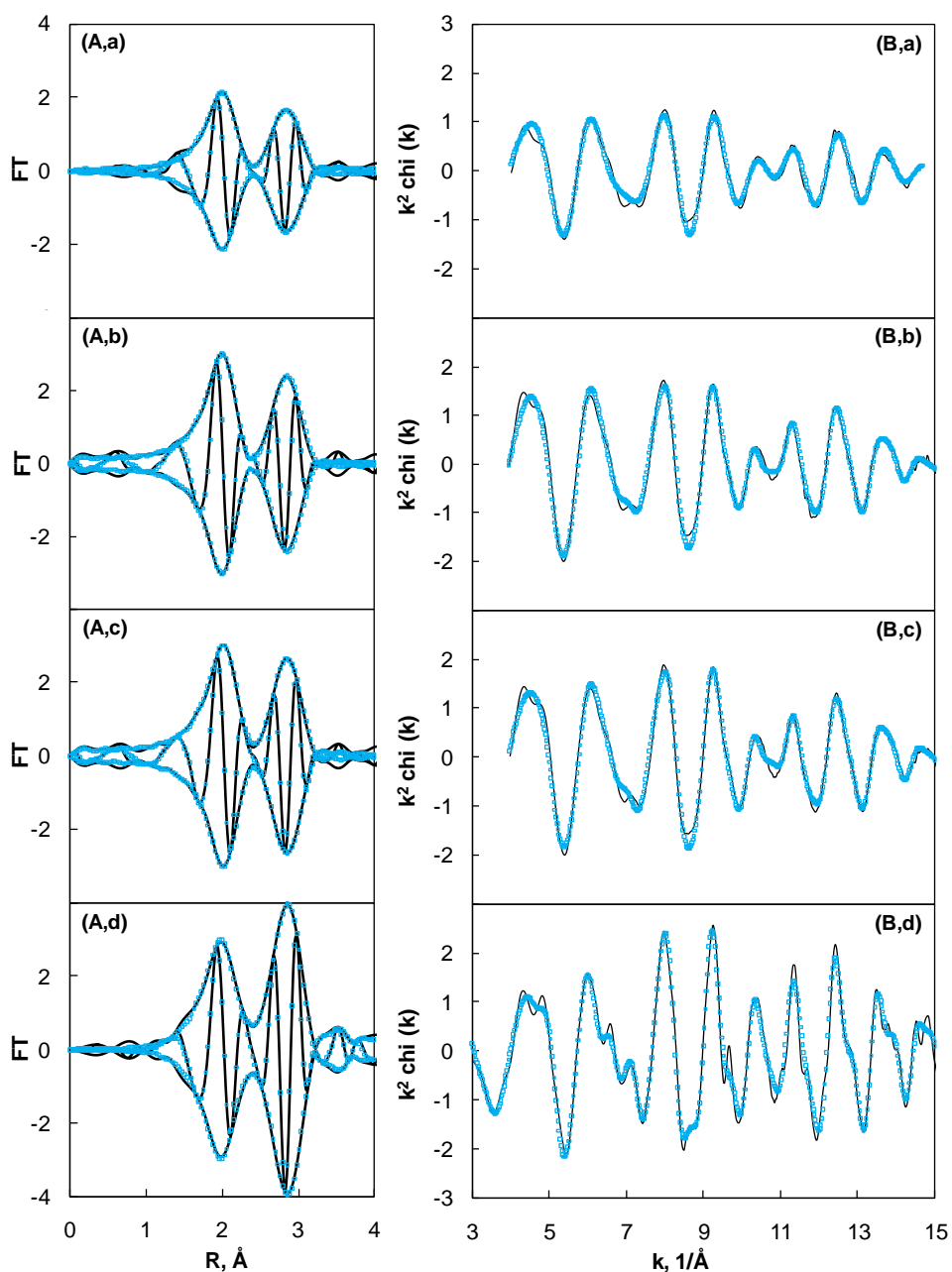


Figure 12. Results for the fitting of the Mo K-edge data of (a) MoS₂/ $\gamma\text{-Al}_2\text{O}_3$, (b) NiMoS/ $\gamma\text{-Al}_2\text{O}_3$, (c) NiMoS/unsupported, and (d) reference MoS₂; (A) k^2 weighted Fourier transform and (B) EXAFS. Fitted data are presented by squares.

Catalyst	Shell	r, Å	N	$\sigma^2, \text{Å}^2$	E_0, eV
MoS ₂ /γ-Al ₂ O ₃	Mo-S	2.41	4.2	0.0036	8.60
	Mo-Mo	3.16	3.2	0.0034	6.99
NiMoS/γ-Al ₂ O ₃	Mo-S	2.41	5.7	0.0034	7.52
	Mo-Mo	3.17	4.7	0.0038	9.22
	Mo-Ni	3.01	0.4	0.0015	-5.71
NiMoS/unsupported	Mo-S	2.41	5.5	0.0031	6.69
	Mo-Mo	3.16	5.2	0.0024	6.90
	Mo-Ni	3.17	0.8	0.0012	19.45
MoS ₂ (reference material)	Mo-S	2.41	6.0	0.0031	9.41
	Mo-Mo	3.16	6.0	0.0026	6.55

Table 6. Fitting results for FT of Mo K-edge $k^2 \chi(k)$ of the sulfided catalysts. N: coordination number, r: distance, E_0 : inner potential, and σ^2 : Debye-Waller factor. EXAFS measurements are carried out at LNT after sulfiding pretreatment.

3.7. Temperature-programmed sulfidation (TPS)

The rate of sulfidation was followed by temperature-programmed reaction (10% H₂S in H₂) increasing the temperature by 5 °C/min. The sulfidation mechanism is governed by oxygen for sulfur exchange reactions leading the transformation from oxide catalyst through the oxy-sulfides, finally to the fully sulfided species. The characteristic profile of H₂S consumption during sulfidation of the NiMo/unsupported catalyst is shown in Fig. 13. In comparison to the supported catalysts, the pattern shape was completely different. Instead of the three characteristic regions, only a continuous consumption of H₂S was detected. The evolution of H₂S (paralleled by H₂ consumption), was not observed probably due to the absence of the support material.

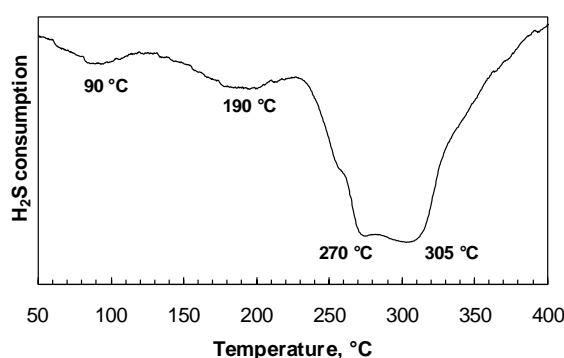


Figure 13. H₂S profile with characteristic temperatures during activation of the NiMo/unsupported catalyst in 10% H₂S in H₂.

As previously published, the terminal Mo=O bonds are the first ones to react and form Mo=S bonds. Therefore the consumption of H₂S observed at 90 and 190 °C could be assigned to two detected crystalline phases, an ammonium nickel molybdate and nickel molybdate, respectively. The intensities of both peaks are low because in the bulk catalyst the most

molybdenum ions are locked in a crystalline structure while only few are accessible at the surface. Further H_2S consumption is due to transformation of the bridging Mo-O-Mo bonds to the new Mo=O terminal and their further sulfidation and reduction. At this point temperatures of 270 and 305 °C are assigned to the molybdenum reduction in an ammonium nickel molybdate and nickel molybdate, respectively, to Mo^{4+} , as confirmed by in-situ Quick EXAFS experiments.

3.8. The HDN of quinoline

3.8.1. The HDN of quinoline as a space time dependent experiment

The HDN reaction network of quinoline is presented in Fig. 14. Quinoline HDN conversion as a function of the space time exhibited non-linear dependency, Fig. 15. At first the rate of nitrogen removal was negligible, but as soon as significant concentration of DHQ was reached the rate increased. The catalyst HDN activity increased in order: $\text{MoS}_2/\gamma\text{-Al}_2\text{O}_3 < \text{NiMoS}/\text{unsupported} < \text{NiMoS}/\gamma\text{-Al}_2\text{O}_3$.

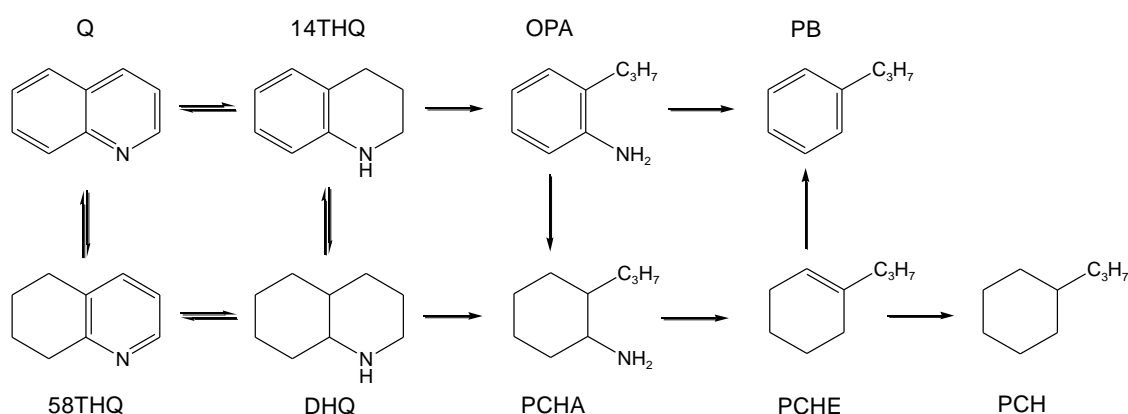


Figure 14. HDN reaction network of quinoline (Q), where following abbreviations are defined as follows:
 14THQ - 1,2,3,4-tetrahydroquinoline
 58THQ - 5,6,7,8-tetrahydroquinoline
 DHQ - decahydroquinoline
 OPA - o-propylaniline
 PCHA – propylcyclohexylamine
 PB – propylbenzene
 PCHE – propylcyclohexene
 PCH - propylcyclohexane.

The effect of the space time on the product distribution is shown in Figs. 16 and 17. At first quinoline was quickly converted to 1,2,3,4-tetrahydroquinoline (14THQ) reaching the equilibrium Fig. 18 (A). Thus the observed primary products, exhibiting the linear correlation with the space time were: 14THQ, 5,6,7,8-tetrahydroquinoline (58THQ), decahydroquinoline (DHQ) and o-propylaniline (OPA).

Further conversion led via the secondary products: propylcyclohexylamine (PCHA) and propylcyclohexene (PCHE) to the final products: propylbenzene (PB) and propylcyclohexane (PCH). Three isomers of propylcyclohexene (PCHE) were detected: 1-propylcyclohexene (with the highest yield according to its highest stability), 3-propylcyclohexene, and propylidene cyclohexane, and were lumped together for further analysis.

The rate of DHQ formation, via hydrogenation of the benzoic ring in 14THQ and the rate of 58THQ formation, via hydrogenation of the benzoic ring in quinoline, was the highest on the NiMoS/ γ -Al₂O₃ and the lowest on the MoS₂/ γ -Al₂O₃ catalyst. Over the whole space time, the conditions were close to the full equilibrium between DHQ and 58THQ, as shown in Fig. 18 (B). Therefore for the further analysis of (quinoline + 14THQ) hydrogenation rate, as well as (DHQ + 58THQ) are lumped together.

The rate of 14THQ ring opening to form OPA increased in the following order: NiMoS/unsupported < MoS₂/ γ -Al₂O₃ < NiMoS/ γ -Al₂O₃. The other ring opening intermediate, PCHA (from DHQ), was either not detected or the yield was very low, < 1% on NiMoS/ γ -Al₂O₃ and < 2.5% on NiMoS/unsupported catalyst. The rate of nitrogen removal from PCHA via Hofmann elimination to PCHE which is hydrogenated to PCH increased in the following order: MoS₂/ γ -Al₂O₃ < NiMoS/unsupported < NiMoS/ γ -Al₂O₃.

In parallel to the HDN of quinoline, the conversion of DBT was also followed on all three catalysts, see Fig. 19. The nickel promoted catalysts exhibited higher HDS activity, i.e., at the space time of 100 h·g_{cat}/mol, the DBT conversion was 12 % on MoS₂/ γ -Al₂O₃, 45% on NiMoS/unsupported, and 90% on NiMoS/ γ -Al₂O₃ catalyst. The product distribution, shown in Fig. 20, indicated that the main route for DBT conversion was the DDS, in which biphenyl (BPh) was mainly formed, Fig. 20 (B). Low yields of phenylcyclohexane (PhCH) were detected over the whole space time: < 2% on MoS₂/ γ -Al₂O₃ and < 8% on NiMoS/ γ -Al₂O₃ and non at NiMoS/unsupported catalyst, Fig. 20 (A).

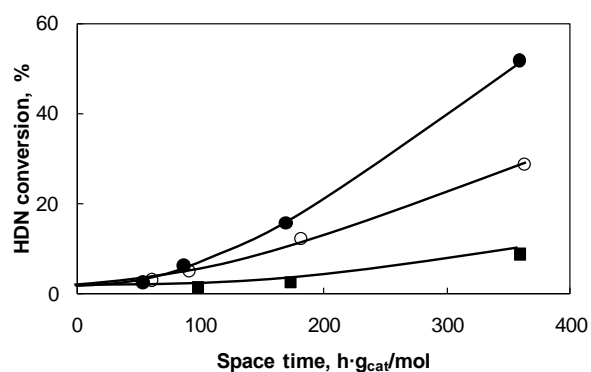


Figure 15. Quinoline HDN conversion as a function of the space time on: (■) MoS₂/ γ -Al₂O₃, (●) NiMoS/ γ -Al₂O₃, and (○) NiMoS/unsupported.

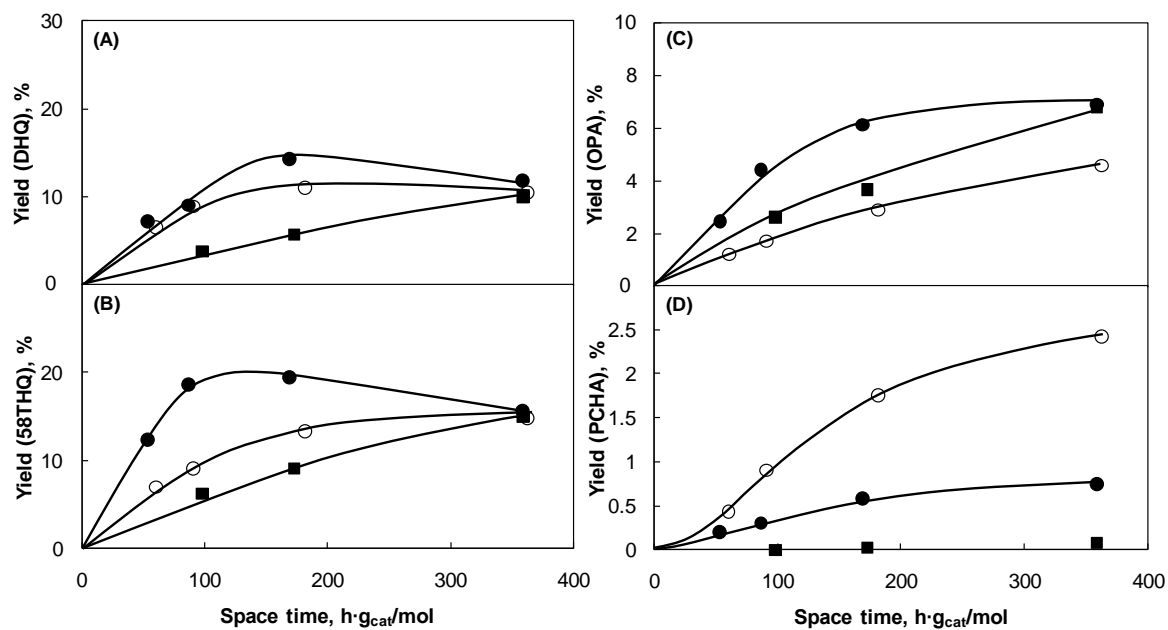


Figure 16. Yield of (A) 58THQ, (B) DHQ, (C) OPA, and (D) PCHA as a function of the space time on: (■) MoS₂/γ-Al₂O₃, (●) NiMoS/γ-Al₂O₃, and (○) NiMoS/unsupported.

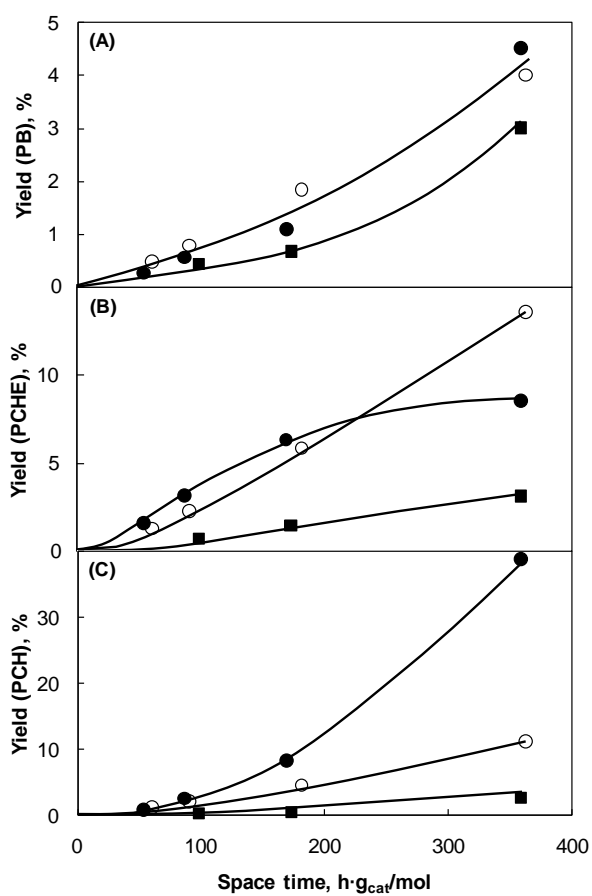


Figure 17. Yield of (A) PB, (B) PCHE, and (C) PCH as a function of the space time on: (■) MoS₂/γ-Al₂O₃, (●) NiMoS/γ-Al₂O₃, and (○) NiMoS/unsupported catalyst.

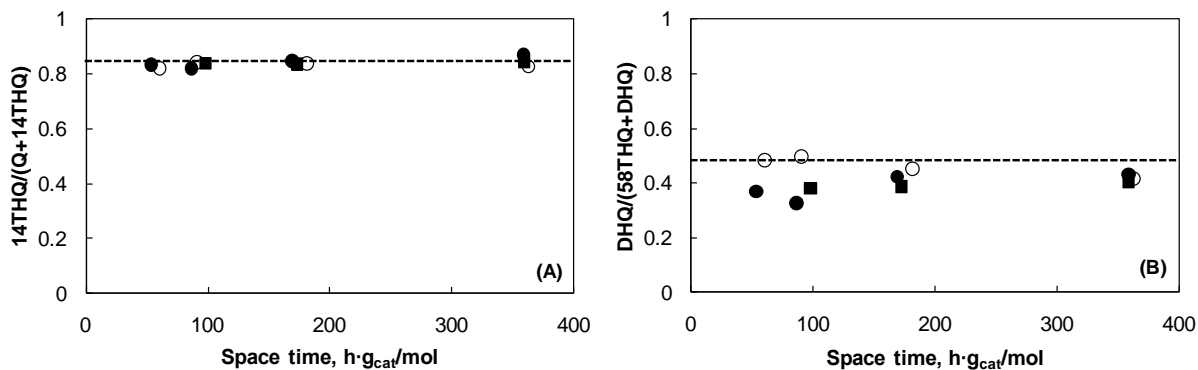


Figure 18. Equilibrium (dotted line) between: quinoline and 14THQ (A) and DHQ and 58THQ (B), when quinoline HDN is carried out at 370 °C and 5 MPa on MoS₂/γ-Al₂O₃ (■), NiMoS/γ-Al₂O₃ (●), and NiMoS/unsupported catalyst (○) in the presence of 3.4 kPa DBT.

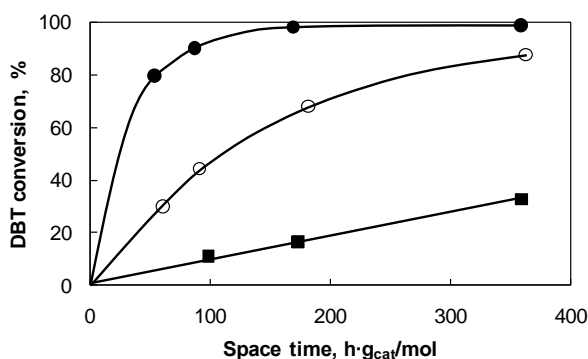


Figure 19. DBT conversion as a function of space time in the parallel reaction with the HDN of quinoline, carried out on: (■) MoS₂/γ-Al₂O₃, (●) NiMoS/γ-Al₂O₃, and (○) NiMoS/unsupported catalyst.

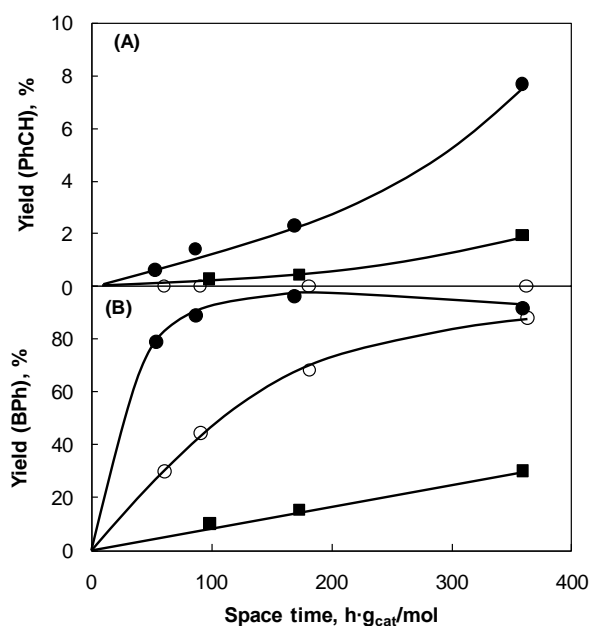


Figure 20. The yield of PhCH (A) and BPh (B) as a function of space time in the parallel HDS of DBT and HDN of quinoline, carried out on: (■) MoS₂/γ-Al₂O₃, (●) NiMoS/γ-Al₂O₃, and (○) NiMoS/unsupported catalyst.

3.8.2. The HDN of quinoline as a temperature dependent experiment

The quinoline HDN conversion as a function of temperature exhibits an S-shaped dependency, as shown in Fig. 21. At 290 °C, the conversion to nitrogen free products did not occur. The only observed products were 14THQ and DHQ from subsequent hydrogenation. At 330 °C further products were observed: 58THQ (hydrogenation), OPA and PCHA (ring opening) and nitrogen-free products PCHE, PCH and PB. The product distribution as a function of reaction temperature is presented in Figs. 22 and 23.

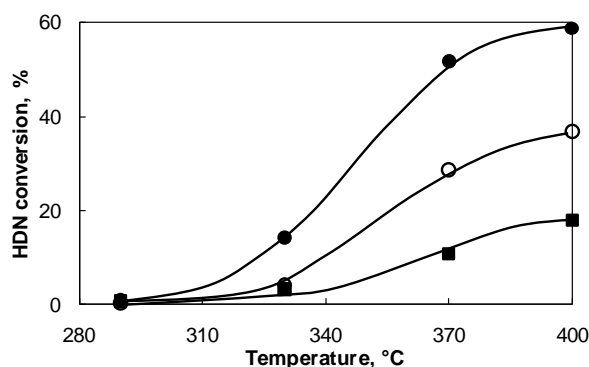


Figure 21. Quinoline HDN conversion as a function of the temperature on: (■) MoS₂/γ-Al₂O₃, (●) NiMoS/γ-Al₂O₃, and (○) NiMoS/unsupported.

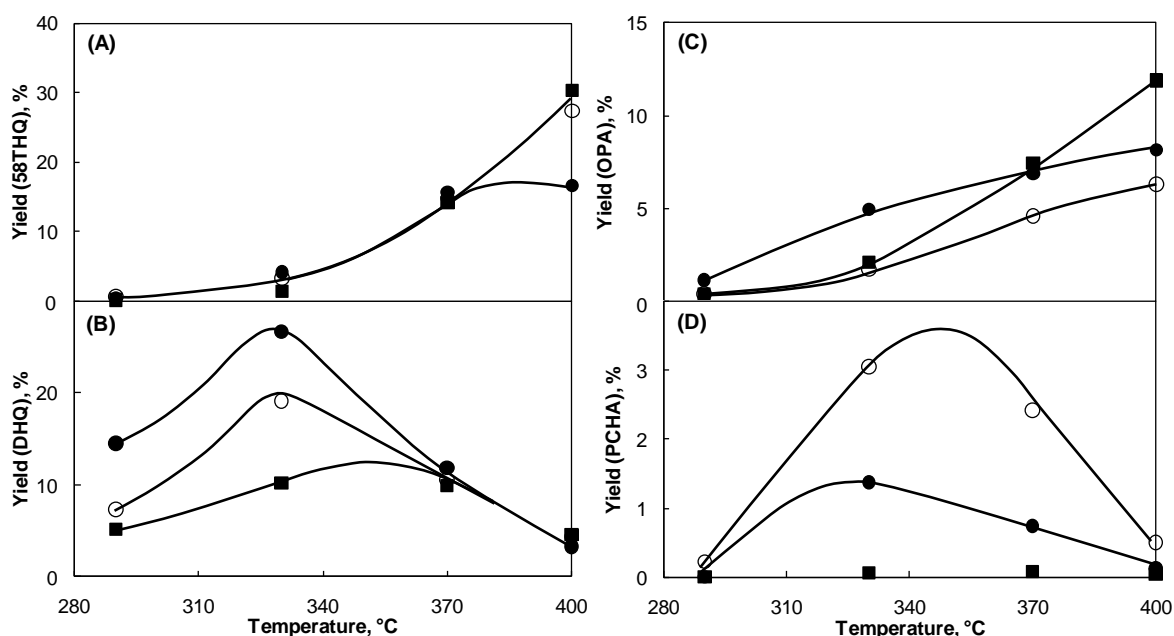


Figure 22. Yield of (A) 58THQ, (B) DHQ, (C) OPA, and (D) PCHA as a function of the temperature on: (■) MoS₂/γ-Al₂O₃, (●) NiMoS/γ-Al₂O₃, and (○) NiMoS/unsupported catalyst.

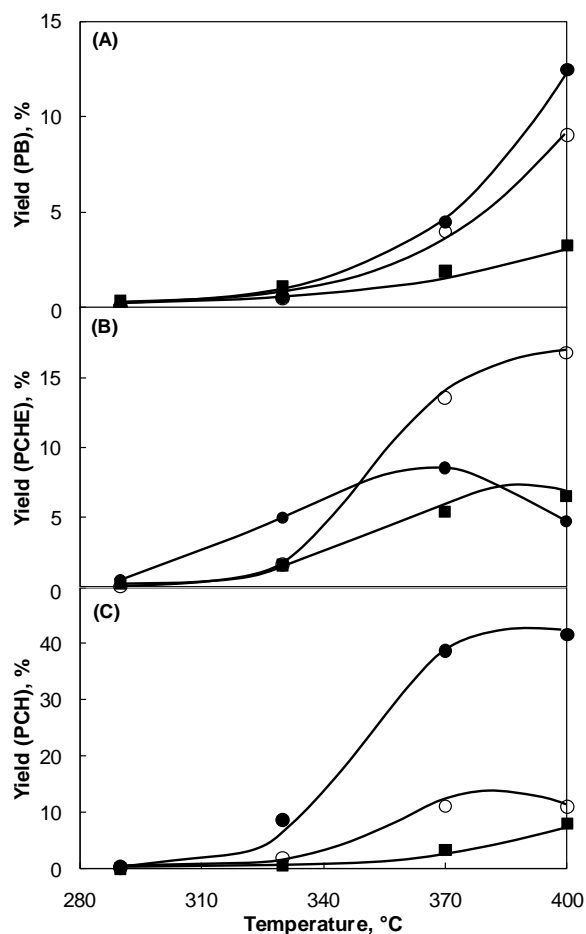


Figure 23. Yield of (A) PB, (B) PCHE, and (C) PCH as a function of the temperature on: (■) MoS₂/γ-Al₂O₃, (●) NiMoS/γ-Al₂O₃, and (○) NiMoS/unsupported.

The thermodynamic equilibrium between quinoline and 14THQ was reached at all temperatures studied, as seen in Fig. 24 (A) where the aromatics are favored at higher temperatures. The equilibrium constant ($K' = K_p \cdot p_{H_2}^2$), is shown as the reciprocal function of the temperature for all three catalysts, Fig. 24 (A). Applying the Van't Hoff equation:

$$\frac{d \ln K_p}{d(1/T)} = -\frac{\Delta H}{R}$$

$$\ln K_p = -\frac{\Delta H}{RT} + \frac{\Delta S}{R}$$

where K_p is the conventional equilibrium constant, T is the temperature (K), ΔH is the heat of the reaction in (J/mol), ΔS is the entropy of the reaction (J/(mol K)), and R is the gas constant (8.314 J/(mol K)), a linear correlation was obtained, as shown in Fig. 24 (B):

$$K_p = \frac{12354}{T} - 25.28$$

The heat of the equilibrium reaction was calculated to be 102.7 kJ/mol.

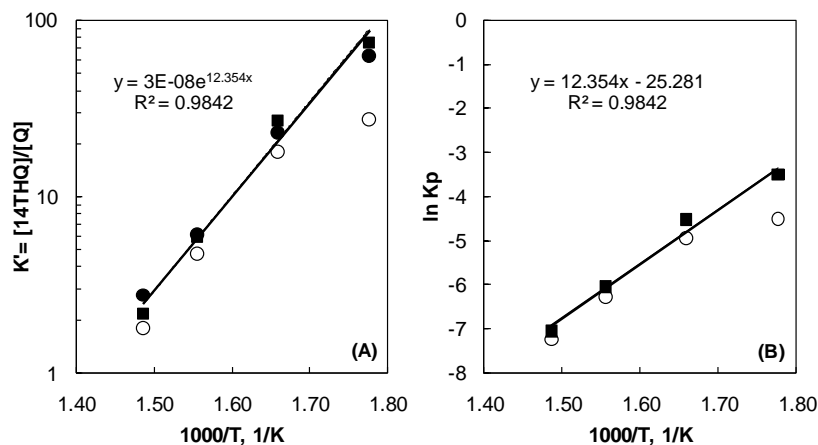


Figure 24. The ratio of 14THQ and quinoline (A) and the natural logarithm of the K_p (B) as a function of the reciprocal of the temperature at 5 MPa. Different assignments were used for the reactions carried out on: (■) $\text{MoS}_2/\gamma\text{-Al}_2\text{O}_3$, (●) $\text{NiMoS}/\gamma\text{-Al}_2\text{O}_3$, and (○) $\text{NiMoS}/\text{unsupported}$.

The product distribution was shifted through hydrogenated, ring opening and finally towards the nitrogen free products with increasing the reaction temperature. The yield of 58THQ (product of the benzoic ring hydrogenation) exhibited maximum at around 380 °C (20%) only on the $\text{NiMoS}/\gamma\text{-Al}_2\text{O}_3$ catalyst. The $\text{NiMoS}/\text{unsupported}$ and $\text{MoS}_2/\gamma\text{-Al}_2\text{O}_3$ catalysts showed an increase of the yield as a function of temperature reaching 30% at 400 °C, Fig. 22 (A). Fully hydrogenated DHQ showed maximum yield at around 330 °C on $\text{NiMoS}/\gamma\text{-Al}_2\text{O}_3$ (27%) and $\text{NiMoS}/\text{unsupported}$ (20%) catalysts, while $\text{MoS}_2/\gamma\text{-Al}_2\text{O}_3$ revealed later maximum at around 350 °C (12%), Fig. 22 (B). While the OPA yield increased with increasing the temperature, PCHA yield exhibited maximum at around 330 °C (1.5%) on $\text{NiMoS}/\gamma\text{-Al}_2\text{O}_3$ and at around 350 °C (3.5%) on $\text{NiMoS}/\text{unsupported}$ catalyst, Fig. 22 (C) and (D). The conversion to nitrogen free products began at 330 °C. PB showed the increase of yield as a function of temperature reaching 3.3, 8.5, and 12.5% on $\text{MoS}_2/\gamma\text{-Al}_2\text{O}_3$, $\text{NiMoS}/\text{unsupported}$, and $\text{NiMoS}/\gamma\text{-Al}_2\text{O}_3$ catalyst, respectively, Fig. 23 (A). PCHE exhibited the maximum yield at 370 °C on $\text{NiMoS}/\gamma\text{-Al}_2\text{O}_3$ catalyst (8.5%), while an S-shaped dependency was observed on $\text{MoS}_2/\gamma\text{-Al}_2\text{O}_3$ and $\text{NiMoS}/\text{unsupported}$ catalysts, reaching 7% and 17% at 400 °C, respectively, Fig. 23 (B). The PCH yield increased as a function of temperature on all three studied catalysts, reaching the maximum of 8.1, 10, and 41.6% on $\text{MoS}_2/\gamma\text{-Al}_2\text{O}_3$, $\text{NiMoS}/\text{unsupported}$ and $\text{NiMoS}/\gamma\text{-Al}_2\text{O}_3$ catalysts, respectively, Fig. 23 (C).

In parallel to the HDN of quinoline, the conversion of DBT was also followed on all three catalysts, Fig. 25. The DBT conversion increased from 5 (at 290 °C) to 43% (at 400 °C) at $\text{MoS}_2/\gamma\text{-Al}_2\text{O}_3$ catalyst, and from 32 (at 290 °C) to 90% (at 400 °C) on $\text{NiMoS}/\text{unsupported}$ catalyst. On $\text{NiMoS}/\gamma\text{-Al}_2\text{O}_3$ catalyst the DBT conversion reached the maximum 100%

already at 330 °C. The product distribution, shown in Fig. 26, indicated that the yield of hydrogenated product, PhCH, increased with increasing the reaction temperature, Fig. 26 (A), reaching 4% on MoS₂/γ-Al₂O₃, 7% on NiMoS/unsupported, and 12% on NiMoS/γ-Al₂O₃ catalyst.

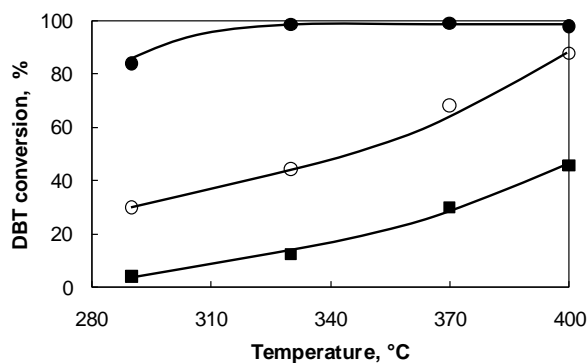


Figure 25. DBT conversion as a function of temperature in the parallel reaction with the HDN of quinoline, carried out on: (■) MoS₂/γ-Al₂O₃, (●) NiMoS/γ-Al₂O₃, and (○) NiMoS/unsupported catalyst.

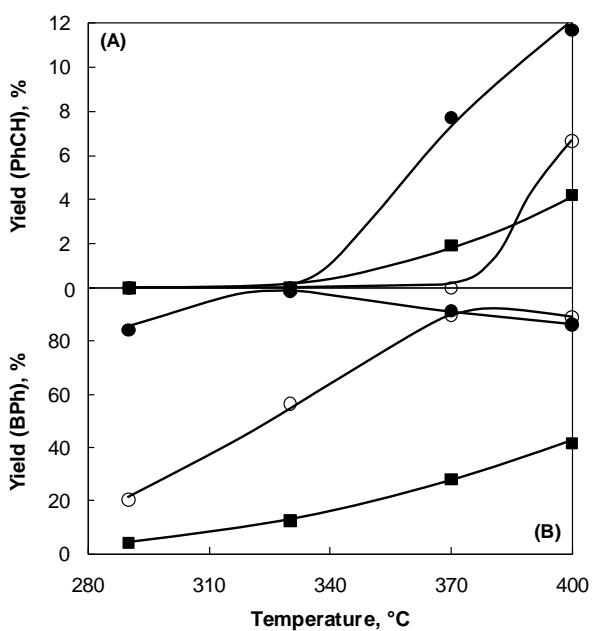


Figure 26. The yield of PhCH (A) and BPh (B) as a function of temperature in the parallel HDS of DBT and HDN of quinoline, carried out on: (■) MoS₂/γ-Al₂O₃, (●) NiMoS/γ-Al₂O₃, and (○) NiMoS/unsupported catalyst.

4. Discussion

4.1. Catalyst characterization

The molybdenum structure in the supported Mo/γ-Al₂O₃ and NiMo/γ-Al₂O₃ oxide catalyst precursors strongly depends on the pH of the impregnation solution and the molybdenum concentration. The isoelectric point (IEP) of γ-Al₂O₃ is known to be around pH 8 [25], thus

aqueous solution of ammonium heptamolybdate (pH 5.5) provides positively charged surface of the γ -Al₂O₃ support ensuring the stabilization of the negative charged molybdenum heptaanions via formation of Al-O-Mo bonds. The molybdenum concentration of 2.5 Mo atoms/nm² is far below the concentration needed for the full monolayer coverage of γ -Al₂O₃ (4.6-5 atoms/nm²) [16]. XRD patterns do not exhibit reflections of any Mo-containing crystalline structure, Fig. 1 (f) and (g), and the Raman spectra imply the existence of the well dispersed polymolybdate species [26-30], Fig. 4 (e) and (f). Neither the presence of the isolated MoO₄ tetrahedra nor the crystalline MoO₃ was observed, due to the absence of the characteristic Raman bands at 896, 846, and 318 cm⁻¹ [31] and 996, 821, 667, and 377 cm⁻¹ (Table 3), respectively. Due to the presence of nickel, Raman band assigned to the terminal Mo=O symmetric vibration shifted from 961 to 947 cm⁻¹ and the intensity of the shoulder at around 860 cm⁻¹ increased, indicating the formation of new Mo-O-Ni bonds [32,33]. The creation of new bridged bonds occurs either from the terminal Mo=O or by breaking Al-O-Mo bonds with γ -Al₂O₃ support. The molybdenum-oxygen bond distances and bond orders are determined using the model of Hardcastle and Wachs [34]. Raman band at 961 cm⁻¹ is correlated to the bond length of 1.71 Å with a bond order of 1.7, while the band at 360 cm⁻¹ is correlated to the bond length of 2.16 Å with a bond order of 0.35 for Mo/ γ -Al₂O₃ catalyst. A good agreement is found between Raman and EXAFS data. The EXAFS analysis defined the existence of six oxygen nearest neighbors; four at short (1.72 Å) and two at long distances (2.12 Å). Furthermore, the presence of the characteristic pre-edge peak in Mo K-edge XANES (at 19995 eV), indicates that Mo is in distorted octahedral coordination, Fig. 8 (A,f) [35,36]. The Mo-Mo distance of 3.27 Å defines the Mo-O-Mo bond angle of 100° that implies a formation of a very tense structure due to the strong interaction with γ -Al₂O₃ support. Therefore, Mo⁶⁺ exhibits two free terminal Mo=O bonds and two Mo-O bonds used for the interaction with the support which tend to be tetrahedrally coordinated around Mo⁶⁺, and the last two Mo-O at the longer distances for bridging connections which complete the octahedra [28,37,38]. After nickel impregnation the EXAFS analysis of the Mo K-edge indicated the existence of four short Mo-O bonds (at 1.72 Å) and two long at (1.98 Å). The equal number of the short Mo-O and long bridging bonds as found in Mo/ γ -Al₂O₃ oxide catalyst precursor indicates that the formation of Mo-O-Ni did not occur from the terminal Mo=O groups, but from Mo-O-Al groups. Thus nickel induces weaker interaction of the oxidic precursor with γ -Al₂O₃ support, causing the structure relaxation seen from the larger Mo-Mo distance (3.38 Å) and Mo-O-Mo bond angle (116°).

NiMo/unsupported oxide catalyst precursor presents a mixture of nickel molybdate (NiMoO₄), and an ammonium nickel molybdate ((NH₄)₂Ni₂(OH)₂(MoO₄)₂), see XRD pattern

in Fig. 1 (b) and Raman spectrum in Fig. 4 (c). The determined metal ratio (Ni/Mo) of 1.07 (Table 1) matched well with the ratio in the molecular formula of the found structures. XANES of Mo K-edge exhibit high pre-edge feature characteristic for the tetrahedral molybdenum species, Fig. 8 (A,h). UV-vis spectrum exhibited two features assigned to octahedral coordinated Ni^{2+} (ammonium nickel molybdate) and tetrahedral coordinated Ni^{2+} (nickel molybdate), Fig. 7 (h). Therefore, an ammonium nickel molybdate is described as a layered structure of distorted nickel octahedra and molybdenum tetrahedra which are bonded with hydrogen to form layers in c-direction [12].

Both supported $\text{Mo}/\gamma\text{-Al}_2\text{O}_3$ and $\text{NiMo}/\gamma\text{-Al}_2\text{O}_3$ catalysts showed a profile with three sections (Fig. 5, Chapter 2) during the temperature-programmed sulfidation (10% H_2S in H_2 mixture). In the low temperature sulfiding oxygen is substituted by sulfur, as seen by H_2S consumption in TPS profile and a decrease of the shortest Mo-O followed by the formation of new Mo-S contribution in Quick EXAFS, Fig. 10. The terminal Mo=O bonds are the most reactive in polymolybdate-like structure and therefore will be the first one to form oxy-sulfidic species [39,40]. In the second section, molybdenum is reduced from Mo^{6+} to Mo^{4+} , indicated by H_2S release and H_2 consumption in TPS profile and the disappearance of the pre-edge feature in Quick EXAFS. The reduction temperature is shifted from 225 ($\text{Mo}/\gamma\text{-Al}_2\text{O}_3$) to 205 °C ($\text{NiMo}/\gamma\text{-Al}_2\text{O}_3$) due to the presence of nickel promoter [9], that causes weaker interaction of the oxide precursor with $\gamma\text{-Al}_2\text{O}_3$ support and easier H_2 dissociation. The following third region, high temperature sulfiding, is characteristic for further H_2S consumption and formation of new Mo-Mo contribution at the larger distance, indicating the further conversion to the final $\text{MoS}_2/\gamma\text{-Al}_2\text{O}_3$ and $\text{NiMoS}/\gamma\text{-Al}_2\text{O}_3$ catalysts.

On the contrary, $\text{NiMo}/\text{unsupported}$ catalyst exhibited a continuous H_2S consumption over the temperature range; H_2S release was not observed due to the absence of support interaction, Fig. 13. Low temperature H_2S consumption is assigned to a sulfidation of the accessible molybdenum ions located at the surface of the bulk structure. Further H_2S consumption is due to a sulfidation of the molybdenum ions locked inside a crystalline structure. The temperatures of 270 and 305 °C are assigned to the molybdenum reduction to Mo^{4+} in an ammonium nickel molybdate and nickel molybdate, respectively, as confirmed by the Quick EXAFS, Fig. 10.

Sulfided catalysts, as shown in Raman spectra of Fig. 6, revealed the presence of the typical MoS_2 phase. Supported $\text{MoS}_2/\gamma\text{-Al}_2\text{O}_3$ and $\text{NiMoS}/\gamma\text{-Al}_2\text{O}_3$ catalysts exhibited high dispersion of the sulfide phase indicated by the absence of the diffraction peak at $14^\circ 2\theta$, Fig. 2 (c) and (d). TEM micrographs confirmed the average MoS_2 stacking degree of two and slabs length below 10 nm, Fig. 2 in Chapter 2. The formation of Ni sulfides was not observed. On the

contrary, NiMoS/unsupported catalyst exhibits higher stacking degree of approximately seven, as calculated from the diffraction peak at $14^\circ 2\theta$, Fig. 2 (e) and TEM micrograph, Fig. 3 (B). Higher stacking degree is a direct consequence of the absence of support. Slab length was between 15 and 20 nm. Furthermore, separated Ni_3S_2 phase is detected, as seen in XRD.

The concentration of the accessible metal cations, i.e., CUS, in alumina supported sulfided catalysts was $65 \mu\text{mol}/g_{\text{cat}}$ for $\text{MoS}_2/\gamma\text{-Al}_2\text{O}_3$ and $80 \mu\text{mol}/g_{\text{cat}}$ for NiMoS/ $\gamma\text{-Al}_2\text{O}_3$ catalyst indicating that the presence of Ni enhanced their concentration by approximately 25%. On the contrary, the NiMoS/unsupported catalyst due to the lack of the support the concentration of CUS was $33 \mu\text{mol}/g_{\text{cat}}$.

4.2. The HDN of quinoline

The quinoline HDN reaction proceeds via hydrogenation of quinoline pyridinic ring to form 14THQ and further hydrogenation of 14THQ benzoic ring to form DHQ. The reaction can then continue via two routes, i.e., the ring opening of 14THQ to OPA and of DHQ to PCHA, and then finally nitrogen is removed via $\text{C}(\text{sp}^2)\text{-N}$ and $\text{C}(\text{sp}^3)\text{-N}$ bond cleavage to form PB and PCHE, respectively, see Fig. 14. The rate of nitrogen removal strongly depends on the reaction temperature and it exhibits an S-shaped dependency, Fig. 21. At 290°C only hydrogenation to 14THQ and DHQ occurs, while at 330°C the first ring opening and nitrogen-free products are observed, see Figs. 22 and 23. Further temperature raise to 370°C strongly increases the rate of nitrogen removal, after which the rate stays almost constant. The reason of the plateau in the nitrogen removal is the quinoline-14THQ thermodynamic equilibrium. The equilibrium is shifted towards unsaturated quinoline at high temperatures, as shown in Fig. 24 and predicted by the estimation of Cocchetto and Satterfield [41].

At 370°C , the nitrogen removal is at first negligible, until a significant amount of 14THQ has been converted to DHQ after which the rate increases, Fig. 15. The initially low rate is a direct consequence of the inhibition by 14THQ that is stronger adsorbed on the catalyst surface than quinoline [42].

The ring opening of 14THQ, via the $\text{C}(\text{sp}^3)\text{-N}$ bond cleavage to form OPA, has lower reaction rate compared to the parallel hydrogenation of the benzoic ring to form DHQ, Fig. 16 (A) and (C). Further hydrogenation of OPA to PCHA is negligible as long as quinoline, 14THQ, 58THQ and DHQ are present, because of their strong adsorption on the catalyst surface [43-46]. Thus, the hydrogenation of the phenyl ring in OPA is the rate determining step in the following sequence: quinoline \rightarrow 14THQ (via hydrogenation) \rightarrow OPA (via ring opening) \rightarrow

PCHA (via denitrogenation). OPA can be also converted to PB via the direct denitrogenation (DDN) route that is suppressed by Ni in the catalyst and the presence of DBT [9]. On the other hand, the HDN of DHQ proceeds via the following sequence: DHQ → PCHA (via ring opening) → PCHE (via denitrogenation) → PCH (via hydrogenation), where the C(sp³)-N bond cleavage in the primary amine (PCHA) is fast and the rate of the C(sp³)-N bond cleavage in DHQ is the rate limiting step [47]. Finally the main route for the nitrogen removal is proposed as follows: quinoline → 14THQ → DHQ → PCHA → PCHE → PCH.

At this point we will attempt to address the HDN activity to the defined catalyst morphology going from well dispersed supported MoS₂/γ-Al₂O₃ and NiMoS/γ-Al₂O₃ catalysts to multi-stacked NiMoS/unsupported catalyst. It has been shown that the promoted NiMoS/γ-Al₂O₃ catalyst is superior in the nitrogen removal compared to its “parent” MoS₂/γ-Al₂O₃ catalyst in the whole temperature range, Fig 15. This observation goes well with the previous believes that upon addition of Ni cations, Mo cations are substituted at the edge positions of the MoS₂ slabs creating new and more active catalytic sites for the HDN [48]. New sulfur vacancies (CUS) are formed, due to the decrease in sulfur binding energy [49]. Dramatic enhancement in the activity of brim sites, electron rich zones on the basal plane associated with metal-like states [50,51], responsible for the hydrogenation of the OPA phenyl ring, has been reported [9].

After the equilibrium between quinoline and 14THQ is reached, the next step in the HDN reaction is the hydrogenation of the benzoic ring in quinoline (to form 58THQ) and in 14THQ (to form DHQ). The products, DHQ and 58THQ, are almost fully equilibrated over the whole space time, Fig. 18 (B). Therefore their yields should be considered together to understand the hydrogenation rate of different catalysts.

The promoted NiMoS/γ-Al₂O₃ catalyst exhibits higher hydrogenation rate than the “parent” MoS₂/γ-Al₂O₃ catalyst; 18 mol% 58THQ + 12 mol% DHQ compared to 5 mol% 58THQ + 3 mol% DHQ, at 100 h·g_{cat}/mol, see Fig. 16 (A) and (B). The higher yield is assigned to the promotion of the brim sites electron density by Ni, as reported in case of phenyl ring hydrogenation of OPA [9]. If this holds true, higher MoS₂ stacking degree would result in a lower hydrogenation rate, because the brim sites are found only on the top of the stacked layers. In fact, multi stacked NiMoS/unsupported catalyst exhibits lower hydrogenation rate than the supported NiMoS/γ-Al₂O₃ counterpart, 8 mol% 58THQ + 8 mol% DHQ, at 100 h·g_{cat}/mol, see Fig. 16 (A) and (B). Higher catalyst dispersion, i.e., lower stacking degree is the key factor responsible for the hydrogenation. Hydrogenation sites for alkenes were previously related to the high dispersion of sulfide phase that was directly correlated to the

high dispersion of NiMo oxidic precursor depending on the support used, e.g. ASA, γ -Al₂O₃ support [52-54].

Turning now to the ring opening reaction via C(sp³)-N bond cleavage in DHQ, to form PCHA that is immediately converted to PCHE via Hofmann-type elimination (the HDN reaction is carried out at relatively high reaction temperature and pressure and low DBT partial pressure), it is shown that the rate increases in the following order: MoS₂/ γ -Al₂O₃ < NiMoS/unsupported < NiMoS/ γ -Al₂O₃ catalyst, see Fig. 17 (B); PCHE is considered to be kinetically primary product. The Hofmann-type elimination requires an acid site, for the nitrogen atom quaternization, and a basic site, for the removal of a β -H atom. The dual site consists of -SH groups with acid character (formed on S²⁻ dimers by reacting with hydrogen), located close to the brim sites of sulfide slabs, and basic S²⁻ ions [55].

The increase in the ring opening rate from MoS₂/ γ -Al₂O₃ to NiMoS/ γ -Al₂O₃ catalyst is attributed to a promotion by Ni that facilitates H₂ dissociation, providing higher concentration of -SH groups and it increases the basicity of S²⁻ ions, facilitating the β -H atom removal. The question that arises here is whether the dual sites are located only at the rim sites, in the vicinity of the brim sites (only top layer), or also at the edge sites of sulfide slabs (middle layers), as defined by Daage and Chianelli [52]. If both, one would expect the increase in the rate of the ring opening with higher stacking degree. On the contrary, it is shown that multi-stacked NiMoS/unsupported catalyst exhibit lower ring opening activity than well dispersed NiMoS/ γ -Al₂O₃ catalyst. The observation would lead to a conclusion that only the sites in the vicinity of the brim sites are active. This would hold true only if the slab diameter in both catalysts would be the same. From the previous analysis it is shown that the NiMoS/unsupported catalyst exhibit much larger slab diameter (between 15 and 20 nm) than the supported counterpart (10 nm), therefore it is not straightforward to conclude that only the sites on the top layer are active, thus that the higher stacking leads to lower number of the active sites.

Turning to the HDS of DBT, it is shown that the main pathway proceeds via the DDS route. The direct sulfur removal occurs via sulfur σ -bonding on the sulfur vacancies (CUS) that act as electron withdrawing sites. Therefore a higher concentration of such coordinatively unsaturated sites should enhance the rate of the HDS reaction. For the materials studied, that concentration of accessible Lewis acid sites at the perimeter of the sulfide slabs increases as follows: NiMoS/unsupported < MoS₂/ γ -Al₂O₃ < NiMoS/ γ -Al₂O₃. Despite the higher CUS concentration on MoS₂/ γ -Al₂O₃, NiMoS/unsupported exhibited higher HDS rate. Higher rate suggests that the intrinsic rate constant of that reaction increased due to faster regeneration of active sites in the presence of H₂. Nickel lowers the sulfur binding energy,

thus CUS are easier created [47,49]. On the other hand the HDS rate on NiMoS/ γ -Al₂O₃ is higher than on NiMoS/unsupported catalyst which is related to the higher CUS concentration on the former.

5. Conclusion

The supported Mo/ γ -Al₂O₃ oxide catalyst precursor exhibited well dispersed amorphous polymolybdate structure. Distorted octahedral Mo formed a very rigid structure due to the strong interaction with γ -Al₂O₃ support. The characterization of the NiMo/ γ -Al₂O₃ oxide catalyst precursor indicated weaker interaction with the support and structure relaxation as new Mo-O-Ni bonds were formed after the breaking of Al-O-Mo bonds. NiMo/unsupported oxide catalyst precursor exhibited a mixture of nickel molybdate, and an ammonium nickel molybdate crystalline phase that is described as a layered structure of distorted nickel octahedra and molybdenum tetrahedra, bonded with hydrogen to form layers in c-direction.

Supported MoS₂/ γ -Al₂O₃ and NiMoS/ γ -Al₂O₃ catalysts exhibited high dispersion of the sulfide phase with the average MoS₂ stacking degree of two and slabs length of 10 nm. On the contrary, NiMoS/unsupported catalyst exhibited higher stacking degree, of approximately seven and slabs length between 15 and 20 nm. This diverse morphology led to different CUS concentrations. The presence of Ni enhanced the CUS concentration in the supported catalyst due to lower sulfur binding energy in the presence of Ni. On the contrary, lower CUS concentration on NiMoS/unsupported catalyst is a direct consequence of higher stacking degree.

The main route for the nitrogen removal in the quinoline HDN is: quinoline → 14THQ (via equilibrium) → DHQ (via hydrogenation) → PCHA (ring opening via C(sp³)-N bond cleavage) → PCHE (Hofmann-type elimination via C(sp³)-N bond cleavage) → PCH (via hydrogenation). The nitrogen removal was at first negligible, until a significant amount of 14THQ has been converted to DHQ after which the rate increases. The ring opening of DHQ is the rate determining in this route, while further nitrogen removal is very fast.

NiMoS/ γ -Al₂O₃ catalyst exhibited higher hydrogenation rate than the “parent” MoS₂/ γ -Al₂O₃ catalyst due to the promotion of the brim sites electron density by Ni. Multi-stacked NiMoS/unsupported catalyst exhibited lower hydrogenation rate than the supported NiMoS/ γ -Al₂O₃ counterpart. Higher catalyst dispersion, i.e., lower stacking degree was concluded to be the key factor responsible for the hydrogenation of the benzoic ring. The ring opening that proceeds via Hofmann-type elimination requires an acid –SH and basic S²⁻ site. Increase in the ring opening rate from MoS₂/ γ -Al₂O₃ to NiMoS/ γ -Al₂O₃ catalyst is because Ni facilitates H₂ dissociation and it increases the basicity of S²⁻ ions. It was shown

that multi-stacked NiMoS/unsupported catalyst exhibit lower ring opening activity than well dispersed NiMoS/ γ -Al₂O₃ catalyst.

The HDS rate increased in the following order: MoS₂/ γ -Al₂O₃ < NiMoS/unsupported < NiMoS/ γ -Al₂O₃. Despite the higher CUS concentration on MoS₂/ γ -Al₂O₃, NiMoS/unsupported exhibited higher intrinsic rate constant of that reaction due to faster regeneration of active sites. On the other hand higher rate on NiMoS/ γ -Al₂O₃ is due to higher CUS concentration than on NiMoS/unsupported catalyst.

6. Acknowledgements

This work was supported by Chevron Energy Technology Company. The authors would like to thank Dr. Alexander Kuperman and Dr. Axel Brait for fruitful discussions. The authors are also grateful to Dr. Marianne Hanzlik for the TEM measurements, and the staff of the beamline X1 at Hasylab DESY, Hamburg, Germany for their kind help and continuous support during the experiments.

7. References

- [1] F. Besenbacher, M. Brorson, B.S. Clausen, S. Helveg, B. Hinnemann, J. Kibsgaard, J.V. Lauritsen, P.G. Moses, J.K. Nørskov, H. Topsøe, *Catal. Today* 130 (2008) 86.
- [2] R. Prins, V.H.J. de Beer, G.A. Somorjai, *Catal. Rev. Sci. Eng.* 31 (1989) 1.
- [3] H. Topsøe, *Appl. Catal. A* 322 (2007) 3.
- [4] J.V. Lauritsen, M. Nyberg, J.K. Nørskov, B.S. Clausen, H. Topsøe, E. Laegsgaard, F. Besenbacher, *J. Catal.* 224 (2004) 94.
- [5] M. Daage, R.R. Chianelli, *J. Catal.* 149 (1994) 414.
- [6] X. Li, A. Wang, M. Egorova, R. Prins, *J. Catal.* 250 (2007) 283.
- [7] B.S. Clausen, H. Topsøe, R. Candla, J. Villadsen, B. Lengeler, J. Als-Nielsen, F. Christensen, *J. Phys. Chem.* 85 (1981) 3868.
- [8] T. Maesen, A. E. Kuperman, US 2009/0107883 A1.
- [9] A. Hrabar, J. Hein, O.Y. Gutiérrez, J.A. Lercher, *J. Catal.* In Press, Available online 17 June 2011.
- [10] A.L. Ankudinov, J.J. Rehr, *Phys. Rev. B* 62 (2000) 2437.
- [11] F. Mauge, J. Lamotte, N.S. Nesterenko, O. Manoilova, A.A. Tsyganenko, *Catal. Today* 70 (2001) 271.
- [12] D. Levin, S. Soled, J. Ying, *Inorg. Chem.* 35 (1996) 4191.
- [13] R.W.G. Wyckoff, *Crystal Structures*, 1 (1963) 280, Second edition. Interscience Publishers, New York, New York.
- [14] F. Pedraza, J. Cruz-Reyes, D. Acosta, M.J. Yañez, M. Avalos-Borja, S. Fuentes, *J. Phys. Condens. Matter.* 5 (1993) A219.
- [15] G. Mestl, T.K.K. Srinivasan, *Catal. Rev. Sci. Eng.* 40 (1998) 451.
- [16] I.E. Wachs, *Catal. Today* 27 (1996) 437.
- [17] A. Guevara-Lara, R. Bacaud, M. Vrinat, *Appl. Catal. A* 328 (2007) 99.
- [18] J.L. Verble, T.J. Wieting, *Phys. Rev. Letters* 25 (1970) 362.
- [19] T.J. Wieting, J.L. Verble, *Phys. Rev. B* 3 (1971) 4286.
- [20] M. Houalla, B. Delmon, *J. Phys. Chem.* 84 (1980) 2194.
- [21] P. Salerno, S. Mendioroz, A. Lopez Agudo, *Appl. Catal. A* 259 (2004) 17.
- [22] R.S. Weber, *J. Catal.* 151 (1995) 470.
- [23] H. Aritani, T. Tanaka, T. Funabiki, S. Yoshida, *J. Phys. Chem. A* 100 (1996) 5440.
- [24] S.M.A.M. Bouwens, R. Prins, V.H.J. de Beer, D.C. Koningsberger, *J. Phys. Chem. A* 94 (1990) 3711.
- [25] S. Kasztelan, E. Payen, H. Toulhoat, J. Grimblot, J.P. Bonnelle, *Polyhedron* 5 (1986) 157.
- [26] C.P. Cheng, G.L. Schrader, *J. Catal.* 60 (1979) 276.

- [27] H. Hu, I.E. Wachs, S.R. Bare, *J. Phys. Chem.* 99 (1995) 10897.
- [28] N.F.D. Verbruggen, G. Mestl, L.M.J. von Hippel, B. Lengeler, H. Knözinger, *Langmuir* 10 (1994) 3063.
- [29] H. Knözinger, H. Jeziorowski, *J. Phys. Chem.* 82/18 (1978) 2002.
- [30] H. Jeziorowski, H. Knözinger, *J. Phys. Chem.* 83/9 (1979) 1166.
- [31] J. Leyrer, M.I. Zaki, H. Knözinger, *J. Phys. Chem.* 90 (1986) 4775.
- [32] B. Canosa-Rodriguo, H. Jeziorowski, H. Knözinger, X. Wang, E. Taglauer, *Bull. Soc. Chim. Belg.* 90 (1981) 1339.
- [33] E. Payen, J. Grimblot, S. Kasztelan, *J. Phys. Chem.* 91 (1987) 6642.
- [34] F.D. Hardcastle, I.E. Wachs, *J. Raman Spectrosc.* 21 (1990) 683.
- [35] N.F.D. Verbruggen, G. Mestl, L.M.J. von Hippel, B. Lengeler, H. Knözinger, *Langmuir* 10 (1994) 3073.
- [36] H. Aritani, T. Tanaka, T. Funabiki, S. Yoshida, M. Kudo, S. Hasegawa, *J. Phys. Chem.* 100 (1996) 5440.
- [37] J. Medema, C. van Stam, V.H.J. de Beer, A.J.A. Konings, D.C. Koningsberger, *J. Catal.* 53 (1978) 386.
- [38] K. Eda, Y. Uno, N. Nagai, N. Sotani, M.S. Whittingham, *J. Solid State Chem.* 178 (2005) 2791.
- [39] R. Cattaneo, F. Rota, R. Prins, *J. Catal.* 199 (2001) 318.
- [40] R. Cattaneo, T. Weber, T. Shido, R. Prins, *J. Catal.* 191 (2000) 225.
- [41] J.F. Cocchetto, C.N. Satterfield, *Ind. Eng. Chem. Process Des. Dev.* 15 (1976) 272.
- [42] T.C. Ho, *Appl. Catal. A* 378 (2010) 52.
- [43] P. Afanasiev, *J. Catal.* 269 (2010) 269.
- [44] G. Perot, *Catal. Today* 10 (1991) 447.
- [45] C.N. Satterfield, J.F. Cocchetto, *Ind. Eng. Chem. Process Des. Dev.* 20 (1981) 53.
- [46] G. Perot, S. Brunet, C. Canaff, H. Toulhoat, *Bull. Soc. Chim. Belg.* 96 (1987) 865.
- [47] M. Jian, R. Prins, *Ind. Eng. Chem. Res.* 37 (1998) 834.
- [48] F. Besenbacher, M. Brorson, B.S. Clausen, S. Helveg, B. Hinnemann, J. Kibsgaard, J.V. Lauritsen, P.G. Moses, J.K. Nørskov, H. Topsøe, *Catal. Today* 130 (2008) 86.
- [49] L.S. Byskov, J.K. Nørskov, B.S. Clausen, H. Topsøe, Sulphur bonding in transition metal sulphides and MoS₂ based structures, in T. Weber, R. Prins, R.A. van Santen (eds.), *Transition Metal Sulphides – Chemistry and Catalysis*, Kluwer Academic Publishers, (1998).
- [50] Henrik Topsøe, *Appl. Catal. A* 322 (2007) 3.
- [51] J. Kibsgaard, A. Tuxen, K.G. Knudsen, M. Brorson, H. Topsøe, E. Laegsgaard, J.V. Lauritsen, F. Besenbacher, *J. Catal.* 272 (2010) 195.
- [52] M. Dage, R.R. Chianelli, *J. Catal.* 149 (1994) 414.

- [53] L. Qu, R. Prins, *J. Catal.* 207 (2002) 286.
- [54] G. Muralidhar, F.E. Massoth, J. Shabtai, *J. Catal.* 85 (1984) 44.
- [55] F.E. Massoth, G. Muralidhar, J. Shabtai, *J. Catal.* 85 (1984) 53.

Chapter 5

Summary

1. Summary

The shortage of light crude oil reserves led to more extensive exploitation of heavy oil due to the continuously increasing demand for transportation fuels, especially diesel fuel. Higher concentration of impurities in heavy hydrocarbons, i.e., sulfur-, nitrogen-, and oxygen-containing compounds, and more severe environmental legislations for the fuel specification, i.e., composition and properties (odour, colour, and stability), have led to a high interest in the hydrotreating chemistry. In industry, hydrotreating reactions, i.e., hydrodesulfurization (HDS), hydrodenitrogenation (HDN), and hydrodeoxygenation (HDO), are carried out simultaneously on a promoted transition metal sulfides (TMS). The effect of individual processes on each other is rather complex. HDN is considered more difficult and more demanding than HDS and it is needed to achieve low sulfur level, to obtain low NO_x emissions, and to protect acid catalytic sites. Basic nitrogen-containing compounds adsorb easily onto acidic catalyst surface, and not all will react therefore leading to inhibition of certain reaction pathways. Non-heterocyclic anilines and aliphatic amines undergo HDN quickly. On the contrary more abundant heterocyclic compounds containing five-member pyrrolic or six-member pyridinic rings are more difficult to convert. Thus, better knowledge of the active sites is expected to lead to a more specific optimization of hydrotreating catalysts.

The HDN, as one of the key hydrotreating reactions, has been studied extensively. Nevertheless, it is still complicate to explicitly establish an atomistic picture of the active sites involved in the various elementary steps, because of its complexity and inhibiting effects of various intermediates. Therefore the main objective of the thesis is to address the catalytic chemistry of supported and unsupported (Ni)MoS₂ catalysts in the quinoline HDN network by combining activity measurements with characterization of sulfide catalysts as well as oxide precursors. Reactions are carried out in the presence of sulfur-containing compound, dibenzothiophene (DBT), to study the effect of competitive adsorption.

The overall network of nitrogen removal from quinoline has been explored because quinoline bicyclic nature allows studying all elementary steps involved in the HDN. The reaction starts with hydrogenation followed by ring opening via C(sp³)-N bond cleavage, and finally nitrogen is removed via C(sp²)-N and C(sp³)-N bond cleavage. *Chapter 2* is focused on the o-propylaniline (OPA) HDN to better understand the critical reaction steps in the overall quinoline HDN sequence. Moreover, the competitive adsorption of various basic nitrogen-containing intermediates is so avoided ensuring the absence of additional inhibition effects. MoS₂/γ-Al₂O₃ and NiMoS/γ-Al₂O₃ catalyst is explored to address the impact of Ni on the catalytic properties of MoS₂.

Under all reaction conditions and on both catalysts studied, the OPA HDN follows two reaction pathways that occur on two separate sites. The first route involves the direct denitrogenation (DDN) via aromatic C(sp²)-N bond cleavage to form propylbenzene (PB). The second route involves the hydrogenation (HYD) of the OPA phenyl ring to form propylcyclohexylamine (PCHA) that is further converted to propylcyclohexene (PCHE) via C(sp³)-N bond cleavage. PCHE is further hydrogenated to propylcyclohexane (PCH). The rate of the phenyl ring hydrogenation is limiting, while that of nitrogen removal via Hofmann-type elimination of NH₃ is comparably large.

The DDN route proceeds on coordinatively unsaturated sites (CUS) via a reverse Mars-van Krevelen mechanism; the N atom, initially in the molecule, remains in the catalyst surface after the reaction. Even though a higher concentration of CUS is found on the promoted NiMoS/γ-Al₂O₃ compared to MoS₂/γ-Al₂O₃ catalyst, the rate of DDN was drastically lower. Thus, it is concluded that only Mo associated cations at the S-edge of the MoS₂ cluster are active for the DDN route were OPA is adsorbed via σ-bonding. The presence of Ni cations dilutes these sites and lowers the reaction rate. It is interesting to note that the reduction in activity fits well to the statistical incorporation of Ni into MoS₂. If DBT is converted in parallel to OPA, its competitive adsorption reduces the DDN rate. The identical relative reduction in the DDN rate by DBT for MoS₂/γ-Al₂O₃ and NiMoS/γ-Al₂O₃ is a strong indirect proof that the nature of these sites is identical in both catalysts. The dominating reaction pathway in DBT HDS was the direct desulfurization (DDS) leading to biphenyl as dominating product. Much higher HDS rate on NiMoS/γ-Al₂O₃ than on MoS₂/γ-Al₂O₃ catalyst suggests that not only the concentration of CUS has increased but also the intrinsic rate constant of that reaction.

The absence of a negative effect of the parallel DBT conversion on the OPA hydrogenation route on MoS₂/γ-Al₂O₃ and dramatic enhancement of the rate on NiMoS/γ-Al₂O₃ led to a conclusion that CUS are not active in HYD. If CUS would be involved in the adsorption site or the active site for the reaction, the presence of DBT would decrease the reaction rate, because of the competitive adsorption. Thus the brim sites, electron-rich zones associated with metal-like states are proposed, where the interaction with the aromatic ring and the propyl group must outweigh the direct bonding of the amine nitrogen with CUS. Using the argumentation from scanning tunneling microscopy (STM) model studies, we suggest that the higher intrinsic rate is related to the higher electron density at the brim sites in the presence of Ni.

The ring opening steps of bicyclic molecules, e.g., 14THQ and DHQ, has received less attention than the DDN and HYD steps. However the efficiency of the overall quinoline HDN depends on the catalyst ability to open the ring via C(sp³)-N bond cleavage. *Chapter 3*

explore the HDN of quinoline and decahydroquinoline (DHQ) to evaluate the initial hydrogenation/dehydrogenation steps followed by the C(sp³)-N bond cleavage in 1,2,3,4-tetrahydroquinoline (14THQ) and DHQ leading to OPA and PCHA, respectively. Two main routes examined, i.e., DHQ → PCHA (via C(sp³)-N ring opening) → PCHE (via C(sp³)-N bond cleavage) → PCH (via hydrogenation), and quinoline → 14THQ (via hydrogenation) → OPA (via C(sp³)-N ring opening) → PCHA (via hydrogenation) and PB (via C(sp²)-N bond cleavage), showed two different limiting steps. In the first route the rate limiting step is the 14THQ ring opening, while in the later it is the OPA HYD, as shown in *Chapter 2*.

The intrinsic rate of the ring opening reaction is lower for 14THQ than for DHQ, because the interaction of nitrogen free electron pair with the electrons of the benzoic ring stabilizes 14THQ. The nitrogen free electron pair in DHQ facilitates the formation of the quaternized nitrogen atom, which presents the leaving group in the Hofmann-type mechanism, proposed for the C(sp³)-N bond cleavage. The dual site, needed for the Hofmann-type elimination mechanism, consists of acidic -SH groups located close to the brim sites of MoS₂ or NiMoS slabs (formed by H₂ dissociation on S²⁻ dimers), and basic S²⁻ ions. DHQ and 14THQ adsorption involves the interaction of the -NH- fragment with -SH groups. DBT stabilizes the sulfide surface converting the CUS (inactive for the ring opening) into the basic S²⁻ ions. Nickel as a promoter facilitates H₂ dissociation and its mobility on the sulfide surface, providing more active -SH groups. On the other hand nickel increases the basicity of the S²⁻ ions, increasing the sulfur electron density and hence facilitates the β-H atom removal.

After establishing the overall picture of the quinoline HDN network and active sites responsible for individual steps, *Chapter 4* correlates the catalyst morphology and HDN activity and selectivity. More insight has been given on the physicochemical properties and molecular structure of a series of supported Mo/γ-Al₂O₃, NiMo/γ-Al₂O₃, and novel unsupported NiMo catalysts. The supported Mo/γ-Al₂O₃ and NiMo/γ-Al₂O₃ oxide catalyst precursors exhibited well dispersed amorphous polymolybdate structure that led to a formation of high dispersed sulfide phase with the average MoS₂ stacking degree of two and slabs length of 10 nm. On the contrary, NiMo/unsupported precursor exhibited a mixture of nickel molybdate and an ammonium nickel molybdate crystalline phase that formed multi-stacked sulfide slabs. The quinoline HDN activity increased in the following order: MoS₂/γ-Al₂O₃ < NiMoS/unsupported < NiMoS/γ-Al₂O₃, therefore, high catalyst dispersion, i.e., lower stacking degree was the key factor for high HDN activity.

Curriculum Vitae

Ana Hrabar was born on August, 10th of 1981 in Belgrade, Serbia. After finishing high school "X Beogradska gimnazija - Mihailo Pupin" in Belgrade in 2000, she started a chemical engineering course of studies at "Faculty of Technology and Metallurgy" at University of Belgrade, Department of Organic Chemical Technology and Polymer Materials. She graduated in December 2005, after finishing Diploma Thesis entitled "Application of optical fibers for damage detection in polymer composite structures", which was performed at the Department of Structural and Special Materials under supervision of Prof. R. Aleksić. She obtained a reward for the best 100 students at University of Belgrade. In October 2006 she joined the Chair of Technische Chemie II of Prof. J.A. Lercher at TU München to start research on the selective oxidation of propane to acrylic acid. In January 2007 she continued to work as a PhD student in the same group. Her work was focused on the hydrodenitrogenation reactions carried out on the unsupported and supported transition metal sulfide catalysts.

List of publications

- [1] A. Wawrzetz, B. Peng, A. Hrabar, A. Jentys, A.A. Lemonidou, J.A. Lercher
Towards understanding the bifunctional hydrodeoxygenation and aqueous phase reforming of glycerol
Journal of Catalysis 269 (2010) 411
- [2] O.Y. Gutiérrez, C. Kaufmann, A. Hrabar, Y. Zhu, J.A. Lercher
Synthesis of methyl mercaptans from carbonyl sulfide over sulfide K_2MoO_4/SiO_2
Journal of Catalysis 280 (2011) 264
- [3] A. Hrabar, J. Hein, O.Y. Gutiérrez, J.A. Lercher
Selective poisoning of the direct denitrogenation route in o-propylaniline HDN by DBT on Mo and NiMo/ γ - Al_2O_3 sulfide catalysts
Journal of Catalysis, In Press, Available online 17 June 2011
- [4] A. Hrabar, J. Hein, Y. Yu, O.Y. Gutiérrez, J.A. Lercher
C(sp³)-N bond cleavage in the ring opening of 1,2,3,4-tetrahydroquinoline and decahydroquinoline on Mo and NiMo/ γ - Al_2O_3 sulfide catalysts
Ready for submission
- [5] A. Hrabar, J. Hein, O.Y. Gutiérrez, J.A. Lercher
Characterization and performance of γ - Al_2O_3 supported Mo and NiMo and novel unsupported NiMo catalysts in the HDN of quinoline
Ready for submission